

Silicate Liquids at Conditions of the Earth's Interior

-From Atomic Scale-

March, 2015

NORITAKE Fumiya

Graduate School of  
Environmental and Life Science  
(Doctor's Course)

OKAYAMA UNIVERSITY

# Contents

## **1. Introduction**

## **2. Experimental study of silicate liquids at pressure: a review**

2.1 Experimental studies of physical properties of silicate liquids and glasses at pressure

2.2 Experimental studies about structure of silicate liquids and glasses at pressure

2.3 Relationship between structure and properties of silicate liquids at pressure

## **3. Basic concept of Molecular Dynamics Method**

3.1 Verlet algorithm

3.2 Symplectic molecular dynamics method

-Symplectic Condition

-Derivation of Verlet Algorithm from symplectic condition

-Conservative quantity in symplectic condition

3.3 Ewald summation

3.4 Calculation of the physical properties from MD

-Static properties

-dynamic properties

## **4. Nature of Si-O-Si bonding by molecular orbital calculation**

4.1 Computational Method

4.2 Result and Discussions

4.3 Conclusions

## **5. Na<sub>2</sub>O-nSiO<sub>2</sub> liquid at pressure**

5.1 Computational method

5.2 Result and Discussions

-Densification Mechanisms

-Transport Coefficients

5.3 Conclusions

## **6. Interface of Silicate liquid**

6.1 Computational Method

6.2 Result and Discussions

-4 nm liquid film: The structuralized liquid film

-16 nm liquid film

-Effect of film thickness

-General discussion

-Implications

6.3 Conclusions

## **7. References**

## 1. Introduction

Knowledge of the properties of silicate liquid is essentially important in Earth science, metallurgy and glass industry. The transport properties and densities of silicate liquids at pressure are used for the study of magmatic process and early Earth process. The silicate liquids appears as slag in metallurgy. The silicate liquids appears as raw material of glass forming process. The physical properties such as viscosities, densities, electrical conductivity and more, are reported by various researchers in various fields. The atomic structure, especially near neighbor structure and network structure of silicate liquids have been investigated using various spectroscopic method such as X-ray diffraction, neutron diffraction, nuclear magnetic resonance and Raman scattering, etc. The silicate liquids composed of corner shared  $\text{SiO}_4$  tetrahedra and network modifiers such as alkali or alkali earth elements under atmospheric pressure (Waseda and Toguri, 1977). It means that the silicate liquids has no three-dimensional periodic structure but short-range-ordered structure.

Basicity,  $B$  is used to characterize the structure and properties of silicate liquids as simple binary system. The basicity is written as follows;

$$B = \frac{\text{mol}\%R_2O}{\text{mol}\%SiO_2}$$

The basicity represents growth of network of corner shared  $\text{SiO}_4$  tetrahedra that

controls various physical properties. Proportion of corner shared  $\text{SiO}_4$  tetrahedra decrease with increasing basicity of liquids (Maekawa et al. 1990), then viscosity of liquid decrease (Bockris et al. 1955).

The properties of silicate liquids at pressure must be investigated to understand volcanic process and early Earth process. The physical properties of silicate liquids show peculiar behaviors under pressure. The viscosities of low basicity liquids decrease with increasing pressure (Kushiro 1976; Scarfe et al. 1979; Suzuki et al. 2002). Moreover, the self-diffusivity of O and Si atoms in liquids increases with increasing pressure (Rubie et al. 1993; Poe et al. 1997). These shows the softening of silicate liquids at pressure.

The atomic structure of silicate liquids have been investigated by various spectroscopic method. Si-O distance remains constant up to several giga-pascals whereas Si-Si distance shortens, according to X-ray diffraction studies (Meade et al. 1992; Funamori et al. 2004). This indicates that the compression of silicate liquids is caused by shrinking of  $-\text{Si-O}-$  network. NMR studies about glass quenched at pressure reported that pressure induced polymerization occur and higher coordinated Si species appear over 10 GPa (Xue et al. 1989, 1991). This type of structural change was also reported by Raman scattering studies (Mysen 1990; McMillan et al. 1984).

Several mechanisms have been proposed to explain the softening of the silicate liquids under pressure. One hypothesis is that weakening of Si-O bonds caused by bending of Si-O-Si angle from ideal angle during compression (Kushiro 1976, 1980). Other hypothesis is that oxygen atoms diffuse via weak-bonded higher coordinated Si species which appear gradually at pressure (Xue et al. 1991). However, those hypothesis are not verified by spectroscopic studies because they are only able to investigate inter-atomic distance of near neighbors or quantity of species.

I investigated the structure and properties of silicate liquids by force-field molecular dynamics (MD) simulations. The trajectories of each atom are implicitly able to obtain in MD simulations. Moreover, it is also possible to identify the individual atoms or groups of atoms which play a deciding role in diffusion processes by use of MD simulations.

I here show the relationship between structural change and physical properties of  $\text{Na}_2\text{O-SiO}_2$  liquid as functions of pressure and basicity. I also show the characteristic structure on the interface of silicate liquids which controls transport properties of partially molten rock.

## 2. Experimental studies of silicate liquids at pressure: a review

### 2.1 Experimental studies of physical properties of silicate liquids and glasses at pressure

The pressure dependence of shear viscosities of silicate liquids have been investigated since 1970's. Viscosities at pressure are measured using falling sphere method in high pressure vessel (Kushiro, 1976). It is a well-known fact that viscosities of acidic silicate liquids have a negative correlation with pressure (Fig. 2.1). The viscosity of diopside liquid ( $B = 1.0$ ) increase with increasing pressure, however, viscosities of acidic silicate liquids ( $B > 2.0$ ) decrease with increasing pressure. The viscosities of fully networked liquids (e.g. Albite liquid) have strong negative correlation with pressure (Fig. 2.2). The viscosity of  $\text{Na}_2\text{O} \cdot 2\text{SiO}_2$  liquid ( $B = 2.0$ ) increase with increasing pressure up to 1.5 GPa, then start to decrease with increasing pressure. These experimental results suggest pressure induced increase of oxygen and silicon diffusivity in acidic silicate liquids considering the Eyring's equation (eq. 2.1),

$$\eta = \frac{1}{\beta \lambda D} \quad (2.1)$$

where  $\eta$  is shear viscosity,  $\beta$  is reciprocal temperature,  $\lambda$  is the jump distance and  $D$  is self-diffusion coefficients. This equation has been used with remarkable success in a variety of silicate liquids to relate diffusivity of network forming atoms and shear

viscosity (e.g., Oishi et al., 1975; Dunn, 1982; Shimizu and Kushiro, 1984; Rubie et al., 1993; Lacks et al., 2007). In fact, the self-diffusion coefficients of network forming elements in acidic silicate liquids increase with increasing pressure (Fig. 2.3). In contrast, the increase of mobility of network forming elements induced by pressure does not affect to electrical conductivity. The relationship between electrical conductivity and ion mobility can be expressed by Nernst-Einstein relation as follows,

$$\kappa = \beta e^2 \sum_i n_i q_i^2 D_i$$

where  $\kappa$  is the electrical conductivity,  $\beta$  is the reciprocal temperature,  $e$  is the elementary charge,  $n_i$  is the number density of  $i$ -th ion,  $q_i$  is the charge of  $i$ -th ion and  $D_i$  is the self-diffusion coefficients of  $i$ -th ion. The electrical conductivity of  $\text{Na}_2\text{O} \cdot 3\text{SiO}_2$  liquid decrease with increasing pressure (Fig. 2.4). This indicates the diffusivity of Na ion is much larger than that of network forming elements.

Density is one of the important physical properties. However, there are no precise data about pressure dependence of density of silicate liquids at pressure because of the difficulty in density measurement at high-pressure vessel. Anomalous compression behavior of silicate liquids is supposed from compression data of silicate glass. Albite glass have density jump at 1.5 to 2.0 GPa (Fig. 2.5). Silica glass quenched at 10 GPa have different compression curve comparing with that quenched at ambient pressure

(Fig. 2.6). There is no anomalous compression behavior in peridotite liquid (Fig. 2.7)

## 2.2 Experimental studies about structure of silicate liquids and glasses at pressure

X-ray diffraction method is widely used for study of average structure of the structurally disordered matter. The ideal intensity of scattered X-ray at detector is written as follows,

$$I(\mathbf{Q}) = A \left| \sum_p f_p(\mathbf{Q}) \exp(i\mathbf{Q} \cdot \mathbf{R}_p) \right|^2 \quad (2.3)$$

where  $I$  is intensity,  $\mathbf{Q}$  is momentum transfer vector,  $A$  is the coefficient,  $f_p(\mathbf{Q})$  is the square root of scattering cross-section at point  $p$  in sample and  $\mathbf{R}_p$  is the vector from origin in sample to point  $p$  in sample. Normalizing eq.2.3 by scattering cross-section of one electron and approximating electrons are just around the nuclei, the intensity can be written as follows,

$$I_{eu}(\mathbf{Q}) = \left| \sum_i \exp(i\mathbf{Q} \cdot \mathbf{R}_i) \right|^2 |f_a(\mathbf{Q})|^2 \quad (2.4)$$

where  $I_{eu}$  is normalized intensity,  $\mathbf{R}_i$  is coordinates of  $i$ -th atom in the sample and  $f_a$  is atomic scattering factor. The former factor of the right side in eq. 2.4 is defined as structural factor,  $S$ ,

$$\left| \sum_i \exp(i\mathbf{Q} \cdot \mathbf{R}_i) \right|^2 \equiv NS(\mathbf{Q}) \quad (2.5)$$

where  $N$  is the number of atoms in the sample. The radial distribution function  $g(r)$  (see chapter 3.4) can be obtained using Fourier transformation as follows,

$$g(r) = 1 + \frac{1}{8\pi^3 n_0} \int_0^\infty dQ (S(Q) - 1) \frac{\sin Qr}{Qr} 4\pi Q^2 \quad (2.6)$$

where  $n_0$  is the number density of the sample. This is the only ideal case considering no inelasticity and mono-element system. However, the radial distribution function of real material can be obtained from extending the eq. 2.3 to eq. 2.6.

The structures of silicate liquids at pressure is investigated by various spectroscopic method. For instance, X-ray diffraction studies give the of radial distribution function and changes of inter-atomic distance. In compression of  $\text{SiO}_2$  glass, Si-O bond length increase with increasing pressure above 10 GPa (Fig. 2.8). The Si-O length is between the variation of that in  $\text{SiO}_2$  polymorphs consists of  $\text{SiO}_4$  tetrahedra (e.g.  $\alpha$ -quartz, coesite) up to 10 GPa. Above 10 GPa, the Si-O length leach to the compression curve of Si-O length of  $\text{SiO}_6$  octahedra in stishovite. This indicates the increase of coordination number of Si above 10 GPa. The T-O (T = Si, Al) length remains almost constant at lower pressure in the in-situ X-ray diffraction study about jadeite liquids at pressure (Fig. 2.9). However the T-T length decrease and T-O-T angle decrease with increasing pressure. This indicates the collapse of  $\text{TO}_4$  corner shared

network.

The structural changes reported by X-ray studies are also reported by other spectroscopic method. The coordination states is quantitatively obtained by using nuclear magnetic resonance (NMR) spectroscopy. The pressure induced change of coordination number of network former elements is reported by NMR spectroscopy study about acidic sodium silicate and sodium aluminosilicate glass quenched at high pressure (Fig. 2.10). This experimental data shows that the high-coordinated network forming elements start to exist above 4 GPa and increase with increasing pressure. The pressure induced decrease of T-O-T angle is also reported by NMR spectroscopic study of SiO<sub>2</sub> glass (Fig. 2.11).

### **2.3 Relationship between structure and properties of silicate liquids at pressure**

The densification mechanism of silicate liquids is explained by collapse of -T-O- network and increase of higher coordinated network forming elements (Stolper and Ahrens 1987). The TO<sub>4</sub> tetrahedra is hard to be compressed, however the average T-O-T angle decrease and silicate liquids densify (Sakamaki et al. 2012). The decrease of T-O-T angle and collapse of -T-O- network finally makes higher coordinated network forming elements (Fig. 2.12). Al atom easily becomes higher coordinated state than Si

atom (Fig. 2.10). In the compression of anorthite system, 4-fold Al in anorthite becomes 6-fold Al in kyanite and grossular (Hariya and Kennedy, 1968). Kaolinite contains 6-fold Al even though that is not high-pressure mineral (Bish, 1993). The fact that Al easily become higher coordinated state by pressure can explain the density jump in compression of the albite glass because the increase of coordination number increases the density (Fig. 2.5). However the increase of coordination number cannot explain the existence of two different compression curve of  $\text{SiO}_2$  glass (Fig. 2.6) because the increase of higher coordinated Si occur above 10 GPa.  $\text{SiO}_2$  has 3 high-temperature polymorphs and 2 (or more) high-pressure polymorphs. Stishovite that exist above  $\sim 7$  GPa has rutile-type structure. However the coesite that exist between about 2 to 7 GPa have network structure of corner shared  $\text{SiO}_4$  tetrahedra. The difference between coesite structure and  $\alpha$ -quartz is the size of membered ring.  $\alpha$ -quartz crystal consist of 6-membered ring unit (Levien et al. 1980), however, coesite crystal consist of 4-membered ring unit (Gibbs et al. 1977). The few-membered ring has smaller T-O-T angle than multi-membered ring. That means silicates consisting of few-membered ring is dense than that consisting of multi-membered ring. The difference between glass quenched at 10 GPa and that quenched at ambient pressure might be explained by the difference of membered ring units in -Si-O- network.

The mechanism of pressure induced softening of acidic silicate liquids is considered as the change of coordination number of network former elements (Xue et al. 1989, Poe et al. 1997). Their hypothesis is that the higher coordination network forming atoms act as the intermediate state of diffusion. In fact, the pressure induced change of abundance of 5-fold aluminum in aluminosilicate liquid related to oxygen diffusivity (Poe et al. 1997). Higher-coordinated Si do not seem to exist in  $\text{Na}_2\text{Si}_4\text{O}_9$  glass below 4 GPa (Poe et al. 1997). Adding to that, the increase of abundance of higher coordinated Si in acidic silicate glass by pressure is faster than those in basic glass (Xue et al. 1991). However the decrease of viscosity of  $\text{Na}_2\text{O} \cdot n\text{SiO}_2$  liquid ( $n = 2, 3$ ) starts below 4 GPa. Consequently, not only the higher coordinated network former elements but also other structural change enhance the diffusion and decrease the viscosity of liquid. One possible structural change is decrease of T-O-T angle. The decrease of Si-O-Si angle weakens the Si-O bonding because of the existence of lone-pair electron around oxygen (Newton and Gibbs, 1980; Kubicki and Sykes, 1993). If aluminum atoms are in tetrahedra, the decrease of T-O-T angle increases the total energy by the charge compensation (Geisinger et al., 1985). I postulate that the molecule in Eyring's viscosity model of liquid is  $\text{SiO}_4$  tetrahedra. The Eyring's viscosity equation is written as follows,

$$\eta = \frac{hN_A}{V_m} e^{\Delta E/\beta} \quad (2.6)$$

where  $h$  is Plank's constant,  $N_A$  is Avogadro's number,  $V_m$  is the volume of molecule and  $\Delta E$  is the activation energy. The T-O bond strength cannot be used directly for the activation energy because the activation energy expresses not only the exchanging of one bond but also the sliding of bulk liquid. However, the change of bonding energy affect the activation energy because the activation energy is the energy barrier between two states and the height of energy barrier is affected by the sum of interatomic energy that expresses the total energy of state in thermal processes. T-O-T angle in SiO<sub>2</sub> glass and jadeite melt decrease with increasing pressure (Fig. 2. 9, 2.11). Consequently, the pressure-induce softening of silicate liquids can be explained by T-O bond weakening by decrease of T-O-T angle.

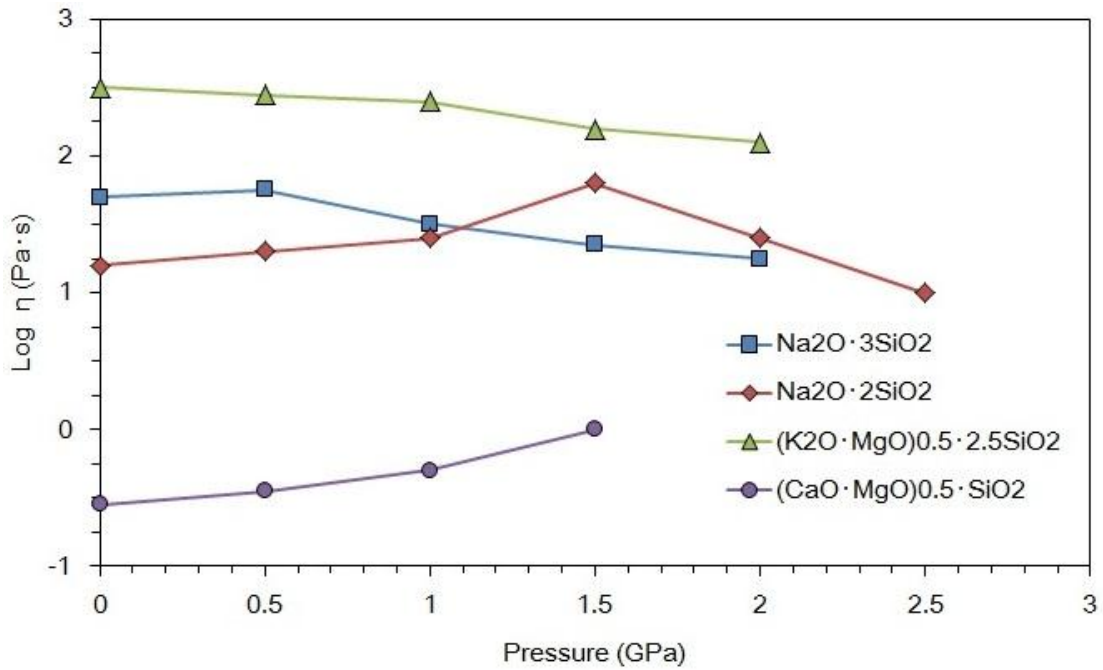


Fig. 2.1. The plots of logarithm of viscosity of various silicate liquids at 1448 K ( $\text{Na}_2\text{O} \cdot 3\text{SiO}_2$ ), 1473 K ( $\text{Na}_2\text{O} \cdot 2\text{SiO}_2$ ), 1913 K (Diopside composition) and 1573 K ( $\text{K}_2\text{O} \cdot \text{MgO} \cdot 5\text{SiO}_2$ ) versus pressure. The data are taken from Kushiro (1976, 1977) and Scarfe et al. (1979).

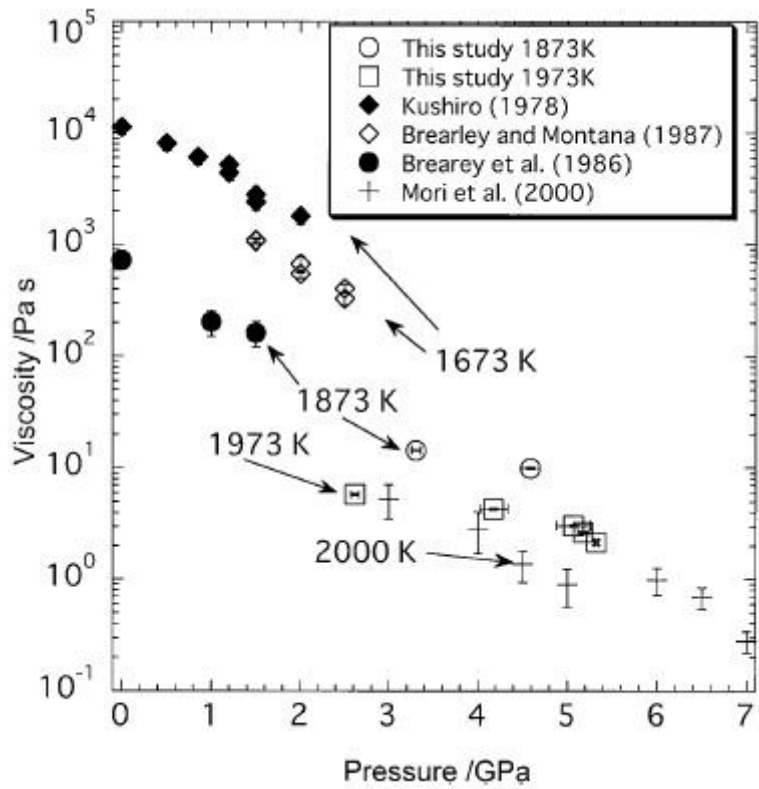


Fig. 2.2. The plots of viscosity of albite liquid versus pressure. This figure is taken from Suzuki et al. (2002).

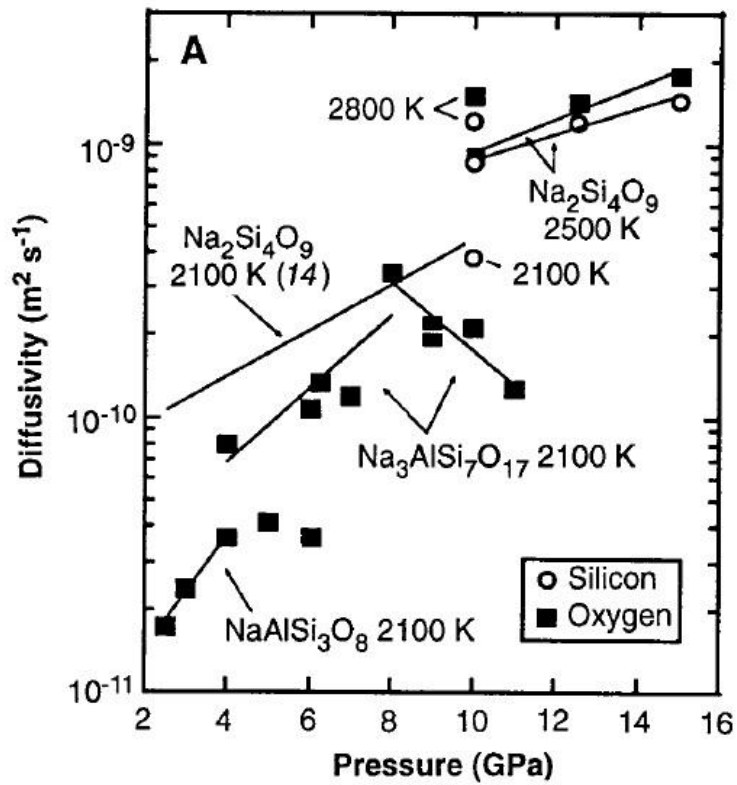


Fig. 2.3. The plots of diffusivity of network former elements in silicate liquids at pressure. This figure is taken from Poe et al. (1997).

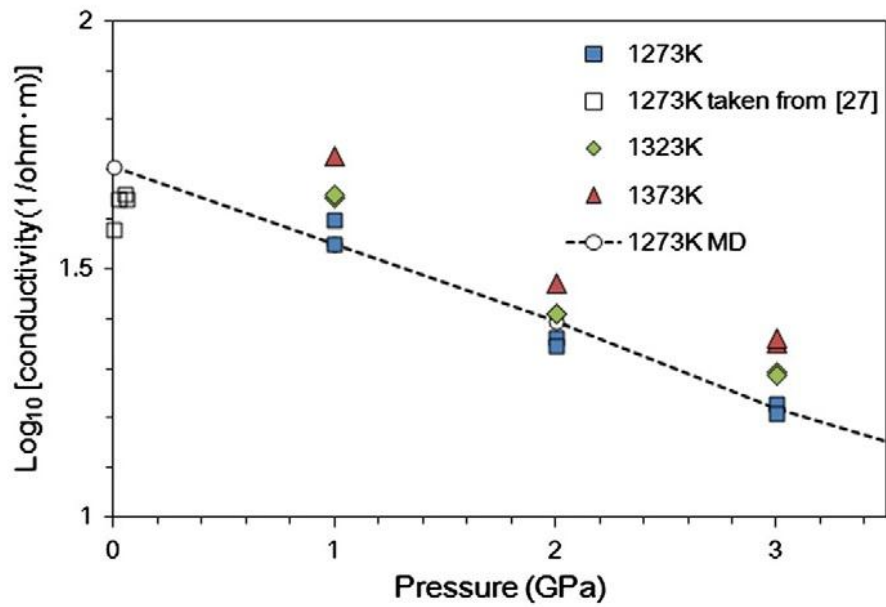


Fig. 2.4. The plots of logarithm of electrical conductivity of  $\text{Na}_2\text{O} \cdot 3\text{SiO}_2$  liquids versus pressure. This figure is taken from Noritake et al. (2012)

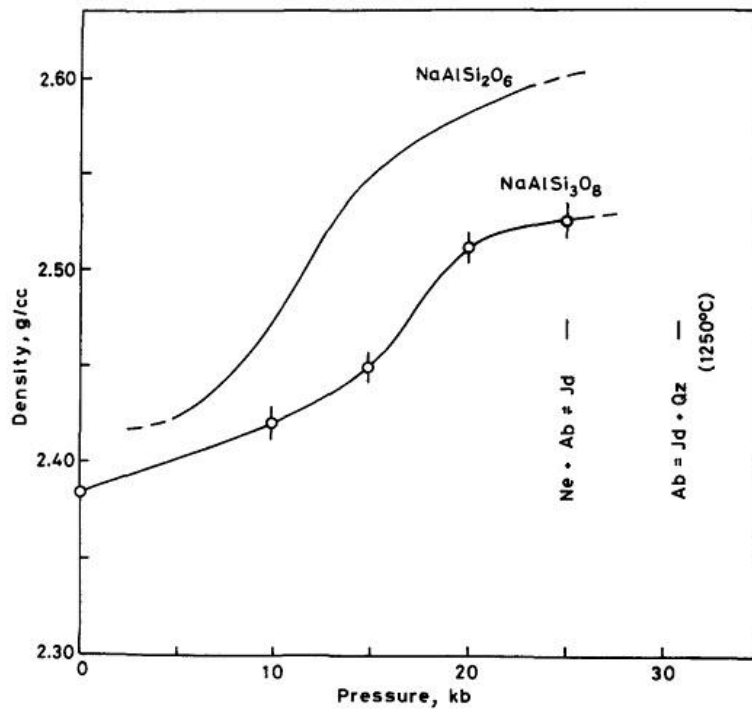


Fig. 2.5. The plots of density of albite glass versus pressure. This figure is taken from Kushiro (1978).

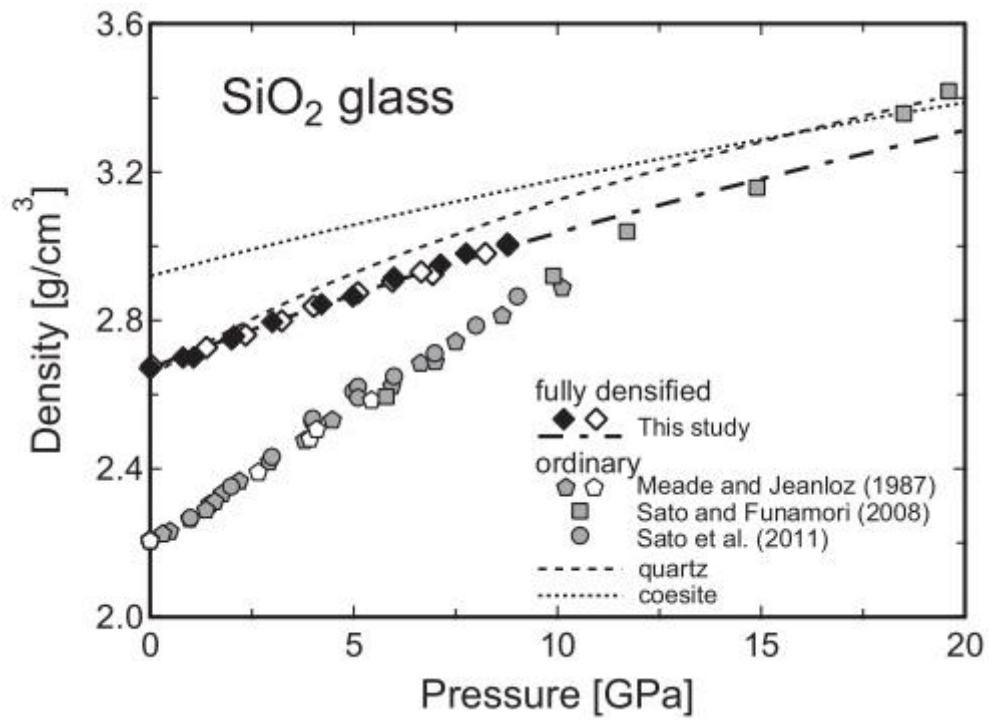


Fig. 2.6. The plots of densities of SiO<sub>2</sub> glass and that quenched at 10 GPa versus pressure. This figure is taken from Wakabayashi et al. (2013).

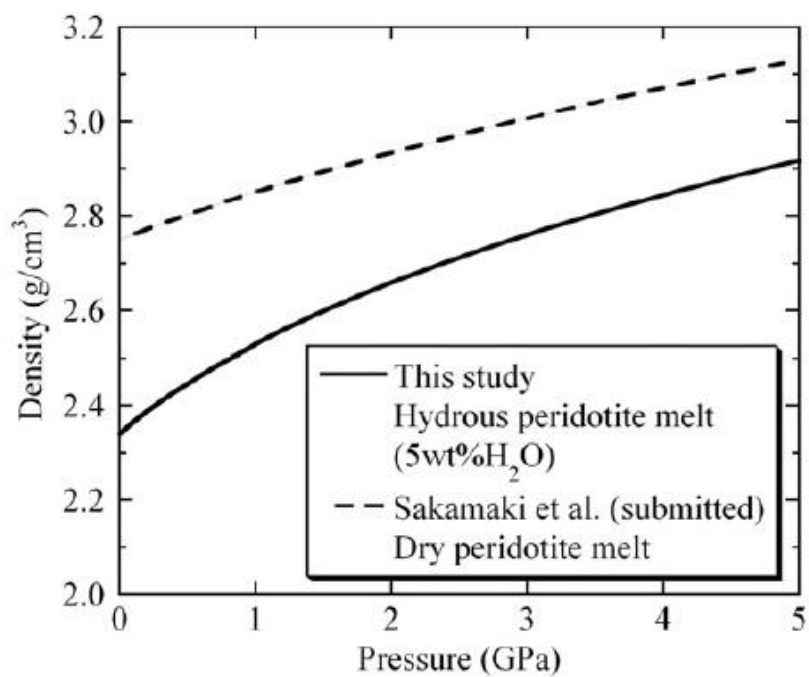


Fig. 2.7. The plots of density of peridotite liquid at pressure. This figure is taken from Sakamaki et al. (2009)

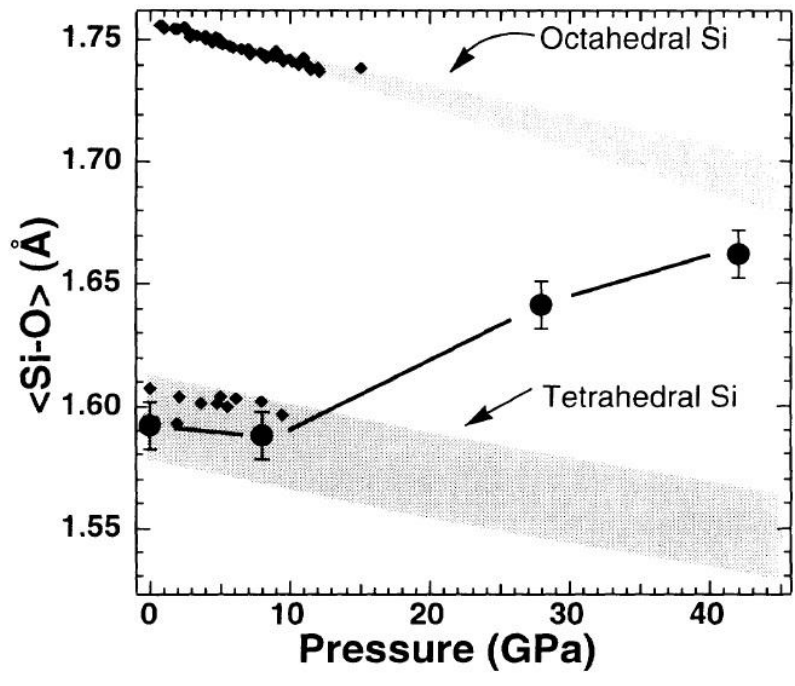


Fig. 2.8. The plots of Si-O bond distance in SiO<sub>2</sub> glass along compression. This figure is taken from Meade et al. (1992)

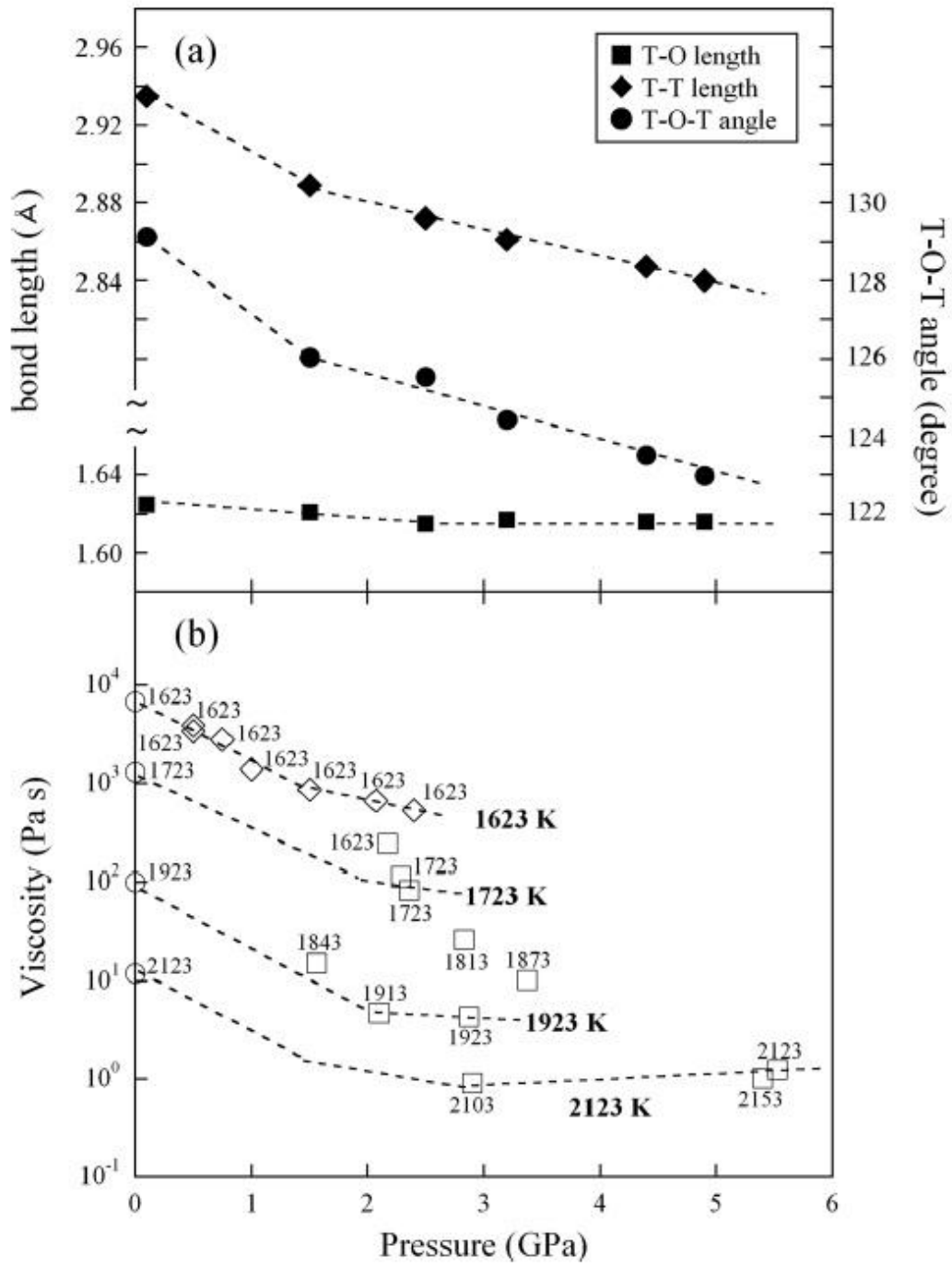


Fig. 2.9

The plots of bond length, T-O-T angle and Viscosity of jadeite liquid at pressure. This

figure is taken from Sakamaki et al. (2012)

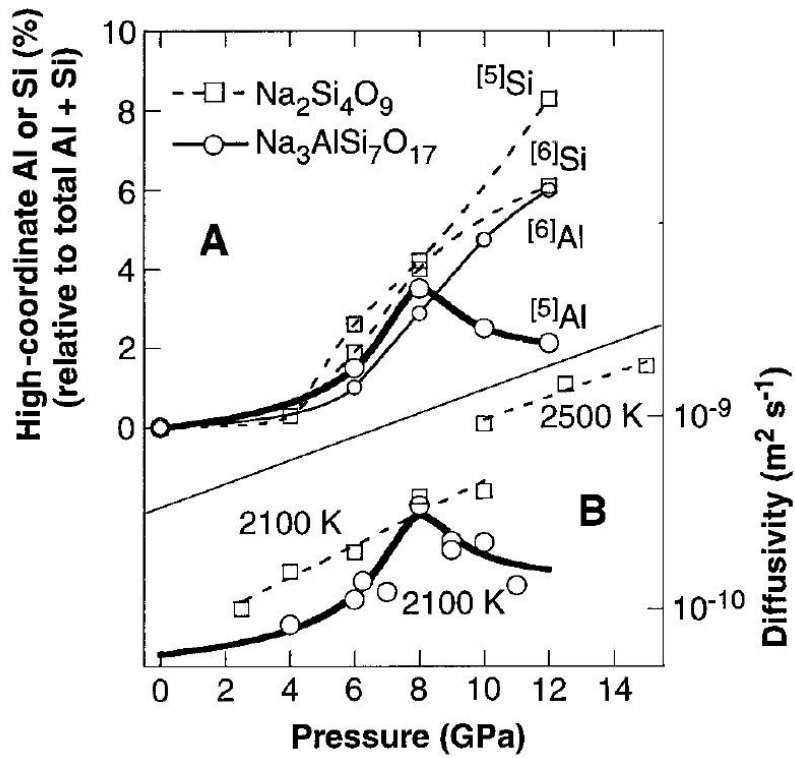


Fig. 2.10. The plots of abundance of high-coordinated Al and Si, and diffusivity of oxygen as functions of pressure. This figure is taken from Poe et al. (1997).

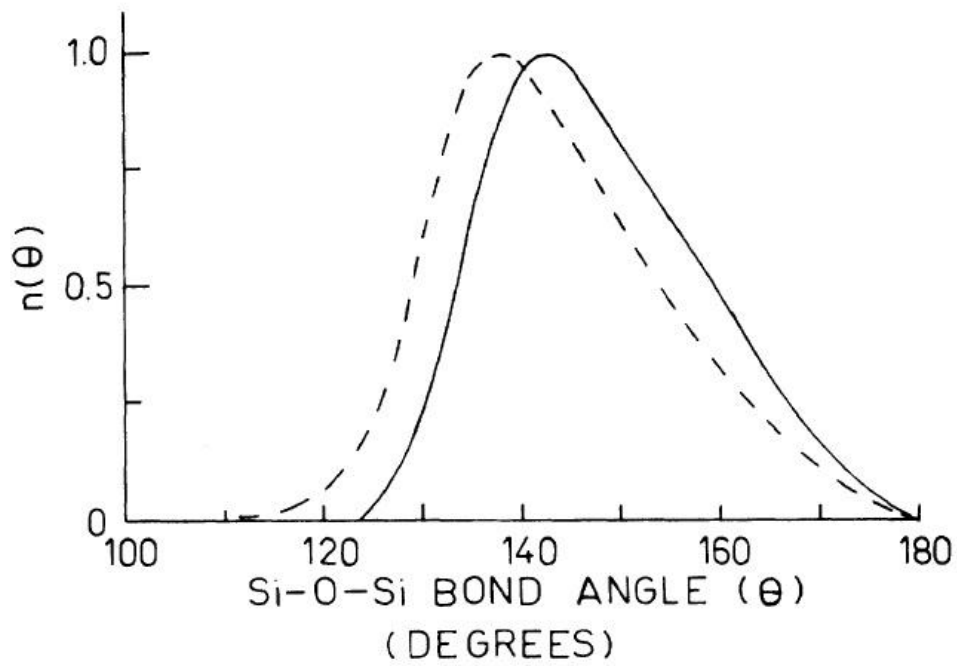


Fig. 2.11.

The plots of distribution of Si-O-Si bond angle in  $\text{SiO}_2$  glass at atmospheric pressure (solid line) and 5 GPa (dashed line). This figure is taken from Devine et al. (1987)

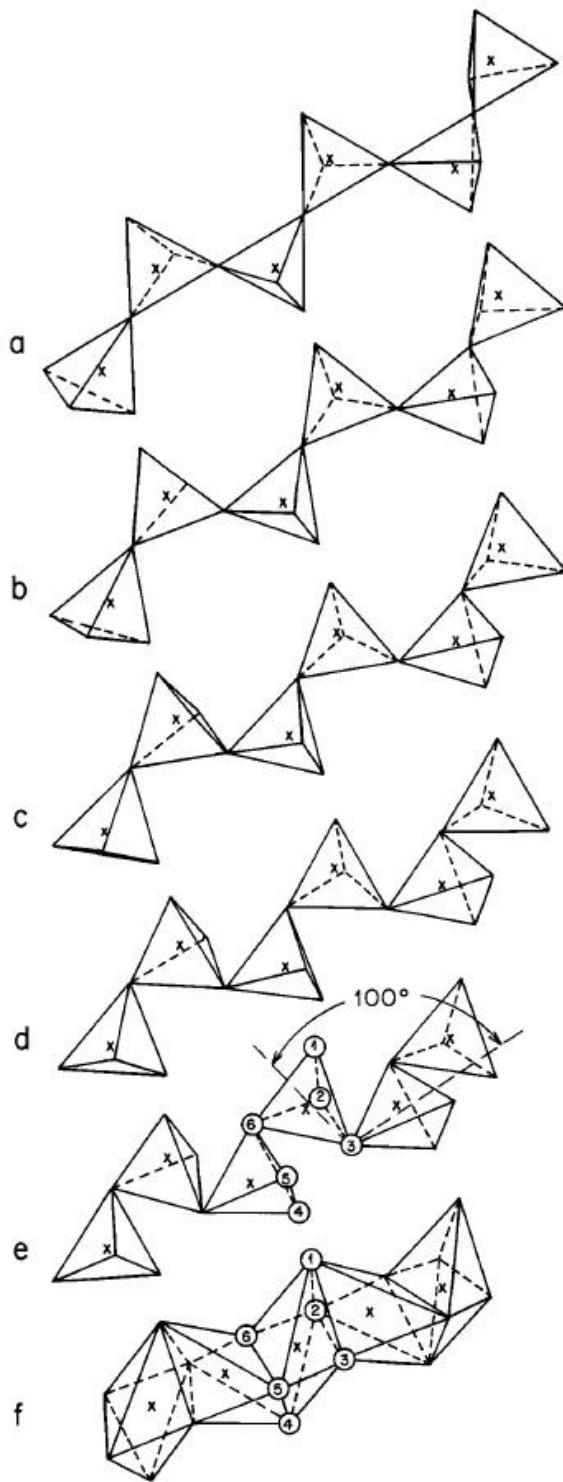


Fig. 2.12. The schematic figure of collapsing of -Si-O- network and changes in coordination. This figure is taken from Stolper and Ahrens (1987)

### 3. Basic concept of molecular dynamics simulations

In Molecular Dynamics (MD) simulations, all the atoms are firstly given initial positions and velocities, then atoms move according to the classical mechanics with given force fields under desired ensemble. We can observe pico-second dynamical phenomena with atomistic or molecular scale and instantaneous structure because we can obtain the trajectories of each atoms by use of MD simulations.

#### 3.1 Verlet algorithm

The Verlet algorithm that has been most frequently used in molecular dynamics simulations is the method to solve differentiation equation of motions of atoms.

Newtonian equation is given by

$$\mathbf{F}_i(t) = m_i \frac{d^2 \mathbf{r}_i(t)}{dt^2} \quad (3.1)$$

where  $\mathbf{F}_i$  is force that apply to i-th atom and  $\mathbf{r}_i$  is coordination of i-th atom. After  $\Delta t$

( $\Delta t \ll 1$ ), the coordination of i-th atom  $\mathbf{r}_i(t + \Delta t)$  can be written as follows by Taylor expansion.

$$\mathbf{r}_i(t + \Delta t) = \mathbf{r}_i(t) + \frac{d}{dt} \mathbf{r}_i(t) \Delta t + \frac{1}{2!} \frac{d^2}{dt^2} \mathbf{r}_i(t) \Delta t^2 + \frac{1}{3!} \frac{d^3}{dt^3} \mathbf{r}_i(t) \Delta t^3 + \dots \quad (3.2)$$

Similarly, the coordination of i-th atom  $\mathbf{r}_i(t - \Delta t)$  can be written as follows.

$$\mathbf{r}_i(t - \Delta t) = \mathbf{r}_i(t) - \frac{d}{dt}\mathbf{r}_i(t)\Delta t + \frac{1}{2!}\frac{d^2}{dt^2}\mathbf{r}_i(t)\Delta t^2 - \frac{1}{3!}\frac{d^3}{dt^3}\mathbf{r}_i(t)\Delta t^3 + \dots \quad (3.3)$$

Adding both side of (3.2) and (3.3), we can obtain (3.4),

$$\mathbf{r}_i(t + \Delta t) = 2\mathbf{r}_i(t) - \mathbf{r}_i(t - \Delta t) + \frac{d^2}{dt^2}\mathbf{r}_i(t)\Delta t^2 + O(\Delta t^4) \quad (3.4)$$

where  $O$  is Landau symbol. Therefore, we can obtain the Verlet algorithm by

substituting (3.1) to (3.4).

$$\mathbf{r}_i(t + \Delta t) = 2\mathbf{r}_i(t) - \mathbf{r}_i(t - \Delta t) + \frac{\mathbf{F}_i(t)}{m_i}\Delta t^2 \quad (3.5)$$

This means that it is possible to calculate the coordinated at  $(t = t + \Delta t)$  from the coordinate at  $(t = t)$  and  $(t = t - \Delta t)$ , and force apply to  $i$ -th atom at  $(t = t)$ . The velocity of  $i$ -th atom is possible to obtain by same procedure.

$$\mathbf{v}_i(t) = \frac{1}{2\Delta t}[\mathbf{r}_i(t + \Delta t) - \mathbf{r}_i(t - \Delta t)] \quad (3.6)$$

where  $\mathbf{v}_i(t)$  is the velocity of  $i$ -th atom. The value of  $\Delta t$  should be chosen properly so as to reproduce physical properties.

## 3.2 Symplectic molecular dynamics method

### Symplectic Condition

I denote the pair of generalized coordinates  $\mathbf{q}$  and generalized momentum  $\mathbf{p}$  as follows.

$$\Gamma = \begin{pmatrix} \mathbf{p} \\ \mathbf{q} \end{pmatrix} \quad (3.7)$$

$\mathbf{p}$  and  $\mathbf{q}$  have  $3N$  component if the system is composed of  $N$  atoms. The time evolution of coordinates and momentum can be written as follows by canonical equation,

$$\frac{dq_i}{dt} = \frac{\partial H}{\partial p_i}, \quad \frac{dp_i}{dt} = -\frac{\partial H}{\partial q_i} \quad (3.8)$$

where  $H$  is Hamiltonian of the system. The time evolution can be written as follows by use of  $\mathbf{\Gamma}$ ,

$$\frac{d}{dt}\mathbf{\Gamma} = \mathbf{J} \frac{\partial H}{\partial \mathbf{\Gamma}} \quad (3.9)$$

where  $\mathbf{J}$  is  $6N \times 6N$  matrix as follows

$$\mathbf{J} = \begin{pmatrix} \mathbf{0} & \mathbf{1} \\ -\mathbf{1} & \mathbf{0} \end{pmatrix} \quad (3.10)$$

where  $\mathbf{1}$  is the  $3N \times 3N$  unit matrix. Now I consider the non-time dependent canonical transformation of  $\mathbf{\Gamma}$  to pair of other coordination and momentum,  $\mathbf{\Gamma}'$ .

$$\mathbf{\Gamma}' = \begin{pmatrix} \mathbf{p}'(\mathbf{p}, \mathbf{q}) \\ \mathbf{q}'(\mathbf{p}, \mathbf{q}) \end{pmatrix} \quad (3.11)$$

Canonical equation about  $\mathbf{\Gamma}'$  holds since  $\mathbf{\Gamma}'$  is derived by canonical transformation of  $\mathbf{\Gamma}$ .

$$\frac{d}{dt}\mathbf{\Gamma}' = \mathbf{J} \frac{\partial H}{\partial \mathbf{\Gamma}'} \quad (3.12)$$

The time evolution of  $\mathbf{\Gamma}'$  can be written as follows by considering that  $\mathbf{\Gamma}'$  is the function of  $\mathbf{\Gamma}$ .

$$\begin{aligned}
\frac{d}{dt} \Gamma'_i &= \sum_{j=1}^{6N} \frac{\partial \Gamma'_i}{\partial \Gamma_j} \frac{d}{dt} \Gamma_j = \sum_{j=1}^{6N} M_{ij} \frac{d}{dt} \Gamma_j = \sum_{j,k=1}^{6N} M_{ij} J_{jk} \frac{\partial H}{\partial \Gamma_k} = \sum_{j,k,l=1}^{6N} M_{ij} J_{jk} \frac{\partial \Gamma'_l}{\partial \Gamma_k} \frac{\partial H}{\partial \Gamma_l} \\
&= \sum_{j,k,l=1}^{6N} M_{ij} J_{jk} M_{lk} \frac{\partial H}{\partial \Gamma_l}
\end{aligned} \tag{3.13}$$

That is,

$$\mathbf{\Gamma}' = \mathbf{M} \mathbf{T} \mathbf{M}^T \frac{\partial H}{\partial \mathbf{\Gamma}} \tag{3.14}$$

where  $\mathbf{M}$  is Jacobian matrix as follows.

$$M_{ij} = \frac{\partial \Gamma'_i}{\partial \Gamma_j} \tag{3.15}$$

Comparing (3.12) and (3.14),

$$\mathbf{M} \mathbf{J} \mathbf{M}^T = \mathbf{J} \tag{3.16}$$

(3.16) holds. (3.16) called symplectic condition. When the generalized coordinates  $\mathbf{q}$  and generalized momentum  $\mathbf{p}$  temporally develop according to the Hamiltonian, the time evolution after  $\Delta t$  can be considered as canonical transformation since the both pair follow the canonical equation with same Hamiltonian.

$$\begin{pmatrix} \mathbf{q}(t) \\ \mathbf{p}(t) \end{pmatrix} \rightarrow \begin{pmatrix} \mathbf{q}(t + \Delta t) \\ \mathbf{p}(t + \Delta t) \end{pmatrix} \tag{3.17}$$

The time evolution of generalized coordinates and generalized momentum derived from Hamiltonian satisfies the symplectic condition (3.16) since canonical transformation (3.17) holds symplectic condition. The ‘real’ body moves symplectic condition. In the computation of solving equation of motion, does symplectic condition hold?

### Derivation of Verlet Algorithm from symplectic condition

Time evolution of an arbitral physical quantity  $A$  which written as a function of  $\mathbf{q}$  and  $\mathbf{p}$  is written as follows.

$$\frac{dA}{dt} = \sum_{i=1}^{3N} \left( \frac{\partial A}{\partial q_i} \frac{dq_i}{dt} + \frac{\partial A}{\partial p_i} \frac{dp_i}{dt} \right) = \sum_{i=1}^{3N} \left( \frac{\partial A}{\partial q_i} \frac{\partial H}{\partial p_i} + \frac{\partial A}{\partial p_i} \frac{\partial H}{\partial q_i} \right) \quad (3.18)$$

I here define operator  $D_H$  as follows.

$$D_H \equiv \sum_{i=1}^{3N} \left( \frac{\partial H}{\partial p_i} \frac{\partial}{\partial q_i} + \frac{\partial H}{\partial q_i} \frac{\partial}{\partial p_i} \right) \quad (3.19)$$

Then the time evolution of  $A$  can be written as follows.

$$\frac{dA}{dt} = D_H A \quad (3.20)$$

The formal solution of (3.20) is written as follows.

$$A(t + \Delta t) = e^{D_H \Delta t} A(t) \quad (3.21)$$

If the Hamiltonian can be decomposed into momentum-dependent and coordination-dependent term as follows,

$$H(\mathbf{q}, \mathbf{p}) = K(\mathbf{p}) + U(\mathbf{q}) \quad (3.22)$$

then the operator  $D_H$  can be decomposed.

$$D_H = \sum_{i=1}^{3N} \frac{\partial K}{\partial p_i} \frac{\partial}{\partial q_i} - \sum_{i=1}^{3N} \frac{\partial U}{\partial q_i} \frac{\partial}{\partial p_i} = D_K + D_U \quad (3.23)$$

$$D_K \equiv \sum_{i=1}^{3N} \frac{\partial K}{\partial p_i} \frac{\partial}{\partial q_i}, \quad D_U \equiv - \sum_{i=1}^{3N} \frac{\partial U}{\partial q_i} \frac{\partial}{\partial p_i} \quad (3.24)$$

The time evolution operator  $e^{D_H \Delta t}$  can be decomposed by using Suzuki-Trotter decomposition.

$$e^{D_H \Delta t} = e^{D_U \frac{\Delta t}{2}} e^{D_K \Delta t} e^{D_U \frac{\Delta t}{2}} + O(\Delta t^3) \quad (3.25)$$

The operators  $e^{D_U \Delta t}$  and  $e^{D_K \Delta t}$  are the time evolution operator which  $U$  and  $K$  are considered as Hamiltonian, respectively. This means symplectic condition holds in time evolution using time evolution operator above. Consequently, symplectic condition holds in time evolution with operator  $e^{D_U \frac{\Delta t}{2}} e^{D_K \Delta t} e^{D_U \frac{\Delta t}{2}}$  because each part of operator satisfies symplectic condition. The operations using  $D_K$  and  $D_U$  to  $\mathbf{p}$  and  $\mathbf{q}$  are written as follows.

$$D_K q_i = \frac{\partial K}{\partial p_i}, \quad D_K^2 q_i = 0, \quad D_U q_i = 0, \quad D_U p_i = \frac{\partial U}{\partial q_i}, \quad D_U^2 p_i = 0, \quad D_K p_i = 0 \quad (3.26)$$

The time evolution of  $\mathbf{p}$  and  $\mathbf{q}$  can be written as follows by using (3.26).

$$e^{D_K \Delta t} q_i = \left( 1 + D_K \Delta t + \frac{1}{2} D_K^2 \Delta t^2 + \dots \right) q_i = q_i + \frac{\partial K}{\partial p_i} \Delta t \quad (3.27)$$

$$e^{D_K \Delta t} p_i = p_i \quad (3.28)$$

$$e^{D_U \Delta t} q_i = q_i \quad (3.28)$$

$$e^{D_U \Delta t} p_i = p_i - \frac{\partial U}{\partial q_i} \Delta t \quad (3.29)$$

When the Hamiltonian is written using the coordinates of  $i$ -th particle,  $\mathbf{r}_i$  and its momentum  $\mathbf{p}_i$  as follows,

$$H = \sum_{i=1}^N \frac{\mathbf{p}_i^2}{2m_i} + U(\mathbf{r}_i) \quad (3.30)$$

The time evolution of the system can be written as follows using the time evolution operator (3.25),

$$\mathbf{p}_i^{n+\frac{1}{2}} = \mathbf{p}_i^n - \frac{\partial U^n}{\partial \mathbf{r}_i^n} \frac{\Delta t}{2} \quad (3.31)$$

$$\mathbf{r}_i^{n+1} = \mathbf{r}_i^n + \frac{\mathbf{p}_i^{n+\frac{1}{2}}}{m_i} \Delta t \quad (3.32)$$

$$\mathbf{p}_i^{n+1} = \mathbf{p}_i^{n+\frac{1}{2}} - \frac{\partial U^{n+1}}{\partial \mathbf{r}_i^{n+1}} \frac{\Delta t}{2} \quad (3.33)$$

where n is step in solving difference equation. The equations (3.31-33) is called velocity-Verlet algorithm. Verlet algorithm satisfies symplectic condition because Verlet algorithm can be derived from velocity-Verlet algorithm which satisfies symplectic condition.

### Conservative quantity in symplectic condition

Baker-Campbell-Hausdorff formula is written as follows.

$$e^A e^B = e^C \quad (3.34)$$

If (3.34) holds in any operator A, B and C, then the formula written below holds,

$$C = A + B + \frac{1}{2}[A, B] + \frac{1}{12}\{[A, [A, B]] + [[A, B], B]\} + \dots \quad (3.35)$$

where [ , ] is commutator defined as follows.

$$[A, B] \equiv AB - BA \quad (3.36)$$

I here apply the Baker-Campbell-Hausdorff formula to the relation below.

$$e^C = e^{\frac{A}{2}} e^B e^{\frac{A}{2}} \quad (3.37)$$

Then,

$$C = \frac{1}{2}A + B - \frac{1}{24}[A, [A, B]] + \frac{1}{12}[[A, B]B] + \dots \quad (3.38)$$

(3.38) can be obtained.

Here I define the time evolution operator as follows.

$$e^{D_{H'}\Delta t} \equiv e^{D_U\frac{\Delta t}{2}} e^{D_K\Delta t} e^{D_U\frac{\Delta t}{2}} \quad (3.39)$$

And then, the time evolution operator  $e^{D_{H'}\Delta t}$  become as follows.

$$D_{H'} = D_K + D_U + \frac{1}{24} \left( 2[[D_U, D_K], D_K] - [D_U, [D_U, D_K]] \right) \Delta t^2 + \dots \quad (3.40)$$

To express (3.40) using Poisson's bracket, the terms in (3.40) become as follows

$$D_K + D_U = \sum_{i=1}^{3N} \frac{\partial H}{\partial p_i} \frac{\partial}{\partial q_i} - \sum_{i=1}^{3N} \frac{\partial H}{\partial q_i} \frac{\partial}{\partial p_i} = \{, H\} = D_H \quad (3.41)$$

$$[D_U, D_K] = - \left\{ , \sum_{i=1}^{3N} \frac{\partial H}{\partial p_i} \frac{\partial H}{\partial q_i} \right\} \quad (3.42)$$

$$[D_U, [D_U D_K]] = \left\{ , \sum_{i=1}^{3N} \sum_{j=1}^{3N} \frac{\partial H}{\partial q_i} \frac{\partial^2 H}{\partial p_i \partial p_j} \frac{\partial H}{\partial q_j} \right\} \quad (3.43)$$

$$[[D_U D_K], D_K] = \left\{ , \sum_{i=1}^{3N} \sum_{j=1}^{3N} \frac{\partial H}{\partial p_i} \frac{\partial^2 H}{\partial q_i \partial q_j} \frac{\partial H}{\partial p} \right\} \quad (3.44)$$

And then,

$$D_{H'} = \{, H\} + \left\{ \frac{1}{24} \left( 2 \sum_{i=1}^{3N} \sum_{j=1}^{3N} \frac{\partial H}{\partial p_i} \frac{\partial^2 H}{\partial q_i \partial q_j} \frac{\partial H}{\partial p} - \sum_{i=1}^{3N} \sum_{j=1}^{3N} \frac{\partial H}{\partial q_i} \frac{\partial^2 H}{\partial p_i \partial p_j} \frac{\partial H}{\partial q_j} \right) \right\} \Delta t^2$$

$$+ \dots \quad (3.45)$$

(3.45) is obtained. This means that quasi-Hamiltonian  $H'$  as follows conserves in the

Verlet algorithm.

$$H' \equiv H + \frac{1}{24} \left( 2 \sum_{i=1}^{3N} \sum_{j=1}^{3N} \frac{\partial H}{\partial p_i} \frac{\partial^2 H}{\partial q_i \partial q_j} \frac{\partial H}{\partial p} - \sum_{i=1}^{3N} \sum_{j=1}^{3N} \frac{\partial H}{\partial q_i} \frac{\partial^2 H}{\partial p_i \partial p_j} \frac{\partial H}{\partial q_j} \right) \Delta t^2 + \dots \quad (3.46)$$

Consequently, the Verlet algorithm is suitable for MD simulation because

quasi-Hamiltonian conserves and the simulated system become stable.

### 3.3 Ewald summation

Treatments of long-ranged force terms such as the Coulombic interactions must be optimized in order to reduce the calculation costs. The Ewald summation is an efficient method to calculate the Coulombic interactions in periodic boundary conditions. In the Ewald summations, the Coulombic interactions are decomposed into two terms which are real space and wave number space terms. The real space term can be calculated by direct summations within a limited cut-off distance. The wave number space term can be calculated by Fourier transformation using periodic boundary conditions within a limited cut-off distance in the reciprocal space.

Coulombic potential  $\Phi$  is written by following form,

$$\Phi_i = \sum_{n, n \neq 0} \sum_{j, j \neq i} \frac{e^2}{4\pi\epsilon_0} \frac{q_i q_j}{|\mathbf{r}_i - \mathbf{r}_j + \mathbf{n}\mathbf{C}|} \quad (3.47)$$

where  $\epsilon_0$  is the permittivity of vacuum,  $e$  is the elemental charge,  $\mathbf{r}_i$  is the coordinates of  $i$ -th atom,  $\mathbf{C}$  is the unit cell matrix, and  $q_i$  is partial charge of  $i$ -th atom. Firstly, I introduce the function below.

$$a(r) = \frac{1}{r} \quad (3.48)$$

Then, (3.47) become as follows.

$$\Phi_i = \sum_{n, n \neq 0} \sum_{j, j \neq i} \frac{e^2 q_i q_j}{4\pi\epsilon_0} a(|\mathbf{r}_i - \mathbf{r}_j + \mathbf{n}\mathbf{C}|) \quad (3.49)$$

Here I introduce the new function  $a_0(r)$  which shows similar attenuation to the function  $a(r)$ .

$$a_1(r) = a(r) - a_0(r) \quad (3.50)$$

The function  $a_0(r)$  will be chosen as  $a_1(|\mathbf{C}|/2) \ll 1$ . Then, (3.49) become as follows by addition and subtraction of  $a_0$ .

$$\begin{aligned} \Phi_i &= \sum_{n, n \neq 0} \sum_{j, j \neq i} \frac{e^2 q_i q_j}{4\pi\epsilon_0} [a(|\mathbf{r}_i - \mathbf{r}_j + \mathbf{n}\mathbf{C}|) - a_0(|\mathbf{r}_i - \mathbf{r}_j + \mathbf{n}\mathbf{C}|)] \\ &+ \sum_{n, n \neq 0} \sum_{j, j \neq i} \frac{e^2 q_i q_j}{4\pi\epsilon_0} a_0(|\mathbf{r}_i - \mathbf{r}_j + \mathbf{n}\mathbf{C}|) = \Phi_i^{real} + \Phi_i^{wave+corr} \end{aligned} \quad (3.51)$$

$\Phi_i^{real}$  is a function which rapidly converges to zero.  $\Phi_i^{wave+corr}$  is a function which

slowly attenuates. I here add and subtract the term in which  $\mathbf{n} = 0$  and  $i = j$ .

$$\begin{aligned}\Phi_i^{wave+corr} &= \sum_{\mathbf{n}} \sum_j \frac{e^2 q_i q_j}{4\pi\epsilon_0} a_0(|\mathbf{r}_i - \mathbf{r}_j + \mathbf{n}\mathbf{C}|) - \frac{e^2 q_i^2}{4\pi\epsilon_0} a_0(0) \\ &= \Phi_i^{wave} + \Phi_i^{corr}\end{aligned}\quad (3.52)$$

Fourier series expansion can be used for  $\Phi_i^{wave}$  because  $\Phi_i^{wave}$  is the summation of the periodic system.

$$\Phi_i^{wave} = \sum_{\mathbf{n}} \sum_j \frac{e^2 q_i q_j}{4\pi\epsilon_0} \frac{1}{(2\pi)^3} \int \int d\mathbf{r} d\mathbf{k} a_0(\mathbf{r}) e^{(-i\mathbf{k}\cdot\mathbf{r})} e^{[i\mathbf{k}\cdot(\mathbf{r}_i - \mathbf{r}_j + \mathbf{n}\mathbf{C})]} \quad (3.53)$$

(3.54) can be used for (3.53) because  $\mathbf{n}\mathbf{C}$  covers whole space.

$$\sum_{\mathbf{n}} e^{i\mathbf{k}\cdot\mathbf{n}\mathbf{C}} = \frac{(2\pi)^2}{|\mathbf{C}|} \sum_{\mathbf{G}} \delta(\mathbf{k} - \mathbf{G}) \quad (3.54)$$

where  $\mathbf{G}$  is reciprocal lattice vector written as follows.

$$\mathbf{C} = \begin{pmatrix} \mathbf{C}_a \\ \mathbf{C}_b \\ \mathbf{C}_c \end{pmatrix} \quad (3.55)$$

$$\mathbf{C}_a^* = \frac{\mathbf{C}_b \times \mathbf{C}_c}{\mathbf{C}_a \cdot (\mathbf{C}_b \times \mathbf{C}_c)}, \quad \mathbf{C}_b^* = \frac{\mathbf{C}_c \times \mathbf{C}_a}{\mathbf{C}_a \cdot (\mathbf{C}_b \times \mathbf{C}_c)}, \quad \mathbf{C}_c^* = \frac{\mathbf{C}_a \times \mathbf{C}_b}{\mathbf{C}_a \cdot (\mathbf{C}_b \times \mathbf{C}_c)} \quad (3.56)$$

$$\mathbf{G} = 2\pi(h\mathbf{C}_a^* + k\mathbf{C}_b^* + l\mathbf{C}_c^*) \quad (h, k, l \in \mathbf{Z}) \quad (3.57)$$

Then,  $\Phi_i^{wave}$  become as follows.

$$\begin{aligned}\Phi_i^{wave} &= \frac{1}{|\mathbf{C}|} \sum_j \frac{e^2 q_i q_j}{4\pi\epsilon_0} \frac{1}{(2\pi)^3} \sum_{\mathbf{G}} \int \int d\mathbf{r} d\mathbf{k} a_0(\mathbf{r}) e^{(-i\mathbf{k}\cdot\mathbf{r})} \sum_{\mathbf{G}} \delta(\mathbf{k} - \mathbf{G}) e^{[i\mathbf{k}\cdot(\mathbf{r}_i - \mathbf{r}_j)]} \\ &= \frac{1}{|\mathbf{C}|} \sum_{\mathbf{G}} \int d\mathbf{r} a_0(\mathbf{r}) e^{(-i\mathbf{G}\cdot\mathbf{r})} \sum_j \frac{e^2 q_i q_j}{4\pi\epsilon_0} e^{[i\mathbf{G}\cdot(\mathbf{r}_i - \mathbf{r}_j)]}\end{aligned}\quad (3.58)$$

The function for  $a_0$  might be a function of potential energy of charge  $Q$  at  $\mathbf{r}$  in the

electric field made by charge distribution which only depends on the distance from the center  $\mathbf{r}'$ . In Ewald's method, the Gaussian distribution is used for charge distribution as follows,

$$\rho_0(\mathbf{r} - \mathbf{r}') = \rho_0(r) = Q' \left( \frac{\alpha^2}{\pi} \right)^{\frac{3}{2}} e^{-(\alpha r)^2} \quad (3.59)$$

where  $\alpha$  is the parameter indicating the variance of the charge distribution. The electric field  $\varphi_0$  can be obtained from Poisson's equation as follows.

$$\Delta\varphi_0 = -\frac{\rho_0}{\varepsilon_0} \quad (3.60)$$

(3.60) can easily be solved using polar coordinates because (3.59) does not depend on the angular components.

$$\frac{\partial^2 r\varphi_0}{\partial r^2} = -\frac{Q'}{\varepsilon_0} \left( \frac{\alpha^2}{\pi} \right)^{\frac{3}{2}} r e^{-(\alpha r)^2} \quad (3.61)$$

The electric potential made by the Gaussian-distributed charge is written bellow.

$$\left. \frac{\partial r\varphi_0}{\partial r} \right|_{r=\infty} = a_{0r=\infty} + r \left. \frac{\partial \varphi_0}{\partial r} \right|_{r=\infty} = 0 \quad (3.62)$$

Then, (3.61) becomes as follows by integrating the both sides from  $\infty$  to  $r$ .

$$\begin{aligned} \frac{\partial r\varphi_0}{\partial r} &= -\frac{Q'}{\varepsilon_0} \left( \frac{\alpha^2}{\pi} \right)^{\frac{3}{2}} \int_{\infty}^r r e^{-(\alpha r)^2} dr = -\frac{Q'}{\varepsilon_0} \left( \frac{\alpha^2}{\pi} \right)^{\frac{3}{2}} \left[ -\frac{1}{2\alpha^2} e^{-(\alpha r)^2} \right]_{\infty}^r \\ &= \frac{Q'}{\varepsilon_0} \left( \frac{1}{\pi} \right)^{\frac{3}{2}} \alpha e^{-(\alpha r)^2} \end{aligned} \quad (3.63)$$

Again, (3.63) becomes as follows by integrating the both sides from 0 to  $r$ .

$$r\varphi_0(r) = \frac{Q'}{4\pi\varepsilon_0} 2 \left( \frac{\alpha^2}{\pi} \right)^{\frac{1}{2}} \int_0^r e^{-(ar)^2} dr \quad (3.64)$$

The integration can be solved by the variable transformation  $ar = x$ .

$$\begin{aligned} r\varphi_0(r) &= \frac{Q'}{4\pi\varepsilon_0} 2 \left( \frac{\alpha^2}{\pi} \right)^{\frac{1}{2}} \int_0^{ar} e^{-x^2} \frac{dr}{dx} dx \\ &= \frac{Q'}{4\pi\varepsilon_0} \frac{2}{\sqrt{\pi}} \int_0^{ar} e^{-x^2} dx = \frac{Q'}{4\pi\varepsilon_0} \operatorname{erf}(ar) \end{aligned} \quad (3.65)$$

As a result, the electric field  $\varphi_0$  and function  $a_0(r)$  are found as follow.

$$\varphi_0(r) = \frac{Q'}{4\pi\varepsilon_0} \frac{\operatorname{erf}(ar)}{r}, \quad a_0 = \frac{4\pi\varepsilon_0}{Q'} \varphi_0(r) = \frac{\operatorname{erf}(ar)}{r} \quad (3.66)$$

Then  $\Phi_i^{real}$  is found as follows postulating the rapid convergence.

$$\begin{aligned} \Phi_i^{real} &= \sum_{n, n \neq 0} \sum_{j, j \neq i} \frac{e^2 q_i q_j}{4\pi\varepsilon_0} \frac{1}{|\mathbf{r}_i - \mathbf{r}_j + n\mathbf{C}|} [1 - \operatorname{erf}(\alpha|\mathbf{r}_i - \mathbf{r}_j + n\mathbf{C}|)] \\ &= \sum_{n, n \neq 0} \sum_{j, j \neq i} \frac{e^2 q_i q_j}{4\pi\varepsilon_0} \frac{\operatorname{erfc}(\alpha|\mathbf{r}_i - \mathbf{r}_j + n\mathbf{C}|)}{|\mathbf{r}_i - \mathbf{r}_j + n\mathbf{C}|} \\ &= \sum_{j, j \neq i} \frac{e^2 q_i q_j}{4\pi\varepsilon_0} \frac{\operatorname{erfc}(\alpha|\mathbf{r}_i - \mathbf{r}_j|)}{|\mathbf{r}_i - \mathbf{r}_j|} \end{aligned} \quad (3.67)$$

Here I derive the Fourier integration in (3.58) to find  $\Phi_i^{wave}$ . The formula of Fourier integration about differentiation is written as follows.

$$\int \Delta\varphi_0(\mathbf{r}) e^{(-i\mathbf{G} \cdot \mathbf{r})} d\mathbf{r} = -\mathbf{G}^2 \int \varphi_0(\mathbf{r}) e^{(-i\mathbf{G} \cdot \mathbf{r})} d\mathbf{r} \quad (3.68)$$

Then, (3.69) can be obtained substituting (3.60).

$$\int \frac{Q'}{\varepsilon_0} \left( \frac{\alpha^2}{\pi} \right)^{\frac{3}{2}} e^{-(ar)^2} e^{(-i\mathbf{G} \cdot \mathbf{r})} d\mathbf{r} = -\mathbf{G}^2 \int \varphi_0(\mathbf{r}) e^{(-i\mathbf{G} \cdot \mathbf{r})} d\mathbf{r}$$

$$\frac{Q'}{\varepsilon_0 |\mathbf{G}|^2} \left( \frac{\alpha^2}{\pi} \right)^{\frac{3}{2}} \int e^{-(\alpha r)^2} e^{-i\mathbf{G} \cdot \mathbf{r}} d\mathbf{r} = \int \varphi_0(\mathbf{r}) e^{-i\mathbf{G} \cdot \mathbf{r}} d\mathbf{r} \quad (3.69)$$

The direction of  $\mathbf{G}$  is selected as z axis.

$$\begin{aligned} \frac{Q'}{\varepsilon_0 |\mathbf{G}|^2} \left( \frac{\alpha^2}{\pi} \right)^{\frac{3}{2}} \int_0^{2\pi} \int_0^\pi \int_0^\infty e^{-(\alpha r)^2} e^{-i|\mathbf{G}||r|\cos\theta} r^2 \sin\theta dr d\theta d\varphi &= \int \varphi_0(\mathbf{r}) e^{-i\mathbf{G} \cdot \mathbf{r}} d\mathbf{r} \\ \frac{Q'}{\varepsilon_0 |\mathbf{G}|^2} \left( \frac{\alpha^2}{\pi} \right)^{\frac{3}{2}} \int_0^\infty \frac{2\pi r^2 e^{-(\alpha r)^2}}{i|\mathbf{G}||r|} [e^{(-i|\mathbf{G}||r|\cos\theta)}]_0^\pi dr &= \int \varphi_0(\mathbf{r}) e^{-i\mathbf{G} \cdot \mathbf{r}} d\mathbf{r} \\ \frac{Q'}{\varepsilon_0 |\mathbf{G}|^2} \left( \frac{\alpha^2}{\pi} \right)^{\frac{3}{2}} \int_0^\infty \frac{2\pi r e^{-(\alpha r)^2}}{i|\mathbf{G}|} [e^{(-i|\mathbf{G}||r|)} - e^{(-i|\mathbf{G}||r|)}] dr &= \int \varphi_0(\mathbf{r}) e^{-i\mathbf{G} \cdot \mathbf{r}} d\mathbf{r} \\ \frac{Q'}{\varepsilon_0 |\mathbf{G}|^2} \left( \frac{\alpha^2}{\pi} \right)^{\frac{3}{2}} \int_0^\infty \frac{2\pi}{i|\mathbf{G}|} r e^{-(\alpha r)^2} 2i \sin(|\mathbf{G}||r|) dr &= \int \varphi_0(\mathbf{r}) e^{-i\mathbf{G} \cdot \mathbf{r}} d\mathbf{r} \end{aligned} \quad (3.70)$$

The Fourier part of (3.58) become as follows using variable transformation  $x = ar$ .

$$\begin{aligned} \frac{Q'}{\varepsilon_0 |\mathbf{G}|^2} \left( \frac{\alpha^2}{\pi} \right)^{\frac{3}{2}} \int_0^\infty \frac{4\pi x}{|\mathbf{G}| \alpha} e^{-x^2} \sin\left(\frac{|\mathbf{G}|x}{\alpha}\right) \frac{dr}{dx} dx &= \int \varphi_0(\mathbf{r}) e^{-i\mathbf{G} \cdot \mathbf{r}} d\mathbf{r} \\ \frac{Q'}{\varepsilon_0 |\mathbf{G}|^2} \left( \frac{\alpha^2}{\pi} \right)^{\frac{3}{2}} \frac{4\pi}{|\mathbf{G}|} \frac{1}{\alpha} \frac{1}{\alpha} \frac{\sqrt{\pi}}{4} \frac{|\mathbf{G}|}{\alpha} e^{-\left(\frac{|\mathbf{G}|^2}{4\alpha^2}\right)} &= \int \varphi_0(\mathbf{r}) e^{-i\mathbf{G} \cdot \mathbf{r}} d\mathbf{r} \\ \frac{Q'}{\varepsilon_0 |\mathbf{G}|^2} e^{-\left(\frac{|\mathbf{G}|^2}{4\alpha^2}\right)} &= \int \varphi_0(\mathbf{r}) e^{-i\mathbf{G} \cdot \mathbf{r}} d\mathbf{r} \\ \int a_0(\mathbf{r}) e^{-i\mathbf{G} \cdot \mathbf{r}} d\mathbf{r} &= \frac{4\pi}{|\mathbf{G}|^2} e^{-\left(\frac{|\mathbf{G}|^2}{4\alpha^2}\right)} \end{aligned} \quad (3.71)$$

Then  $\Phi_i^{wave}$  become as follows.

$$\begin{aligned}
& \frac{1}{|\mathcal{C}|} \sum_{\mathbf{G}} \int d\mathbf{r} a_0(\mathbf{r}) e^{-i\mathbf{G} \cdot \mathbf{r}} \sum_j \frac{e^2 q_i q_j}{4\pi\epsilon_0} e^{i\mathbf{G} \cdot (\mathbf{r}_i - \mathbf{r}_j)} \\
&= \frac{1}{|\mathcal{C}|} \sum_{\mathbf{G}} \frac{4\pi}{|\mathbf{G}|^2} e^{-\left(\frac{|\mathbf{G}|^2}{4\alpha^2}\right)} \sum_j \frac{e^2 q_i q_j}{4\pi\epsilon_0} [\cos\{\mathbf{G} \cdot (\mathbf{r}_i - \mathbf{r}_j)\} \\
&+ i\sin\{\mathbf{G} \cdot (\mathbf{r}_i - \mathbf{r}_j)\}] \tag{3.72}
\end{aligned}$$

There are pairs of reciprocal lattice vector such as  $\mathbf{G} = -\mathbf{G}'$  because the summation about  $\mathbf{G}$  includes whole reciprocal space. Then  $\Phi_i^{wave}$  can be obtained as follows.

$$\Phi_i^{wave} = \frac{e^2 q_i}{|\mathcal{C}|\epsilon_0} \sum_{\mathbf{G}} \frac{1}{|\mathbf{G}|^2} e^{-\left(\frac{|\mathbf{G}|^2}{4\alpha^2}\right)} \sum_j q_j \cos\{\mathbf{G} \cdot (\mathbf{r}_i - \mathbf{r}_j)\} \tag{3.73}$$

$\Phi_i^{corr}$  can be obtained using Maclaurin expansion.

$$\begin{aligned}
\Phi_i^{corr} &= \frac{e^2 q_i^2}{4\pi\epsilon_0} a_0(0) = \frac{e^2 q_i^2}{4\pi\epsilon_0} \frac{\text{erf}(ar)}{r} = \frac{e^2 q_i^2}{4\pi\epsilon_0} \lim_{r \rightarrow 0} \frac{1}{r} \frac{2}{\sqrt{\pi}} \left( ar - \frac{(\alpha r)^3}{3} + \dots \right) \\
&= \frac{e^2 q_i^2}{2\pi\epsilon_0} \frac{\alpha}{\sqrt{\pi}} \tag{3.74}
\end{aligned}$$

### 3.4 Calculation of the physical properties from MD

#### Static properties

The static properties can be obtained from the molecular dynamics simulations by thermo-dynamical theory excluding entropy. The internal energy,  $U$  is written as follows,

$$U = \left\langle \sum_i \Phi_i \right\rangle + \left\langle \frac{1}{2} \sum_i m_i \mathbf{v}_i^2 \right\rangle \tag{3.75}$$

where  $\Phi_i$  is the potential energy of  $i$ -th atom,  $m_i$  is the mass of  $i$ -th atom and  $\mathbf{v}_i$  is the

velocity of  $i$ -th atom. The temperature,  $T$  is written as follows by the law of equipartition of energy,

$$T = \frac{1}{3Nk_B} \left\langle \sum_i \frac{1}{2} m_i \mathbf{v}_i^2 \right\rangle \quad (3.76)$$

where  $N$  is the number of the atom in unit cell and  $k_B$  is the Boltzmann's constant. The pressure,  $P$  is derived from virial theorem as follows,

$$P = \frac{1}{3V} \left( 3Nk_B \langle T \rangle + \left\langle \sum_i \nabla \phi_i \cdot \mathbf{r}_i \right\rangle \right) \quad (3.77)$$

where  $V$  is the volume of the unit cell and  $\mathbf{r}_i$  is the coordinates of  $i$ -th atom.

The radial distribution function of atoms is the useful properties for explaining or understanding the structure of non-crystalline materials, easily comparable with experimental data by X-ray diffraction by weighting of electron density, and theoretically important for statistical physics of liquids. The radial distribution function,  $g(r)$  is defined as following form using Dirac's delta function.

$$g(r) = \frac{V}{N^2} \left\langle \sum_i \sum_{j(i < j)} \delta(r - |\mathbf{r}_{ij}|) \right\rangle \quad (3.78)$$

The function  $g(r)$  can be obtained for desired pairs of elements because the trajectory of each atoms can be obtained in molecular dynamics simulations. The function  $g(r)$  which calculated about is called pair correlation function.

## Dynamics properties

The auto-correlation function is a fundamental function which is obtained from molecular dynamics simulation to calculate dynamics properties. The auto-correlation function is defined as follows,

$$\langle A(t)A(0) \rangle = \frac{1}{N} \sum_{i=1}^N A(t_i + t)A(t_i) \quad (3.79)$$

where  $A(x)$  is a certain physical quantity,  $t$  is the time and  $t_i$  is the step of the simulation.

This means the auto-correlation function indicates the ensemble average of the correlation between the certain physical quantity and that after time  $t$ .

Many dynamics properties can be obtained by linear response theory. The linear response theory is written as follows,

$$\mathbf{B}(t) - \mathbf{B}^{eq} = \mathbf{L}\mathbf{X}(t) \quad (3.80)$$

where  $\mathbf{B}(t)$  is the value of flux which has a linear relation with force at time  $t$ ,  $\mathbf{B}^{eq}$  is the value of  $\mathbf{B}(t)$  at equilibrium,  $\mathbf{L}$  is the transfer coefficient matrix and  $\mathbf{X}(t)$  is the force at time  $t$ . Considering the time delay of response, (3.80) should be extended as non-Markovian form as follows,

$$\mathbf{B}(t) - \mathbf{B}^{eq} = \mathbf{L}\mathbf{X}(t) + \int_{-\infty}^t ds \boldsymbol{\varphi}(t-s) \mathbf{X}(s) \quad (3.81)$$

where the matrix  $\boldsymbol{\varphi}$  is the function indicating the time delay. Here omitting details,

Kubo-Green equation is derived from (3.81) as follows.

$$L = \frac{V}{k_B T} \int_0^\infty \langle B(t)B(0) \rangle dt \quad (3.82)$$

For example, shear viscosity  $\eta$  can be obtained when the stress is chosen as flux,

$$\eta = \frac{V}{k_B T} \int_0^\infty \langle \sigma_{ij}(t)\sigma_{ij}(0) \rangle dt \quad (3.83)$$

where  $\sigma_{ij}$  is the off-diagonal component of stress tensor. Self-diffusion coefficient  $D$  also can be obtained by choosing the velocity of atom as flux and adjusting the dimension as follows,

$$D = \int_0^\infty \langle \mathbf{v}_i(t)\mathbf{v}_i(0) \rangle dt \quad (3.84)$$

where  $\mathbf{v}_i$  is velocity of  $i$ -th atom. The convergence of auto-correlation function is generally slow. Therefore the Einstein relation as follows is used for obtaining the self-diffusion coefficient,

$$D = \lim_{t \rightarrow \infty} \frac{1}{6t} \frac{1}{N} \left\langle \sum_{i=1}^N |\mathbf{r}_i(t) - \mathbf{r}_i(t_0)|^2 \right\rangle \quad (3.85)$$

where  $t$  is the time,  $N$  is the number of atoms in unit cell,  $\mathbf{r}_i$  is the position of  $i$ -th atom and  $t_0$  is the reference time. The life time of bonding between atom is calculated from the time dependence of probability  $P(r, t)$ , the ensemble average of the existence probability of bonds between atoms of desired element and coordinated atoms those were presented at time zero, written as follows using Heaviside's function,

$$P(r, t) = \frac{1}{N} \left\langle \sum_i^N \sum_j^{N_{crd}} H_c[r - |\mathbf{r}_i(t) - \mathbf{r}_j(t)|] \right\rangle \quad (3.86)$$

where  $N$  is the number of atoms of desired element,  $N_{crd}$  is the number of atoms bonded with  $i$ -th atom,  $r$  is the maximum bond length and  $r_i$  is the position of  $i$ -th atom. The life time of bonding  $\tau$  is determined as follows.

$$P(r, \tau) = e^{-1} \quad (3.87)$$

The exchanging rate of bond can be obtained from inverse of the life time of the bonding.

#### **4. Nature of Si-O-Si bonding via molecular orbital calculation**

Understanding the nature of Si-O bonding and Si-O-Si bridging is important for mineralogy, material science and metallurgy. It is well known that the variation of Si-O-Si angle in silicates is caused by difference of composition, temperature and pressure. The change of angle of Si-O-Si bridging affects the strength of Si-O bonding. For instance, the increase of Si-O-Si angle decreases the Si-O bond length in coesite crystal (Gibbs et al., 1977). The decrease of Si-O-Si angle of liquid silicates as a result of compression is reported by various researchers (e.g. Navrotsky et al., 1985; Ohtani et al., 1985; Sakamaki et al., 2012). The decrease of Si-O-Si angle is thought to be the trigger of decrease of viscosity of liquid silicates. (Navrotsky et al., 1985; Noritake et al., 2012). Quantum chemical properties of Si-O-Si bridging is investigated to understand the relationship between Si-O-Si angle, Si-O bond length and its strength (e.g., Newton and Gibbs, 1981; Tsuneyuki, 1996; Kubicki and Sykes, 1993). Newton and Gibbs (1981) reports the pyrosilic acid molecule has energy minimum at Si-O-Si angle of  $145^\circ$  using STO-3G basis set (Hehre et al. 1969) by Hartree-Fock method. Tsuneyuki (1996) reports that the bending of Si-O-Si is not reproduced using double-zeta function basis set nevertheless the increase of the number of basis function generally increase the reproducibility. However, the nature of Si-O-Si bridgings seems not to be reproduced by

increase of basis function using Hartree-Fock method. In this paper, I show the molecular orbital calculation about pyrosilic acid molecule using post-Hartree-Fock method and more precise basis set to understand the nature of Si-O-Si bridging.

#### **4.1 Computational Method**

Molecular orbital calculations were performed using the GAUSSIAN 09 code. We firstly calculate the optimized structure of disiloxane by Hartree-Fock (HF), second-order Møller-Plesset perturbation theory (MP2) (Head-Gordon et al., 1988), and two density functional theory (Becke's density functional (Becke, 1988) with three correlation functionals by Lee, Yang and Parr (B3LYP, Lee et al., 1988), and generalized gradient approximation by Perdew, Burke and Ernzerhof (PBE, Perdew et al., 1996)) with 6-311G(d,p) split valence double zeta basis set (McLean and Chandler, 1980; Raghavachari et al., 1980). The optimized parameter by various model chemistry and experimental data by Almenningen et al. (1963) is shown in Table 4.1. The bending of Si-O-Si bridging is not reproduced by HF method as shown in Tsuneyuki (1966). The bending of Si-O-Si bridging is reproduced by use of MP2 and density functional theory with PBE. The optimized angle of Si-O-Si in disiloxane molecule by MP2 is closer to experimental value than that by PBE. Then we apply the MP2 method with 6-311G(d,p)

basis set to the calculation of pyrosilic acid,  $H_6Si_2O_7$ . In optimizing the molecular structure of pyrosilic acid, hydrogen bonding is made in the molecule as shown in Kubicki and Sykes (1993). I optimized with z-matrix to define the point symmetry of pyrosilic acid molecule to avoid the effect of hydrogen bonding. Two types of structure is optimized, one is the  $C_{2v}$  point symmetry as shown in Figure 4.1a, the other is structure in which each tetrahedra is in conformational relation of  $60^\circ$  torsion as shown in Figure 4.1b. The optimized parameter is shown in Table 4.2.

Then we calculate the energy surface of two pyrosilic acid molecules varying the Si-O(brd) bond length and Si-O-Si angle with fixing other parameters obtained by optimization. To analyze the bonding, I use the Natural Bonding Orbital (NBO) analysis method (Foster and Weinhold, 1980; Reed et al., 1985, 1988). NBO analysis originated as a technique for studying hybridization and covalency effects in molecular wave functions. In NBO analysis, the each calculated molecular orbitals are decomposed and recomposed visualized bond orbital that corresponds to the picture of interatomic bonds and lone pairs. It gives us energy of bonding, degree of hybridization of bonding, overlap integration weighted bond order and charge of atoms. In NBO analysis, I firstly define natural atomic orbital and attribute the electrons. Natural atomic orbital can be obtained by block diagonalization of density matrix by each angular momentum

of atomic orbital of each atoms. Then I define the  $sp^\lambda$  natural hybrid orbitals,  $h_\lambda(\theta)$  as follows,

$$h_\lambda(\theta) = N \left( s + \lambda^{\frac{1}{2}} p_\theta \right) \quad (1)$$

where  $p_\theta$  is a normalized p orbital pointing in the direction  $\theta$  and N is a normalization constant. Then I can obtain the natural bond orbital  $\sigma_{AB}$  between atom A and B from directed orthonormal hybrid orbitals  $h_A$  and  $h_B$  (natural hybrid orbitals) as follows,

$$\sigma_{AB} = c_A h_A + c_B h_B \quad (2)$$

where c is constant and calculated numerically from the result of density by molecular orbital calculations. More precise about NBO analysis is written in Foster and Weinhold (1980) and Reed et al. (1985, 1988).

### 4.3 Results and Discussion

The optimized parameter of pyrosilic molecules is shown in Table 4.2. Stable Si-O-Si angle and total energy of  $C_{2v}$  symmetry are larger than those of  $60^\circ$  torsion. However, the bond length between Si and bridging oxygen ( $O_{br}$ ) does not change significantly by change of torsion angle. Figure 4.2 and 4.3 are contour maps of potential energy surface of pyrosilic acid molecules ( $C_{2v}$  symmetry and  $60^\circ$  torsion) varying Si-O-Si angle and Si- $O_{br}$  length, respectively. The stable Si-O bond lengths

decreasing Si-O-Si angle in both molecules. The total energy at minimum of twisted pyrosilic at energy minimum is lower than that of molecule which has  $C_{2v}$  symmetry. Figure 4.4 shows sum of orbital energy of valence electrons of bridging oxygen and each orbitals, and overlap weighted bond order of Si-O<sub>br</sub>. The Sum of the orbital energy of valence electrons of bridging oxygen decrease with decreasing Si-O-Si angle. Decomposing into each orbital, orbital energy of sum of two lone pairs decrease with increasing Si-O-Si angle, however the orbital energy of Si-O bonding increase with decreasing Si-O-Si angle. Note that the calculated orbitals are decomposed based on natural Lewis and lone pairs those are orthogonal with each other. The overlap weighted bond order has locally minimum at 140 to 145 degree whereas the changes in orbital energy shows monotonic increase or decrease. Contribution ratio of d character of Si atom to  $\sigma$  bonding between Si and O atom is showed in Figure 4.5. The calculated point charge at Si and O<sub>br</sub> are also showed in Figure 4.5. In NBO analysis, the point charge at each atom is calculated from occupancy of natural atomic orbital. The absolute value of atomic charge increase with increasing Si-O-Si angle. Figure 4.6 shows the coefficient  $c_{Si}$  and  $c_O$  with varying Si-O-Si angle. The coefficient of  $c_{Si}$  decrease and  $c_O$  increase with increasing Si-O-Si angle.

The bending of Si-O-Si bridging is reproduced in this study using Møller-Plesset

perturbation theory and 6-311G(d,p) split valence double zeta basis set. The bending of Si-O-Si bridging is often explained by three contributes, coulombic repulsion between two SiO<sub>4</sub> tetrahedra, lone pair (or valence shell electron pair repulsion rule) of bridging oxygen, and the d-p  $\pi$ -bonding model. The contributes coulombic repulsion between second-nearest to energy surface seems to be important. Because the bending configuration cannot be reproduced in some combinations of model chemistry and basis set (Tsuneyuki, 1996). The contribute of lone pair electrons of bridging oxygen decrease the bridging angle. Oxygen atom has 6 valence electrons. The electrons make sp<sup>3</sup> hybrid orbital and tetrahedral configuration of bonding orbital and lone pair because of coulombic repulsion between orbitals. The stabilization by bending is represented in figure 4.4. The sum of the energy of valence orbital decrease with bending. The orbital energy of lone pair split and the energy of the one of the lone pair does not change because of the orthogonal decomposing of lone-pair electrons unlike with bonding orbitals. However the changes in orbital energy of valence orbital of oxygen atom shows the tendency of equalization of each orbital. Consequently the effect of lone pair potentially bend the Si-O-Si bridging. The d-p  $\pi$ -bonding between Si and O atoms is considered to act an important role in Si-O-Si bridging (Cruickshank, 1961). Newton and Gibbs (1980) calculated the contributes of 3d-orbital to Si-O bonding from the

results of MO calculation with Hartree-Fock method and STO-3G basis by Mulliken population analysis (Mulliken, 1955). In Newton and Gibbs (1980), the total overlap populations in Si-O bonding is 0.832 to 0.862. The population of  $\sigma$ -bonding between sp hybrid orbital of Si and O is 0.556. Population of  $\sigma$ -bonding and  $\pi$ -bonding which 3d-orbital involves are 0.113 and 0.163, respectively. The results of population analysis in our calculation are shown in Figure 4.5 and Table 4.3. Figure 4.5 shows the ratio of d character from Si in Si-O  $\sigma$ -bonding. The contribution of d character to  $\sigma$ -bonding is only about 2% whereas the population analysis by Newton and Gibbs (1980) shows several tens of percent. The occupancy of valence orbitals analyzed by natural atomic orbital analysis are shown in Table 4.3. The ratio of occupancy of d-orbital to s- and p-orbital is about 1%. The effect of d-p  $\pi$ -bonding seems to be negligible in Si-O-Si bridging. Consequently, the bending of Si-O-Si bridging can be explained by the balance of Coulombic repulsion between tetrahedra and lone pair electrons of bridging oxygen atom.

The relationship between Si-O-Si angle and Si-O bond length or strength have been discussed by Newton and Gibbs (1981), Navrotsky et al. (1985), Geisinger et al. (1985), etc.. The general result of these works is Si-O bond lengthen with bending Si-O-Si angle. This phenomenon is also reported by experiments (Gibbs et al., 1977). This study

shows same tendency in energy surface map (Figure 4.2 and 4.3). The mechanism of Si-O bond lengthening by bending of Si-O-Si angle can be explained by orbital energy of Si-O bonding and overlap weighted bond index. The energy of Si-O bonding orbital increase with bending Si-O-Si angle (Figure 4.4). This means that the Si-O bonding stabilize when the Si-O-Si angle is 180°. The ideal orbital energy of sp hybrid orbital should be lower than that of sp<sup>3</sup> hybrid orbital because of energy difference between s- and p-orbital, qualitatively. The changes in orbital energy during bending of Si-O-Si angle is the result of increase of ratio of p character in sp<sup>λ</sup> hybrid orbital in Si-O bonding in contribute of bridging oxygen. The weakening of Si-O bonding with bending Si-O-Si angle can be explained by hybridization from the viewpoint of energy of bonding orbital. Another view point is overlap-integration weighted bond index. The overlap weighted bond order is considered to be simply related with bond strength and bonding energy, especially in the case of homonuclear diatomic molecule. However the calculated overlap weighted bond order has locally minimum at Si-O-Si angle of 140 to 145 degree whereas the orbital energy of Si-O bonding simply decrease with bending Si-O-Si angle (Figure 4.4). The locally minimum of overlap weighted bond represents the transition of the type of hybridization of sp<sup>λ</sup> orbital of bridging oxygen. The changes in the point charge of atom (Figure. 4.5) seems to support the weakening of Si-O

bonding with bending Si-O-Si angle. The point charge at Si and O atom increase with increasing Si-O-Si angle. This means the coulombic interaction increase with increasing Si-O-Si angle. Consequently the Si-O bonding strengthen with increasing Si-O-Si angle because of stabilization of Si-O bonding orbital with decreasing the hybridization index  $\lambda$  in  $sp^\lambda$  orbital of bridging oxygen and increase of coulombic interaction between Si and bridging oxygen atom.

I hypothesize the variation of Si-O-Si angle strongly affect to the transportation coefficient of silicates. The decrease of Si-O-Si angle and viscosity of acidic silicate liquid by escalation of pressure is well known experimental fact (See Chapter 2.). The softening phenomena of silicate liquids can be explained by weakening of Si-O bonding by bending of Si-O-Si angle, from the view point of quantum chemical study. The Eyring's viscosity equation is written as follows,

$$\eta = \frac{hN_A}{V_m} e^{\Delta E/\beta} \quad (3)$$

where  $h$  is Plank's constant,  $N_A$  is Avogadro's number,  $V_m$  is the volume of molecule and  $\Delta E$  is the activation energy. Then we postulate that the molecule in Eyring's viscosity model of liquid is  $SiO_4$  tetrahedra. The Si-O bond strength cannot be used directly for the activation energy because the activation energy expresses not only the exchanging of one bond but also the sliding of bulk liquid. However the change of

bonding energy can affect to the activation energy because the activation energy is the energy barrier between two states and the height of energy barrier is affected by the sum of interatomic energy that express the express the sum of total energy of each state in thermal processes.

### 4.3 Conclusion

I here showed the results and discussion of molecular orbital calculations of pyrosilic acid molecule. I found the equilibrium geometries for two pyrosilic acid molecules ( $C_{2v}$  and  $60^\circ$  torsion) using Møller-Plesset perturbation theory and with 6-311G(d,p) split valence double zeta basis set. The bending of Si-O-Si angle in equilibrium geometries can be explained by explained by the balance of Coulombic repulsion between tetrahedra and lone pair electrons of bridging oxygen atom without concerning the contribution of d-p  $\pi$ -bonding. I calculated the energy surface with varying Si-O<sub>br</sub> length and Si-O-Si angle and found the relationship between Si-O<sub>br</sub> length and bridging angle. The Si-O bonding strengthen with increasing Si-O-Si angle because of stabilization in energy of Si-O bonding orbital with decreasing the hybridization index  $\lambda$  in  $sp^\lambda$  orbital of bridging oxygen and increase of coulombic interaction between Si and bridging oxygen atom.

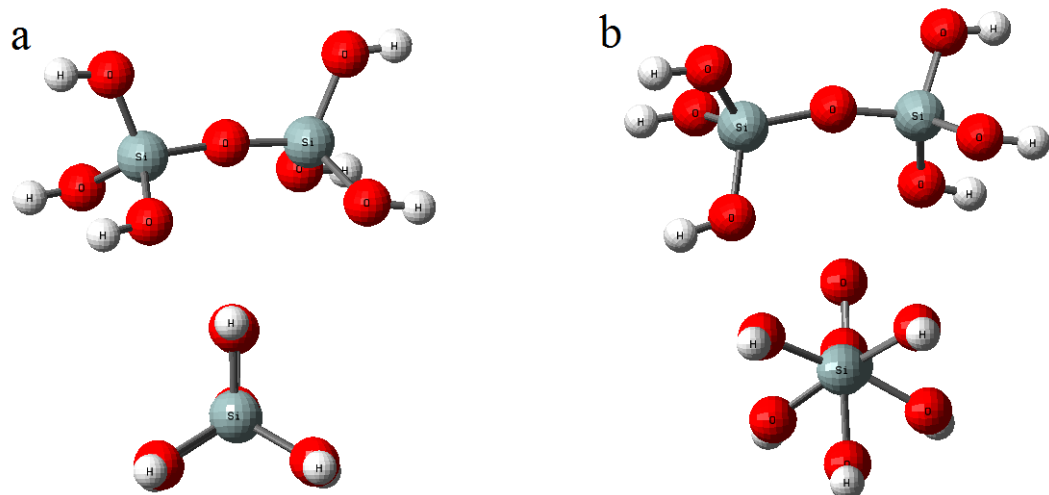


Figure 4.1. Calculated equilibrium geometries of pyrosilic acid molecule. (a)  $C_{2v}$  symmetry. (b) Each tetrahedra mutually twisted  $60^\circ$  degree ( $60^\circ$  torsion).

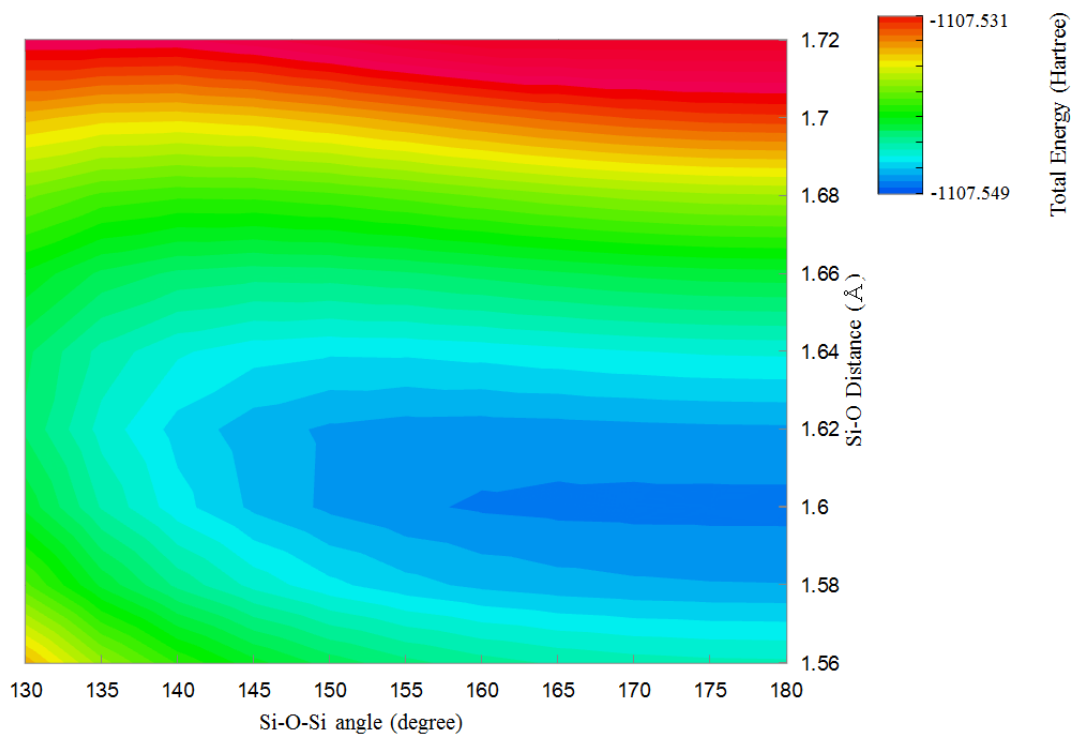


Figure 4.2. The contour map of energy surface of pyrosilicic acid molecule ( $C_{2v}$ ) with varying  $Si-O_{br}$  and Si-O-Si angle.

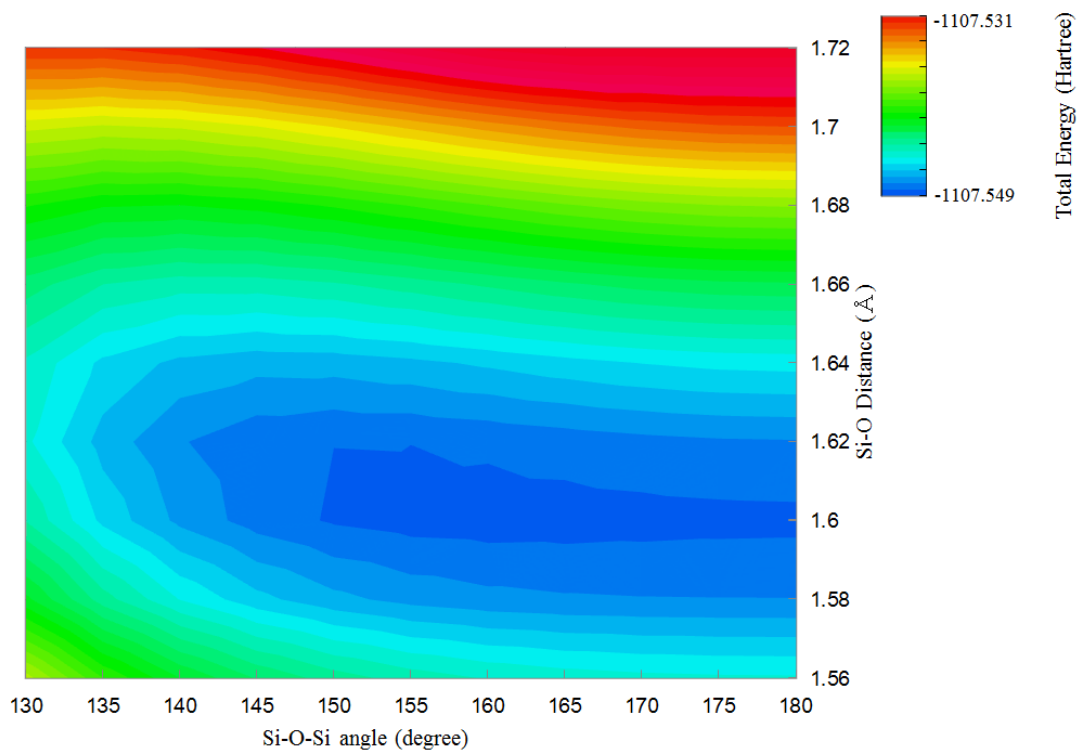


Figure 4.3. The contour map of energy surface of pyrosilic acid molecule ( $60^\circ$  torsion) with varying  $\text{Si-O}_{\text{br}}$  and Si-O-Si angle.

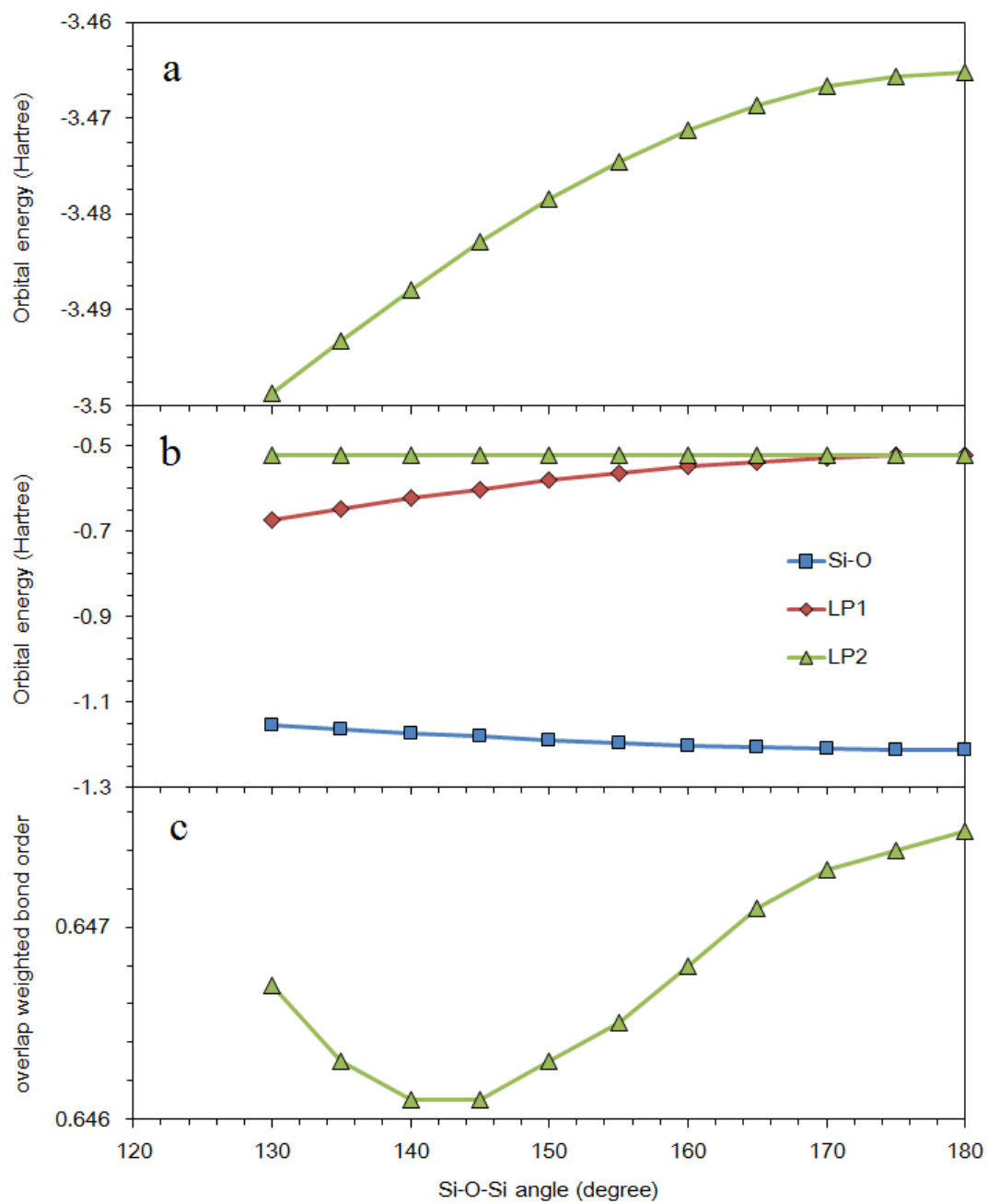


Figure 4.4. The plots of (a) sum of energy of the valence orbitals of bridging oxygen atom, (b) orbital energy of each valence orbitals of bridging oxygen atom and (c) overlap weighted bond order of Si-O<sub>br</sub> bonding with varying Si-O-Si angle in the case of 60° torsion.

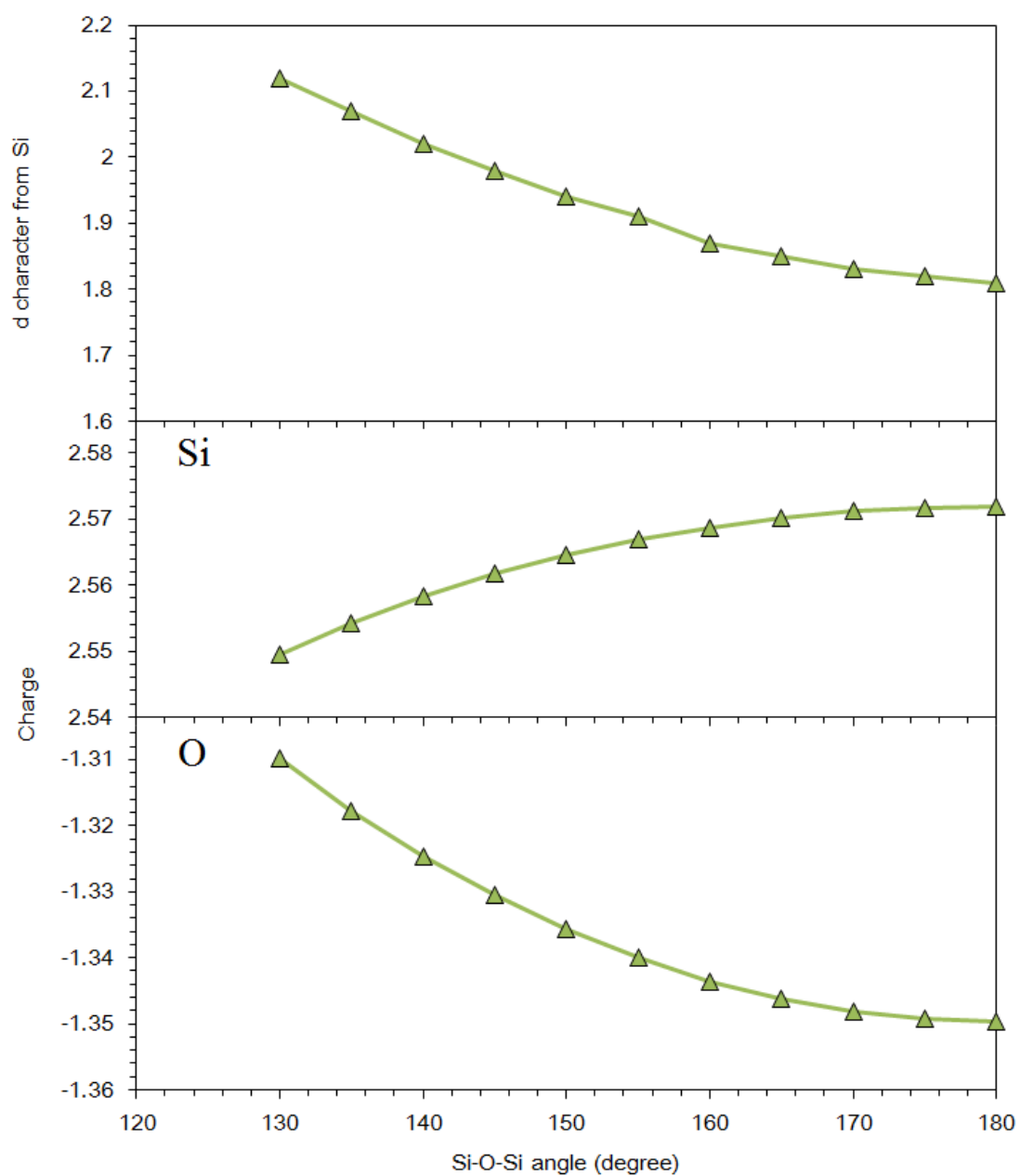


Figure 4.5. The plots of d character in Si-O  $\sigma$ -bonding, and point charge of Si and bridging oxygen atoms with varying Si-O-Si angle in the case of  $60^\circ$  torsion.

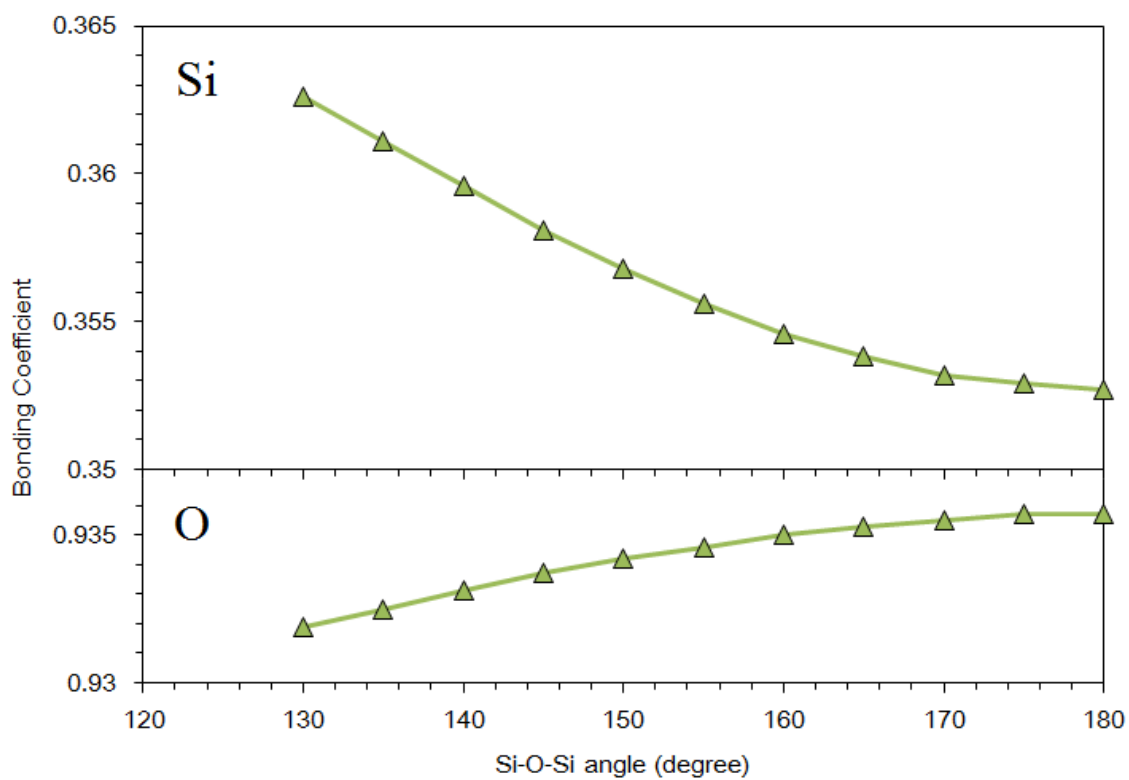


Figure 4.6. The plots of bonding coefficients Si and O atoms for Si-O<sub>br</sub>  $\sigma$ -bonding with varying Si-O-Si angle in the case of 60° torsion

	Exp.	HF		MP2		B3LYP		PBE	
Si-O	1.634	1.621	-0.013	1.642	0.008	1.640	0.006	1.635	0.001
Si-H	1.486	1.476	-0.010	1.476	-0.010	1.485	-0.001	1.488	0.002
Si-O-Si	144.1	180.0	35.9	156.5	12.0	179.2	35.1	169.7	25.63
O-Si-H	109.9.	109.9	0.0	110.4	0.5	109.9	0.0	110.1	0.2
H-Si-H	109.1	109.0	-0.1	109.0	-0.1	109.0	-0.1	109.0	-0.1

Table 4.1. The optimized parameters and difference from experimental value in angstrom and degree of disiloxane molecule,  $(\text{SiH}_3)_2\text{O}$  by MO calculation using various model chemistry. The experimental value is taken from Almenningen et al. [17].

	C <sub>2v</sub>	60° torsion
Si-O <sub>br</sub>	1.601171	1.604154
Si-O <sub>nbr</sub>	1.648782	1.648563
O-H	0.954669	0.954561
Si-O-Si	172.006	159.647
Si-O-H	117.705	117.857
Total Energy (Hartree)	-1107.5476706	-1107.5482842

Table 4.2. The optimized parameters in angstrom and degree of pyrosilicicacid molecule, H<sub>6</sub>Si<sub>2</sub>O<sub>7</sub> by MO calculation using MP2 level and 6-311G(d,p) basis set.

	130°	155°	180°
3s	0.44388	0.43775	0.43546
3px + 3py + 3pz	0.92376	0.91504	0.91303
3dxy + 3dyz + 3dzx + 3dx <sup>2</sup> y <sup>2</sup> + 3d <sup>2</sup>	0.05959	0.05834	0.05808

Table 4.3. The occupancy of natural atomic orbital of Si in various Si-O-Si angle in pyrosilic acid (60° torsion).

## **5. Na<sub>2</sub>O-nSiO<sub>2</sub> liquid at pressure**

Several mechanisms have been proposed by various researchers in order to explain the softening of silicate melts at high pressure. One hypothesis is that weakening of the Si-O bond is caused by bending of the Si-O-Si angle from the ideal angle and the distortion of the SiO<sub>4</sub> network during compression. The other hypothesis is that diffusion of oxygen is likely to occur via minor highly coordinated Si species which appear gradually with increasing pressure (see Chapter 2). However, those hypotheses have not been verified by spectroscopic methods because they investigate inter-atomic lengths of near neighbor atoms or amounts of coordination species.

In order to obtain more precise information on structure of silicate melt under high pressure, knowledge of network conformation are needed as well as inter-atomic distances. In this study, the structure and properties of Na<sub>2</sub>O·nSiO<sub>2</sub> melt under high pressure are investigated using molecular dynamics (MD) simulation and electrical conductivity measurement in order to understand the relationship between the structure and properties of silicate melts.

### **5.2 Computational method**

Molecular dynamics simulations of  $\text{Na}_2\text{O} \cdot n\text{SiO}_2$  liquids were performed using the MXDORTO code. The simulated pressure range is from 0.1 MPa to 12 GPa with NPT ensembles ( $N = 8000$ ,  $T = 1873$  K) and the potential model which well reproduces structures various silicate crystals (Noritake et al. 2012). We imposed periodic boundary conditions in all directions. The Ewald summations were applied for evaluating the long-ranged Coulombic interactions. The pressure and temperature were kept constant at a given value through a scaling procedure. All the atoms were moved by application of the Verlet algorithm under a time interval of 0.5 fs.

The function of inter-atomic potential model used in this work is as follows .

$$U_{ij} = \frac{1}{4\pi\epsilon_0} \frac{Z_i Z_j e^2}{r_{ij}} + f_0(b_i + b_j) \exp\left(\frac{a_i + a_j - r_{ij}}{b_i + b_j}\right) + \frac{c_i c_j}{r_{ij}^6} + D_{1ij} \exp(-\beta_{1ij} r_{ij}) + D_{2ij} \exp(-\beta_{2ij} r_{ij}) \quad (5.1)$$

This model explicitly includes Coulomb potential as the 1st term, short-range repulsion as the 2nd term, van der Waals force as the 3rd term and radial part of covalent effect as the 4th and 5th terms. Adding to two-body term, the three body term is also used.

$$U_{ijk} = -f[\cos\{2(\theta_{kij} - \theta_0)\} - 1] \sqrt{k_{ij} k_{ik}} \quad (5.2)$$

$$k_{ij} = \frac{1}{\exp[g_r(r_{ij} - r_m)] - 1} \quad (5.3)$$

Starting with a randomly generated structure and randomly generated velocities of

atom, I firstly calculate through 2.0 ns (4,000,000 steps) as relaxation at 0.1 MPa. Then the static and dynamic properties are obtained from 500,000 steps production run. Starting from relaxed structure, the relaxation and production runs for 1 GPa higher pressure are performed.

## **5.3 Result and Discussion**

### **Transport coefficients**

Figure 5.1 shows the pressure dependence of diffusion coefficients. The diffusion coefficients of Na atom decrease with increasing pressure in every compositions. The diffusion coefficients of network forming elements shows complex behavior as various past study reports by measurement of shear viscosity and direct measurement of diffusion coefficients (see chapter 2). The diffusion coefficients simply decrease with increasing pressure in  $\text{Na}_2\text{O}\cdot\text{SiO}_2$  liquid. However, the inclination become shallower with increasing pressure. The diffusion coefficients of network forming elements in  $\text{Na}_2\text{O}\cdot 2\text{SiO}_2$  shows two types of pressure dependence. The diffusion coefficients decrease with increasing pressure up to 3 GPa, then increasing with increasing pressure above 3GPa. The diffusion coefficients increasing with increasing pressure in acidic liquids. The decrease around 10 GPa is similar to the result of Diefenbacher et al.

(1998). However there are two types of power laws between self-diffusion coefficients of network forming elements and exchanging rate of Si-O bonding. Figure 5.3 shows logarithm of self-diffusivity of oxygen versus logarithm of exchanging rate of Si-O bonding. The relation between bond exchanging rate  $R_{exc}$  and self-diffusivity of network forming elements  $D_{nwf}$  of basic liquid at lower pressure is written as follows,

$$D_{nwf} = aR_{exc} + c \quad (5.4)$$

where  $a$  and  $c$  is constant. Meanwhile the relation of acidic liquid at higher pressure is written as follows.

$$D_{nwf} = aR_{exc}^{\frac{1}{4}} + c \quad (5.5)$$

These anomalous pressure dependence might be caused by distortion of corner shared network of  $\text{SiO}_4$ . One obvious structural distortion is a decrease in the Si-O-Si angle (Figure 5.4a). The Si-O-Si angle has a stable angle by the balance of Coulombic repulsion between tetrahedra and lone pair electrons of bridging oxygen atom (see chapter 4). The bending of Si-O-Si angle weaken the Si-O bonding by destabilization of Si-O bonding orbital by increase the hybridization of p-orbital. The bending activate diffusion of oxygen atoms and  $\text{SiO}_4$  tetrahedra because the energetic destabilization of Si-O bonding decrease the energy barrier of exchanging of  $\text{SiO}_4$  network. The distortion of  $\text{SiO}_4$  tetrahedra also affect the bond strength. In a regular tetrahedron, the O-Si-O

angles are  $109.47^\circ$ . However the average O-Si-O angle decreases from  $109.47^\circ$  with increasing pressure (Figure 5.4b). Oxygen atoms is unstabilized when the tetrahedron distorts because of repulsion between oxygen. Consequently, the Si-O bond weakens with elevating pressure. The decrease of the O-Si-O angles is due to deformation from the regular tetrahedron to the distorted one. The distortion factor of polyhedra,  $\alpha$  is written as follows,

$$\alpha = \left\langle \frac{1}{n} \sum_{i=1}^n [r_a - |x_0 - x_i|]^2 \right\rangle \quad (5.6)$$

$$r_a = \frac{1}{n} \sum_{i=1}^n |x_0 - x_i| \quad (5.7)$$

$$x_0 = \frac{1}{n} \sum_{i=1}^n x_i \quad (5.8)$$

where  $n$  is coordination number of the atom at center and  $x_i$  is the position of coordinating atom. The  $\text{SiO}_4$  tetrahedra actually distorts by using these criteria (Figure 5.5). However the distortion factor of  $\text{Na}_2\text{O} \cdot \text{SiO}_2$  liquid does not change in elevating pressure. One possible deformation is that Si and 3 oxygen atoms are located in one plane and one oxygen atom is located out of the plane (deformation in  $\text{C}_{3v}$  symmetry). The other is that the silicon atom and 4 oxygen atoms are located into one plane. If the former deformation occurs under high pressure, the diffusion process below is conceivable. A silicon atom and 3 oxygen atoms are located on one plane are

disconnected from bridged  $\text{SiO}_4$  as  $\text{SiO}_3$ , and then  $\text{SiO}_3$  is connected to the other non-bridging oxygen atom (see Fig. 17 of Noritake et al. 2012). Changes in the distribution of ring size also possibly affect the transportation coefficients of liquid (Figure 5.6). The liquids mechanically softens by decrease of 4-membered rings and with increasing pressure, because the structure of the network is likely to deform by formation of a more flexible structure through the decreasing of 4-membered rings at pressure.

The difference of pressure dependence of transportation coefficient is caused by transition from simple liquid to networked liquid with increasing pressure or  $\text{SiO}_2$  content. When the network forming element move certain distance  $r$  by each bond exchanging event, the relation between self-diffusivity  $D$  and bond exchanging rate  $R_{exc}$  is written as follows,

$$D = \frac{C_1}{6} r^2 R_{exc} + C_2 \quad (5.9)$$

where  $C_1$  and  $C_2$  are coefficient those represent probability of diffusion direction and thermal component, respectively. The silicate liquids act like simple liquid when the exchanging rate of Si-O bonding has linear relation with diffusion coefficient of network forming elements. When the  $\text{SiO}_4$  network entangles, the probability of stabilization of diffusing group at site moved. When the probability of success to diffuse

is 1/4, equation 5.9 become as follows.

$$D = \frac{C_1}{6} r^2 R_{exc}^{\frac{1}{4}} + C_2 \quad (5.10)$$

Consequently, the change in exponent represents the transition from simple liquid to networked liquid. The changes in distortion factor along pressure represent the difference between simple liquid and networked liquid (Figure 5.5). The distortion factor of  $\text{Na}_2\text{O} \cdot \text{SiO}_2$  liquid does not change with increasing pressure whereas the factors of other acidic liquids increase with increasing pressure. The networked of corner shared  $\text{SiO}_4$  tetrahedra in acidic liquid act as a framework of liquid and controls elastic properties and viscosities. The distortion of network and tetrahedra only occurs and acts as the cause of softening in entangled networked, meanwhile the both tetrahedra and polyhedra of modifiers controls the elasticity and viscosities.

### **Densification Mechanism**

Figure 5.7 gives a compression curvature of sodium silicate liquids. The plots of  $V/V_0$  along basicity are shown in figure 5.8. The compressibility of liquids does not show simple dependence on composition and pressure. Bulk moduli of each liquids are displayed in figure 5.9. The jumps in moduli are confirmed in figure 5.9. Each continuous pressure regions seem to represent the change of densification mechanisms.

T1 region in figure 5.9 is the region where the relation between exchanging rate of Si-O bonding and self-diffusivity of network former is linear. The main mechanism of densification of simple liquid-like silicate liquid is thought to be increase of coordination number. The coordination number of Si remains constant, however the coordination number of Na increases with increasing pressure (Figure 5.10). The liquids densify via increasing coordination number of Na in the pressure-composition region where the self-diffusivity of network former decrease. The silicate liquids act like simple liquid consist of Na and  $\text{SiO}_4$  group in this region. T2 region in figure 5.10 is the region where the self-diffusivity of network former is proportional to the exchanging rate of Si-O to  $1/4$ . The collapsing of network of  $\text{SiO}_4$  also contributes to the densification because there are no jumps in bulk moduli when the densification mechanism does not change. This means that network of  $\text{SiO}_4$  is forced and distorts at pressure. In the collapsing of network of  $\text{SiO}_4$ , two types of structural change exist. The one is decrease of Si-O-Si angle (Figure 5.4a), the other is decrease of 4-membered rings (Figure 5.6). These characteristics represent that the collapse of network consist of increase of degree of freedom of deformation of network via decrease of 4-membered ring, and bending of Si-O-Si angle. In this densification, the softening of silicate liquids appears. In T3 region, the 4-membered ring increase with elevating pressure. This type

of change is also confirmed in coesite transition of  $\text{SiO}_2$  crystal triggered by pressure. The similar behaviour is reported in the compression of  $\text{SiO}_2$  glass (Wakabayashi et al. 2013). These compression behaviour suggests that silicate liquids gradually changed to coesite-like network structure in T3 composition-pressure region. The densification mechanism changed from simple liquid-like, through collapse of  $\text{SiO}_4$  network to coesite-like with increasing  $\text{SiO}_2$  content and pressure. The densification will change to increase of coordination number of Si above the pressure region investigated (Meade et al. 1992).

## **Conclusions**

In this chapter, the structure-property relationship of  $\text{Na}_2\text{O} \cdot n\text{SiO}_2$  liquids at pressure via force field molecular dynamics simulations. The pressure induced softening of silicate liquids is reproduced in this simulations. Distortion of  $\text{SiO}_4$  tetrahedra and decrease of Si-O-Si angle enhance exchanging of Si-O bonding. These structural change energetically enhance the exchanging of Si-O bonding. Decrease of 4-membered rings might affect the decrease of viscosity at pressure because the decrease of 4-membered ring increase the degree of freedom of deformation. There are two types of relationship between Si-O bond exchanging rate and self-diffusivity of network formers those are

written by power law. Each relations represent the simple liquid-like and entangled liquid behaviour. In the compression, three types of densification are confirmed in this composition-pressure range investigated. The main mechanism of densification is increase of coordination number of Na like simple liquid consist of Na and  $\text{SiO}_4$  group at lower pressure and high basicity. High  $\text{SiO}_2$  content liquids densify via collapsing of  $\text{SiO}_4$  network. The collapse of network is consist of bending of Si-O-Si bridging and decrease of 4-membered rings. The acidic liquid become coesite like structure by elevation of pressure.

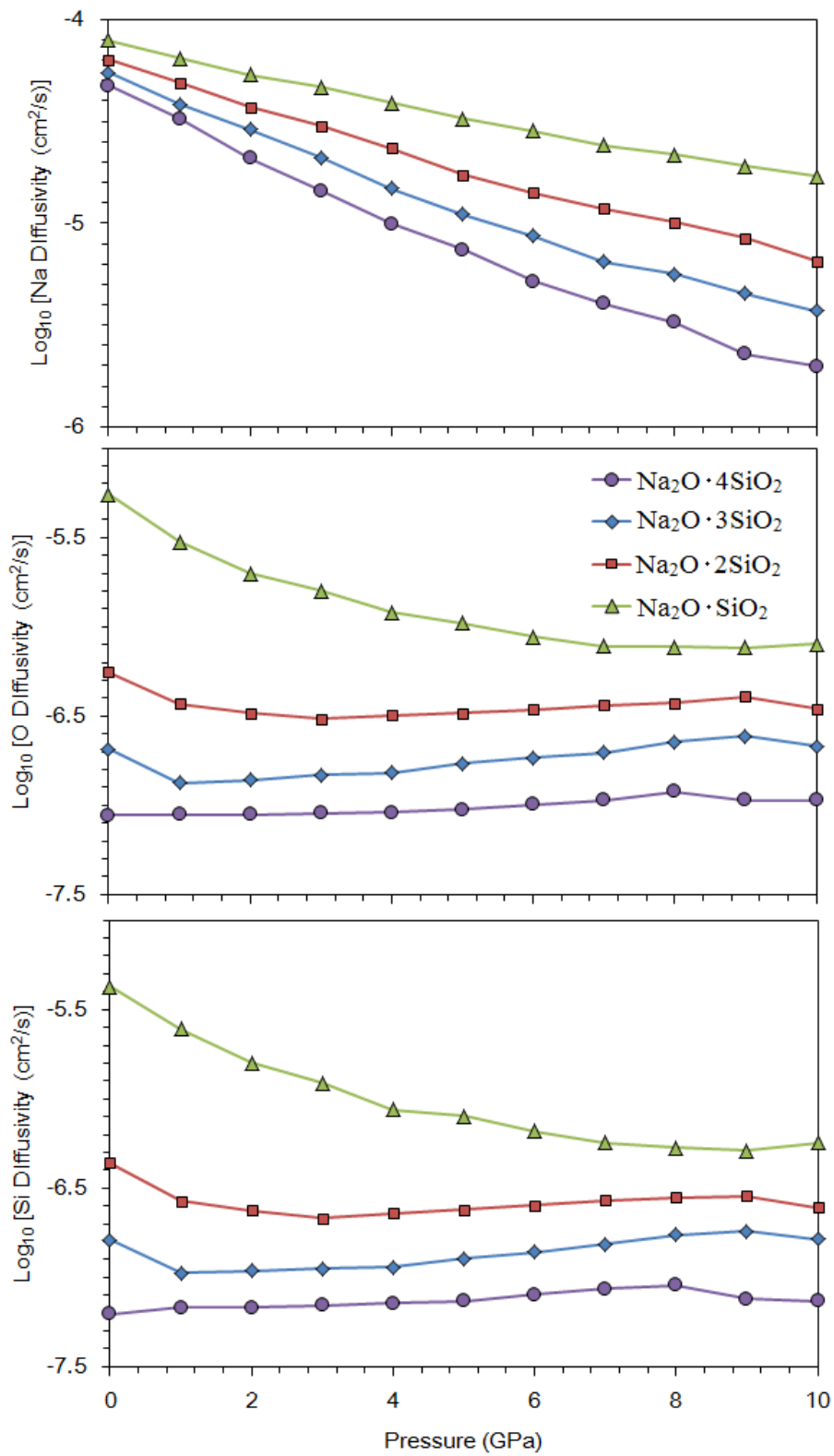


Figure 5.1. Plots of logarithm of diffusion coefficients versus pressure.

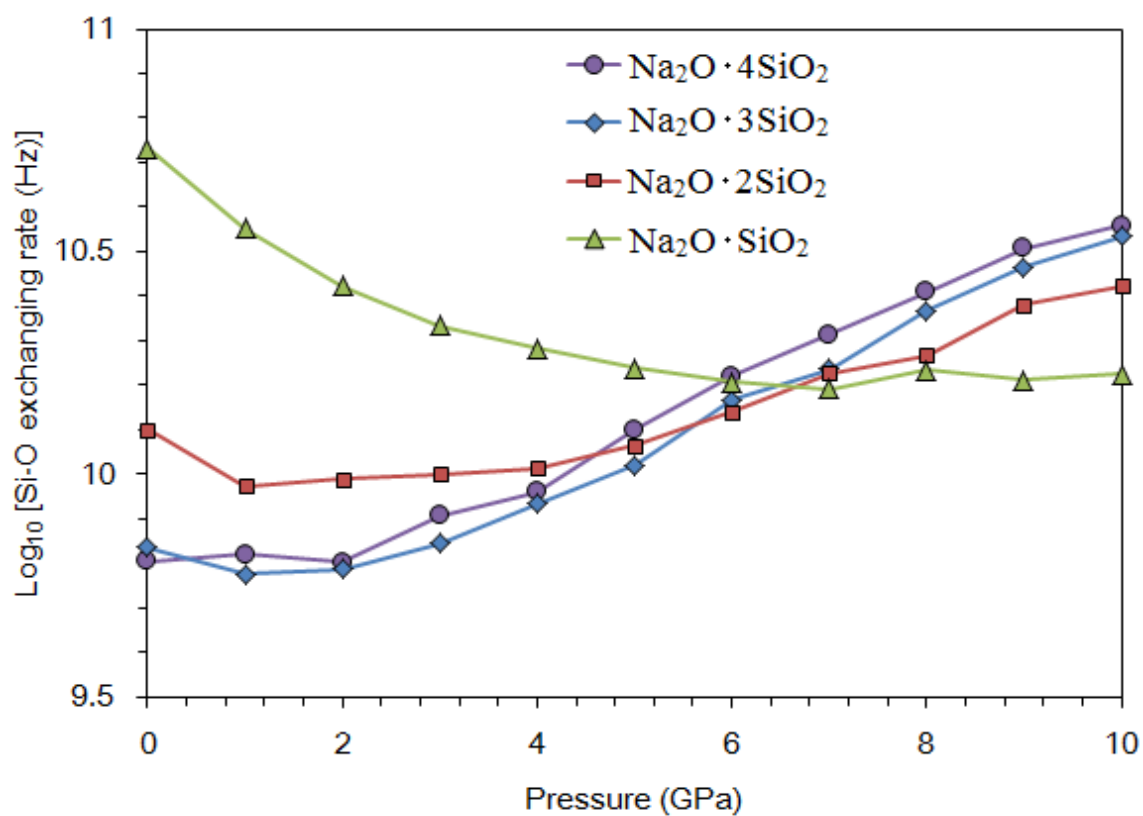


Figure 5.2. Plots of logarithm of bond exchanging rate versus pressure.

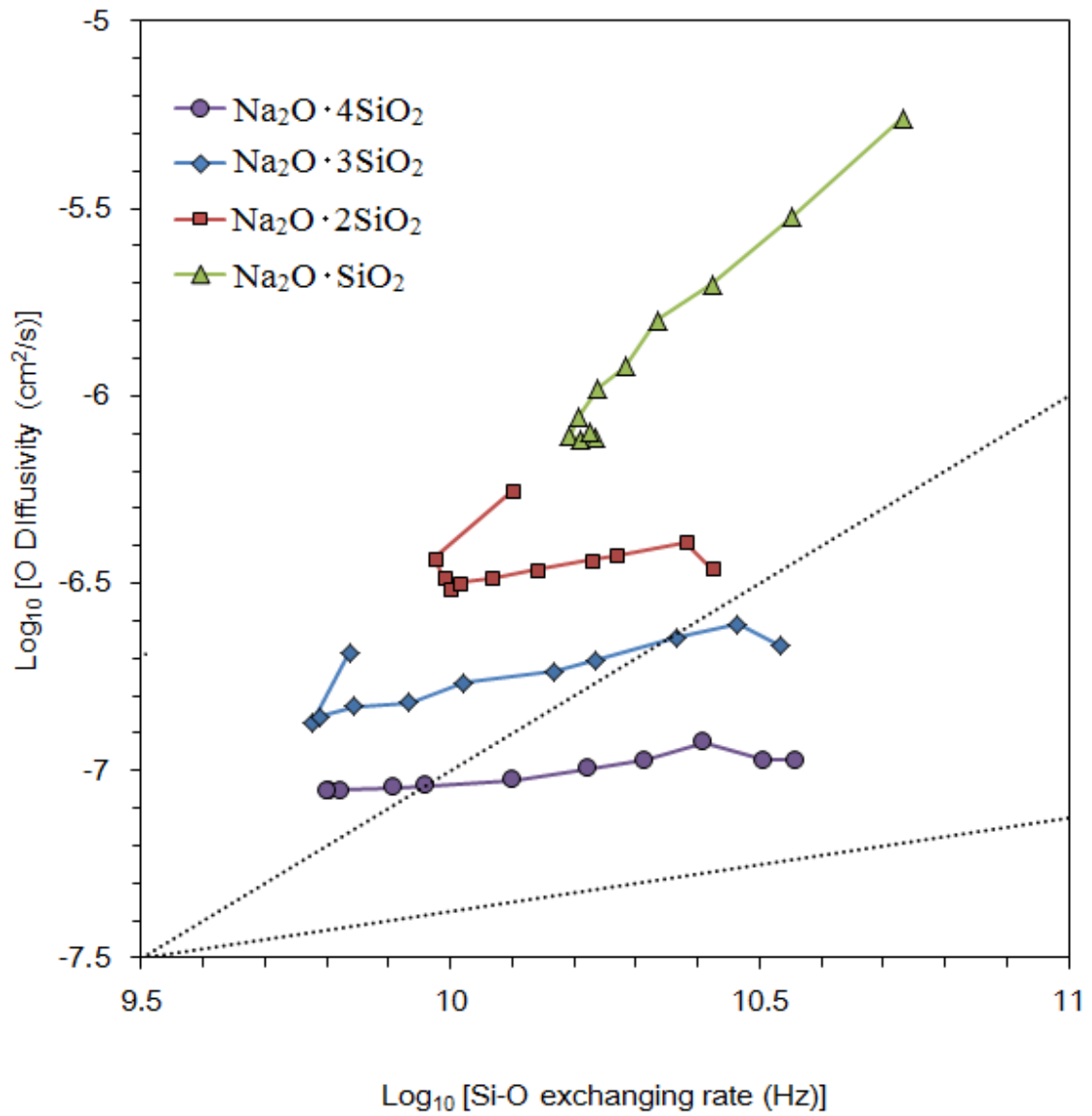


Figure 5.3. Plots of logarithm of oxygen diffusivity versus logarithm of bond exchanging rate. The dotted line represent the lines those exponent is 1 and 1/4.

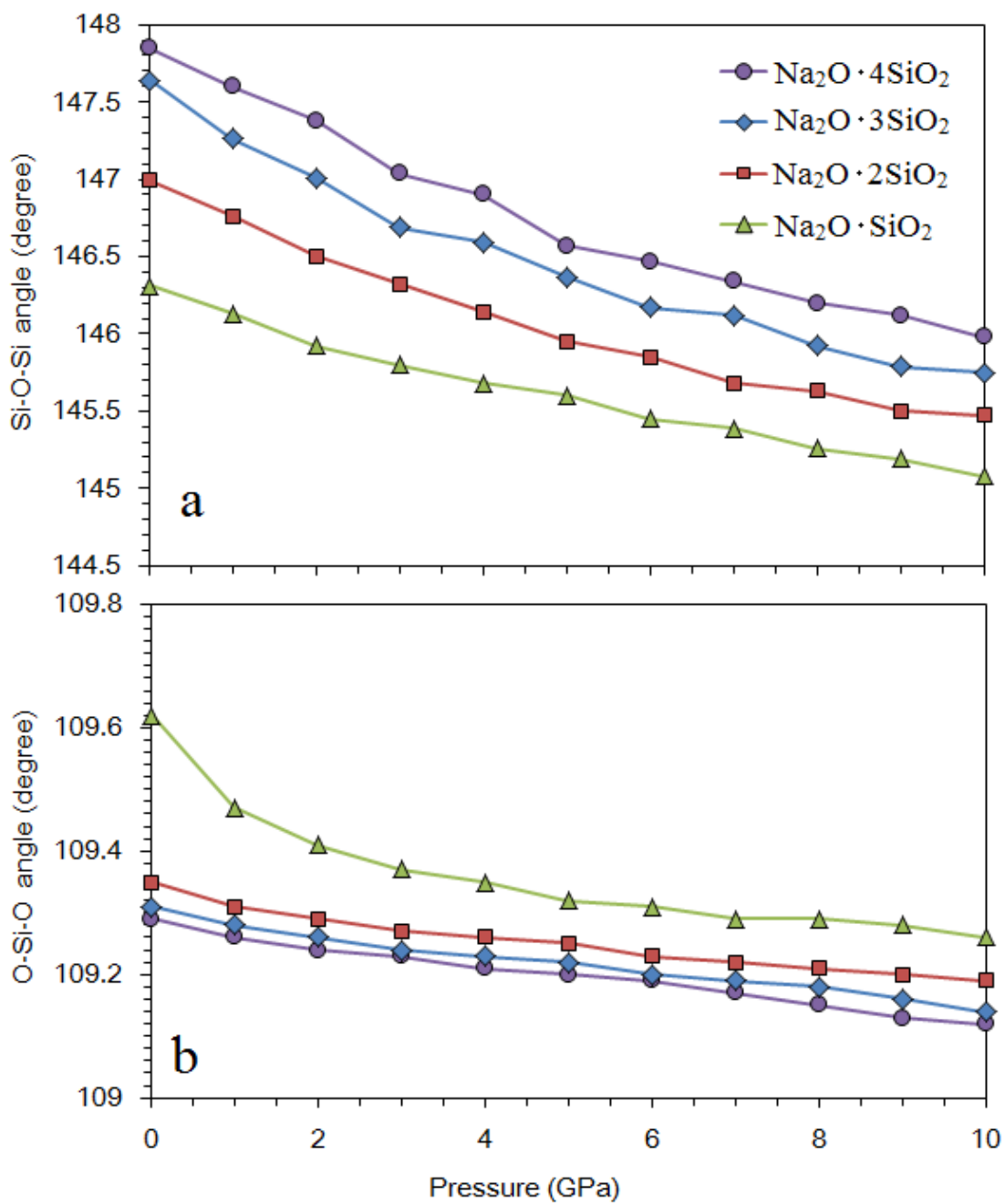


Figure 5.4. The plots of average Si-O-Si angle (a) and O-Si-O angle versus pressure.

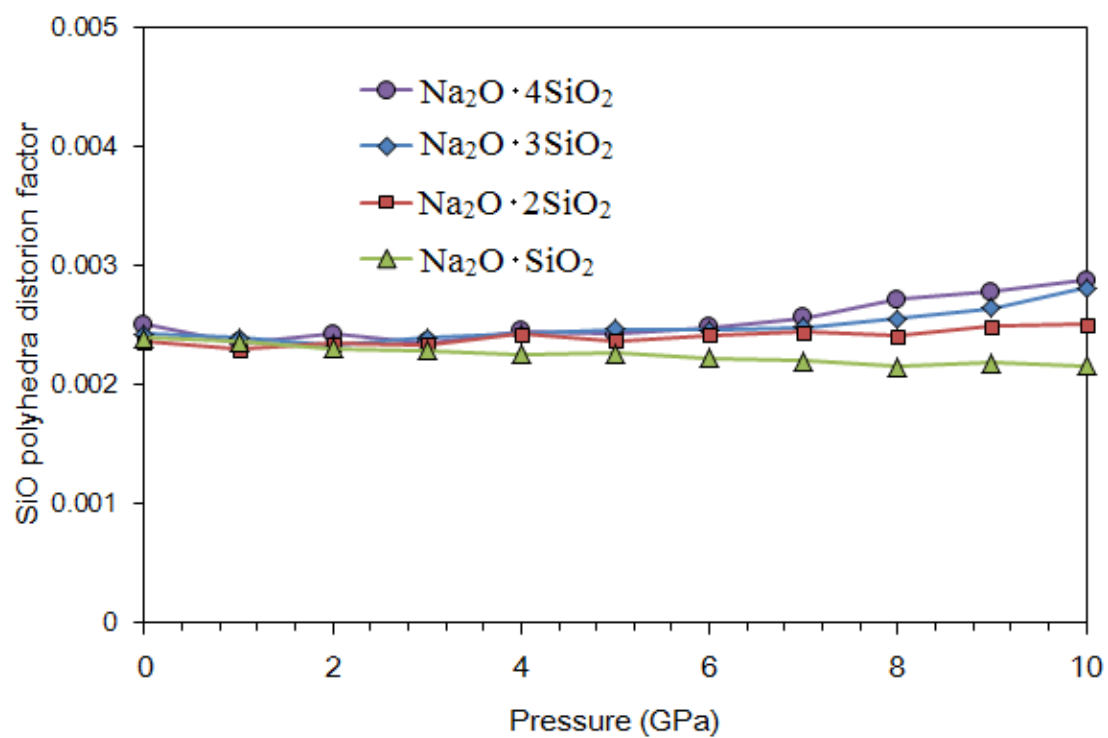


Figure 5.5. The plots of distortion factor of SiO<sub>4</sub> tetrahedra versus pressure.

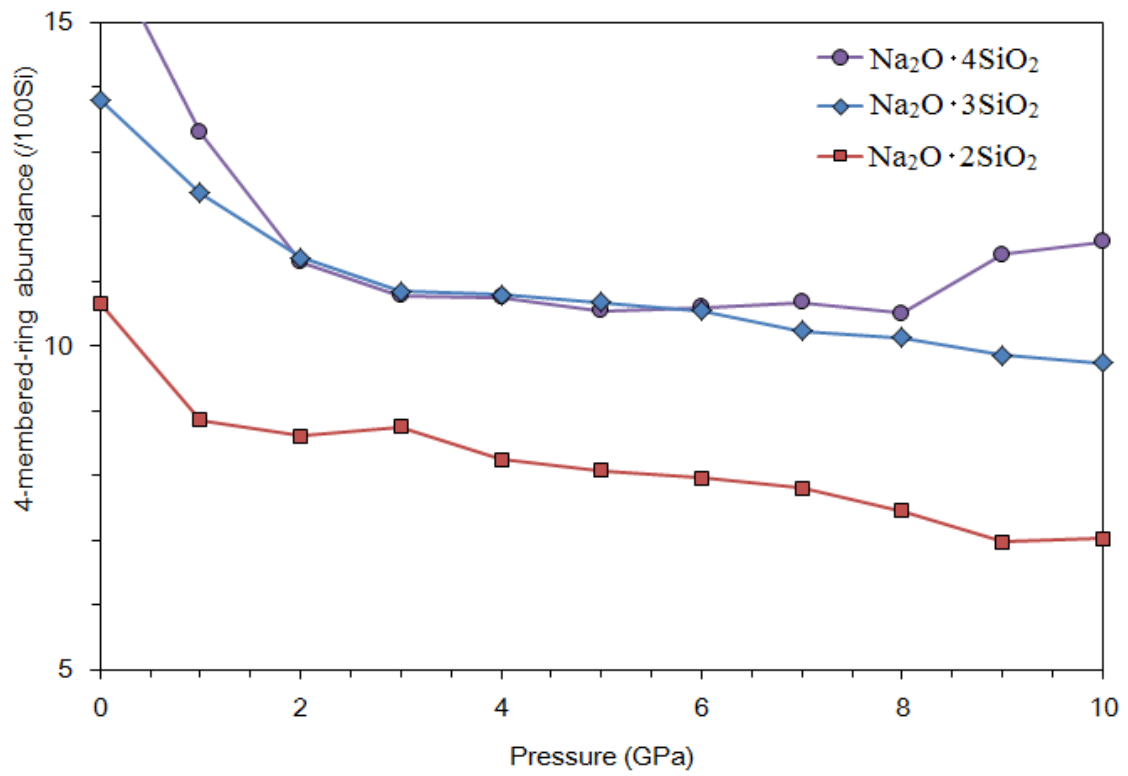


Figure 5.6. The plots of the abundance of 4-membered ring per 100 Si atom versus pressure.

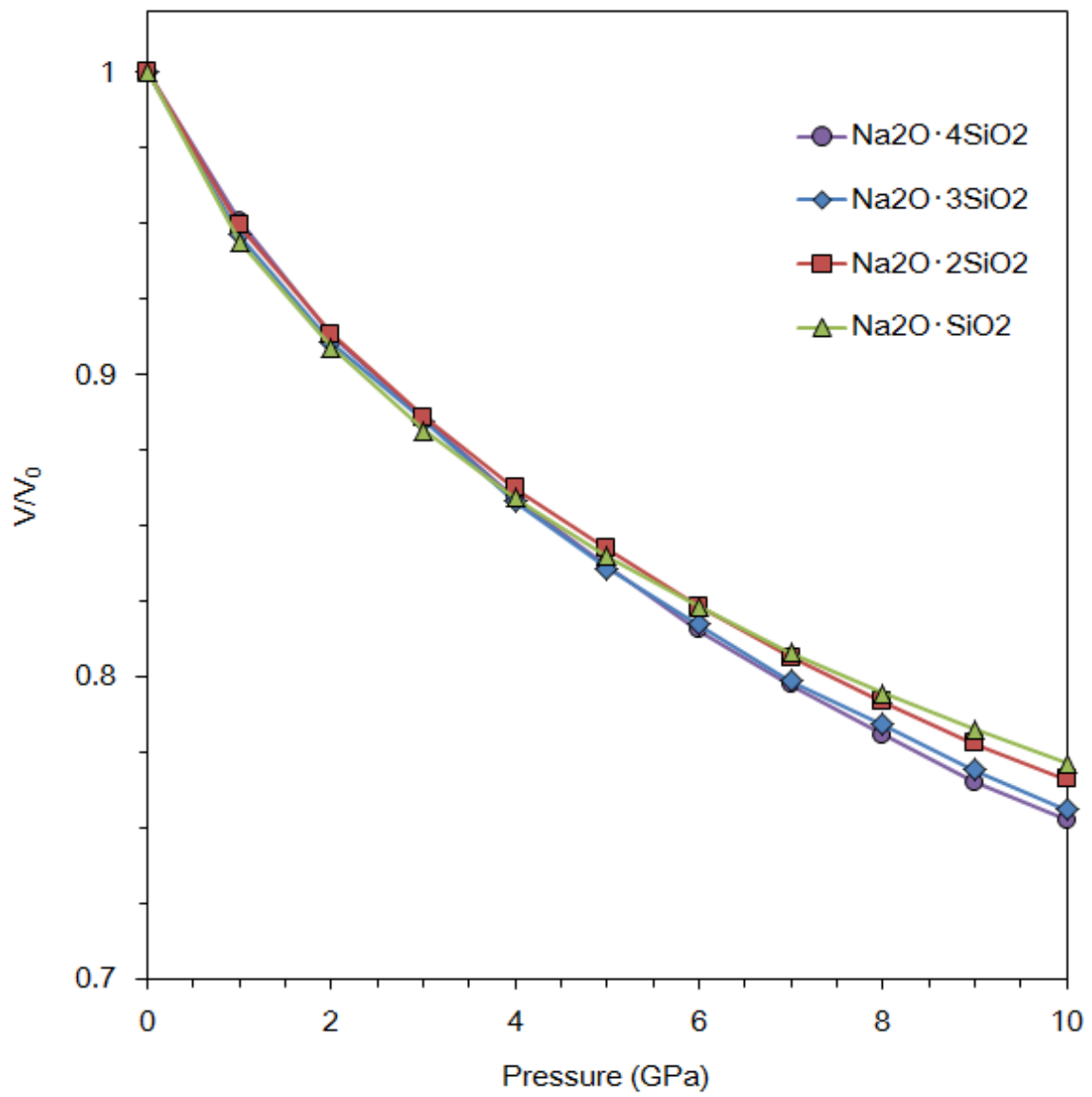


Figure 5.7. Plots of  $V/V_0$  as functions of pressure.

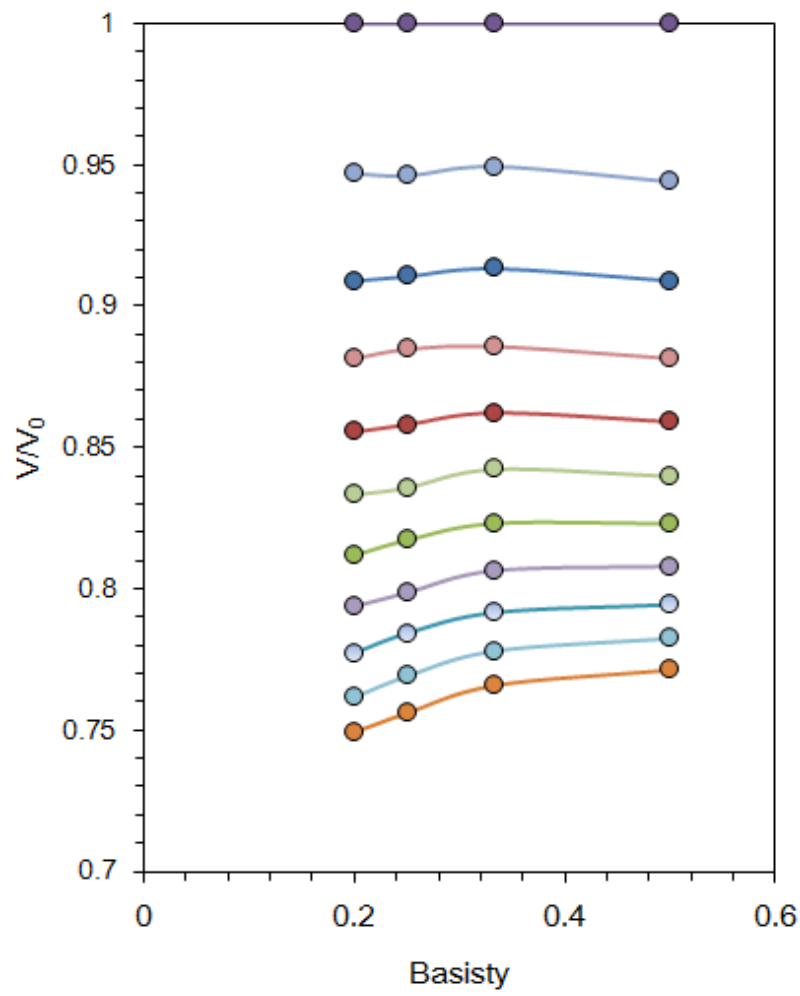


Figure 5.8. Plots of  $V/V_0$  as functions of basicity.

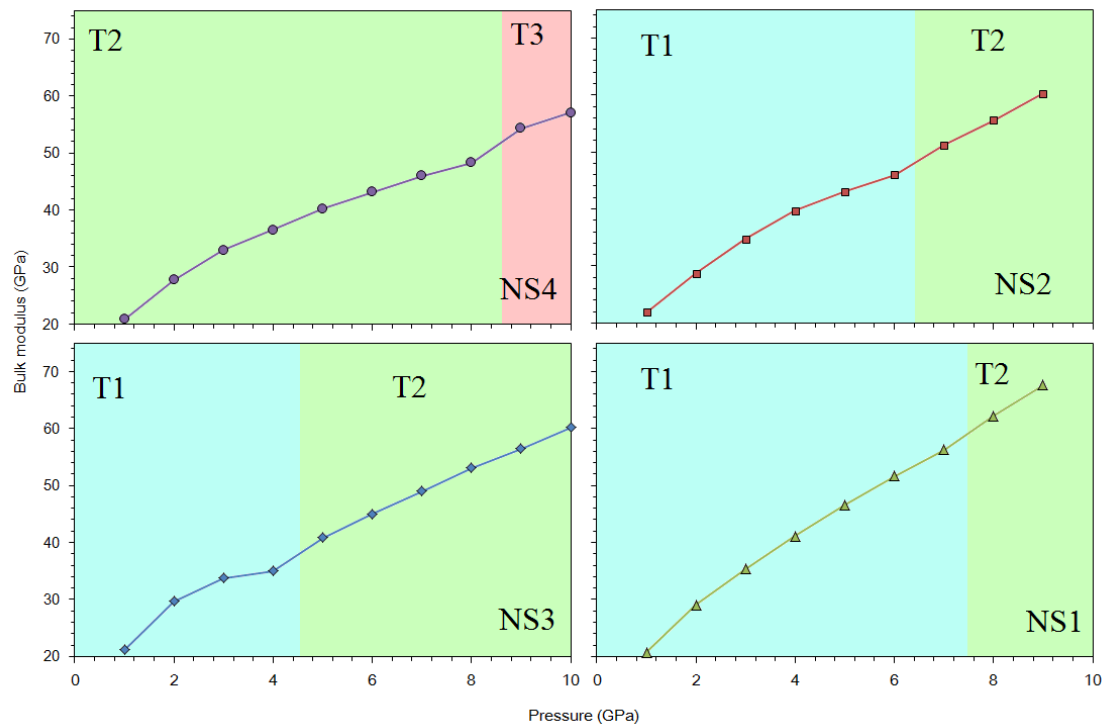


Figure 5.9. Plots of bulk modulus of various composition versus pressure NS1, NS2, NS3 and NS4 represent  $\text{Na}_2\text{O} \cdot \text{SiO}_2$ ,  $\text{Na}_2\text{O} \cdot 2\text{SiO}_2$ ,  $\text{Na}_2\text{O} \cdot 3\text{SiO}_2$  and  $\text{Na}_2\text{O} \cdot 4\text{SiO}_2$  liquids, respectively.

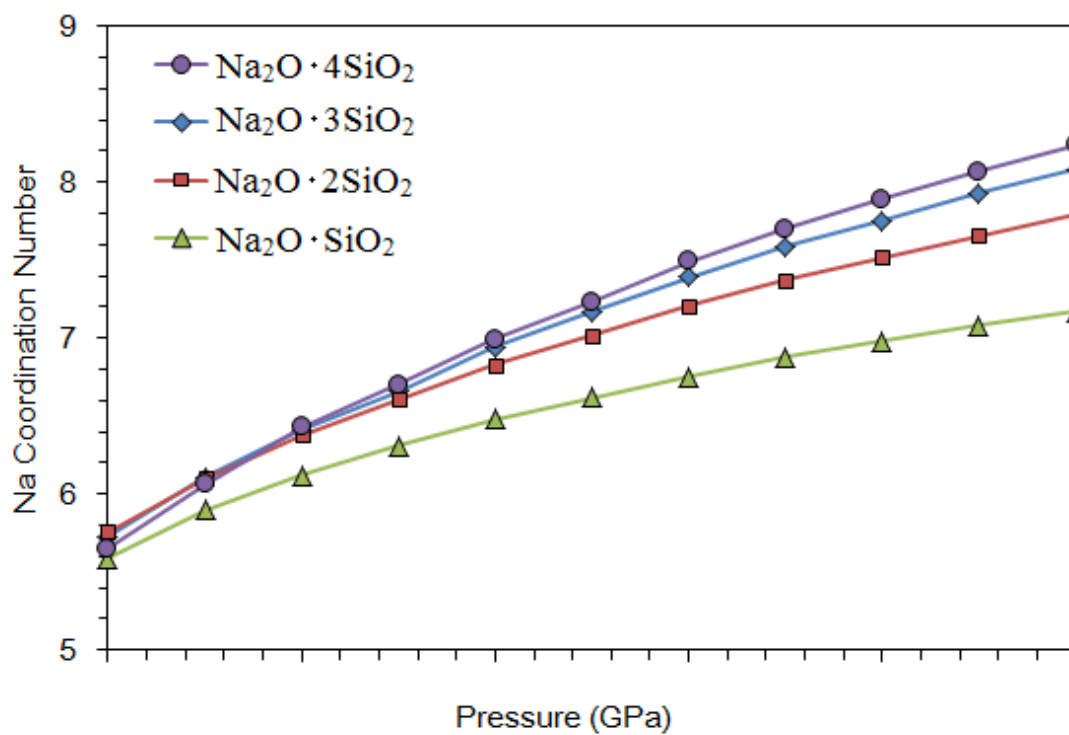


Figure 5.10. Plots of coordination number of Na versus pressure.

## **6. Silicate crystal/liquid interface**

Knowledge of viscosity and permeability of partially molten rocks is important for understanding volcanism and the thermal history of the earth. To understand the results obtained by experiments, and to estimate physical properties in extreme conditions that are difficult to reproduce in laboratory experiments, it is necessary to know the local structure and the properties of silicate crystal–liquid interfaces. In particular, knowledge of the nano-scale structure and properties of silicate crystal–liquid interfaces might be useful in estimating the properties of rocks containing a small degree of melting. Hiraga et al. (2002) reported the presence of nano-scale melt films using high-resolution electron microscopy and energy dispersive X-ray profiling in scanning transmission electron microscopy. The properties of melt in such thin regions are considered to be different from properties in a bulk melt because of the effect of crystal surfaces. For instance, the lateral self-diffusivity of water to a crystal surface is different from a bulk surface in the case of a water–brucite surface (Sakuma et al. 2003), a water–muscovite mica surface (Sakuma and Kawamura 2009), and others. The dynamic property anomalies on solid–liquid interfaces affect the properties of bulk rock, e.g., permeability (Ichikawa et al. 2001).

Molecular dynamics simulations are widely used to investigate the physical

properties and structures of crystals, liquids, gasses, and interfaces. In these simulations, we set the initial positions and velocities of all atoms, then the atoms are forced to move according to given force fields under a proper ensemble. Molecular dynamics simulations are useful methods for investigating the nano-scale structure and properties because they give us the trajectory of each atom. In this study, the structure and properties of the forsterite–MgSiO<sub>3</sub> liquid interface are investigated by application of molecular dynamics simulations. It is essential to know the structure and physical properties of forsterite–MgSiO<sub>3</sub> liquid interfaces because forsterite is the liquidus mineral of primordial magmas.

## 6.1 Computational Method

Molecular dynamics simulations were performed with the NPT ensemble at ambient pressure and various temperatures by application of the MXDORTO code (Sakuma and Kawamura 2009). The initial structure contains 21,440, 26,440, 43,440, and 63,440 atoms in which sheets of MgSiO<sub>3</sub> liquid consisting of 8,000, 15,000, 30,000, and 50,000 atoms (~4, ~7, ~16, and ~28 nm thickness, respectively) are sandwiched between the (010) surfaces of forsterite. First, we simulated the equilibrated MgSiO<sub>3</sub> liquid film in a vacuum, starting with a randomly generated structure and randomly generated velocities

of atoms through 0.5 ns (1,000,000 steps) at 1973 K, and quenched to 300 K. Second, we simulated bulk forsterite with 13,440 atoms ( $11 \times 5 \times 8$  unit cells of forsterite), starting with the given experimental crystal structure, which was obtained by an experiment (Fujino et al. 1981) and with randomly generated atom velocities, then we cut along the (010) surface. Finally, we combined forsterite sheets along the (010) surface and an  $\text{MgSiO}_3$  liquid film. We defined the z-axis perpendicularly to the (010) axis. Maintaining isobaric and isothermal conditions, we performed the relaxation up to 1.5 ns with a time step of 0.5 fs. Then, the statistical averages of the structure and physical properties were obtained from the velocities and coordinates of each atom in the simulations, through 500 ps. We confirmed that relaxation has been achieved by a plot of enthalpy versus time (Figure 6.1). The enthalpy of the system fluctuated around a constant value after 1.5 ns of relaxation (Figure 6.1a, 6.1b). The enthalpy of the system in the process of melting decreased, although 4 ns elapsed in the simulation (Figure 6.1c).

We imposed periodic boundary conditions in all directions. The Ewald summations were applied for evaluating the long-ranged Coulomb interactions. The pressure and temperature were kept constant at a given value through a scaling procedure. All the atoms were moved by application of the Verlet algorithm under a time interval of 0.5 fs.

The function of the inter-atomic potential model was the same as that used in our previous work (Noritake et al. 2012):

$$U_{ij}(r_{ij}) = \frac{1}{4\pi\epsilon_0} \frac{Z_i Z_j e^2}{r_{ij}} + f_0 (b_i + b_j) \exp\left(\frac{a_i + a_j - r_{ij}}{b_i + b_j}\right) + \frac{c_i c_j}{r_{ij}^6} + D_{1ij} \exp(-\beta_{1ij} r_{ij}) + D_{2ij} \exp(-\beta_{2ij} r_{ij}) \quad (5.1)$$

where  $U_{ij}(r_{ij})$  is the potential energy,  $\epsilon_0$  is the permittivity of a vacuum,  $Z_i$  is the effective charge of the  $i$ -th atom,  $e$  is the elementary charge,  $r_{ij}$  is the distance between the  $i$ -th and  $j$ -th atoms, and  $f_0$  is the constant  $4.1865 \text{ kJ } \text{\AA}^{-1} \text{ mol}^{-1}$ . The values  $a_i$ ,  $b_i$ , and  $c_i$  are the repulsion diameter, softness coefficient, and van der Waals coefficient of the  $i$ -th atom, respectively. The values  $D_{1ij}$ ,  $\beta_{1ij}$ ,  $D_{2ij}$ , and  $\beta_{2ij}$  are the parameters for the radial covalent bonds. The first term of this model gives the Coulomb potential, the second term gives the short-range repulsion, the third term is the van der Waals force, and the fourth and fifth terms are the radial part of the covalent bond. The three-body interactions between  $i$ ,  $j$ , and  $k$  are represented as follows:

$$U_{kij} = -f [\cos\{2(\theta_{kij} - \theta_0)\} - 1] \sqrt{k_{ij} k_{ik}} \quad (5.2)$$

$$k_{ij} = \frac{1}{\exp[g_r(r_{ij}-r_m)]-1} \quad (5.3)$$

where  $f$  is the force constant,  $\theta_{kij}$  is the angle among the atoms  $k$ ,  $i$ , and  $j$ , and  $\theta_0$ ,  $g_r$ , and  $r_m$  are parameters for adjusting the angular part of the covalent bonds. Atomic and pair parameters are given in Table 6.1. The potential parameters used in this study are the same as those used in Noritake et al. (2012) for silicon and oxygen atoms. We added new parameters for magnesium atoms empirically. We verified the potential parameters by calculating the lattice parameters and compressibility of forsterite and enstatite crystals (Table 6.2). The bulk modulus,  $K_0$ , and the pressure derivative of the bulk modulus,  $K'$ , are obtained by fitting the simulated compression results along the 3rd-order Birch–Murnaghan equation of state. The calculated lattice parameters and compressibility show good agreement with the experimental data (Fujino et al. 1981; Duffy et al. 1995; Morimoto and Koto 1969; Angel and Hugh-Jones 1994). We also simulated the bulk  $\text{MgSiO}_3$  liquid ( $N = 8000$ ) at ambient pressure to verify our inter-atomic potential model by comparing the self-diffusion coefficients of oxygen with other force fields and Car-Parrinello molecular dynamics (de Koker et al. 2009; Adjaoud et al. 2011; Lacks et al. 2007). The calculated diffusion coefficients show good agreement with other molecular dynamics studies (Figure 6.2a). Figure 6.2b shows the

calculated viscosity using the Einstein–Stokes relation with the effective radius reported by Lacks et al. (2007). The viscosity is lower than the experimental data (Bockris et al. 1955) by approximately half an order of magnitude. However, the activation enthalpy shows good agreement with the experimental data.

## **6.2 Result and Discussions**

### **4 nm liquid film: The structuralized liquid film**

Figure 6.3 shows snapshots of molecular dynamics simulations perpendicular to the *a*-axis of forsterite using the visualization software VESTA (Momma and Izumi 2011). The liquidus temperature appears to be 1873 K in Figure 6.3 because the crystal structure of the forsterite is altered. However, equilibrium is not achieved in a 4.5 ns run at 1873 K (Figure 6.1c). The liquidus temperature of the simulated system is approximately 150 K lower than expected from the phase diagram (Jung et al. 2004). Figure 6.4a shows a distribution of elements perpendicular to the (010) surface of forsterite at 1773 K. Figure 6.4b gives a distribution of Q-species of Si atoms perpendicular to the forsterite surface at 1773 K. The threshold length of Si–O bonding for calculating the Q-speciation is 0.22 nm. The altered crystal surfaces exist at  $z = 2\text{--}2.5$  nm and  $7\text{--}7.5$  nm. The abundance of Mg atoms is higher than that of Si atoms in this

region. The nesosilicate structure is disturbed, and 20%–40% of the  $\text{SiO}_4$  tetrahedra form Si–O–Si bridging in this region. In the near crystal surface, the Si-rich layer exists in the liquid domain. The Mg-rich layer exists on the inside of Si-rich layer. Figure 6.5 shows a distribution of the direction of the Si–O–Si bridging perpendicular to the forsterite surface as a square of the cosine between the z-axis and the vector Si–Si calculated as an inner product. The orientation of the Si–O–Si bridging in the sandwiched liquid film is clearly parallel to the crystal surface. Figure 6.6b gives a distribution of the two-dimensional self-diffusion coefficients of oxygen parallel to the forsterite surface, and Figure 6.6c shows the calculated viscosities determined using the Einstein–Stokes relation with the effective radius obtained by Lacks et al. (2007). The two-dimensional self-diffusion coefficients of oxygen are consistently lower than that of the bulk  $\text{MgSiO}_3$  liquid (dotted line) by an order of magnitude. The two-dimensional self-diffusion coefficients of oxygen are strongly related to the Mg/Si ratio of the layer to which the oxygen atoms belong (Figure 6.6a). In the high Mg/Si ratio layer, the self-diffusion coefficients of oxygen show higher values than those in the low Mg/Si ratio layer.

### **16 nm liquid film**

Figure 6.7 shows snapshots of molecular dynamics simulations perpendicular to the a-axis of forsterite. The volume of the melting part increased at 1773 K, and the system is completely melted at 1873 K. Figure 6.8a shows the distribution of elements perpendicular to the (010) surface of forsterite at 1673 K. Figure 6.8b gives the distribution of Q-species perpendicular to the forsterite surface at 1673 K. The altered crystal surfaces exist at  $z = \sim 3$  nm and  $\sim 20$  nm. The nesosilicate structure is altered, and  $\sim 20\%$  of the  $\text{SiO}_4$  tetrahedra formed Si–O–Si bridging in this region. In the near crystal surface, the Si-rich layer exists in the liquid domain. In the domain between the disturbed crystal surface and the Si-rich layer, Si–O–Si bridging is formed, and  $Q^1$  becomes the dominant species. The Mg-rich layer exists on the inside of the Si-rich layer. The composition of the sliced layer of the  $\text{MgSiO}_3$  liquid is heterogeneous and oscillates, whereas the sliced layer is distant from the crystal surface (Figure 6.8a). Figure 6.9 shows the distribution of the direction of the Si–O–Si bridging perpendicular to the forsterite surface. The orientation of the Si–O–Si bridging in the sandwiched liquid film is clearly parallel to the crystal surface. However, the orientation in the disturbed crystal surface is strongly perpendicular to the crystal surface. Figure 6.10b gives the distribution of two-dimensional self-diffusion coefficients of oxygen parallel to the forsterite surface, and Figure 6.10c shows the calculated viscosities. The

two-dimensional self-diffusion coefficients of oxygen are all slightly lower than those of bulk  $\text{MgSiO}_3$  liquids (dotted line). The two-dimensional self-diffusion coefficients of oxygen are strongly related to the Mg/Si ratio of each layer in which the oxygen atoms belong in the liquid region. In the high Mg/Si ratio layers, the self-diffusion coefficients of oxygen show larger values than in the low Mg/Si ratio layers (Figure 6.10a). However, coefficients in altered crystal surface regions are lower than those in liquid regions, in contrast to the case of the 4 nm liquid film.

### **Effect of film thickness**

We show the result of simulation of the system containing films of 7 nm and 28 nm thickness. The layered structure is also found in this system. However, the global decrease of self-diffusion coefficients is much smaller than the interface system with the 4 nm liquid film (Figure 6.11). Figure 6.12 shows the distribution of the Mg/Si ratio, elements and the two-dimensional self-diffusion coefficients of oxygen of the system with a 28 nm liquid film. The layered structure is similar to the case of the 16 nm liquid film. The two-dimensional self-diffusion coefficients of oxygen in the middle part ( $z = 12\text{--}23$  nm) of the liquid films are the same as those of bulk liquids. This means that the  $\text{MgSiO}_3$  liquid film sandwiched by the forsterite (010) surface acts like a bulk liquid in

the region 7 nm apart from the crystal surface. Figure 6.13 shows the calculated viscosities for various film thicknesses. The average viscosity approaches the viscosity of a bulk liquid with increasing film thickness. The average viscosity in the liquid films of 28 nm thickness is nearly the same as that of a bulk liquid. The average viscosity in the thin (<5 nm) liquid film is much higher than that of a bulk liquid.

### **General discussion**

The layered structure that exists in the liquid films in these simulations is caused by the difference in bond strength between Si–O semi-covalent bonds and Mg–O ionic bonds. Si–O–Si bridgings are excessively formed between the altered crystal surface and the Si-rich layer because the strength of Si–O bonding is much higher than that of Mg–O bonding. The excess formation of Si–O–Si bridging in these compositions produce free oxygen atoms. Formation of Si–O–Si bridging depletes the non-bridging oxygen as an acceptor of magnesium atoms and concentrates silicon atoms. The excess free oxygen atoms concentrate magnesium atoms. Consequently, an Si-rich layer is formed in the nearest surface region of the liquid domain, and an Mg-rich layer is formed on the inside of the Si-rich layer on the liquid film (Figure 6.6a and 6.10a). The Q-speciation reflects the Mg/Si ratio on the Si-rich layer because  $Q^4$  species increase in the case of

the 4 nm liquid film. However, the Q-speciation does not reflect the Mg-rich layer. The abundance of  $Q^0$  is too small in the case of the 4 nm film (Figure 6.4), meaning free oxygen atoms are produced. Clustering of the -Si-O- network also occurs. The Q-speciation does not reflect the Mg/Si ratio because the -Si-O- corner shared network makes the cluster. The clustering and layering weaken with increasing film thickness. The weakening can be explained by the degree of freedom in the film structure. The excess free oxygen and magnesium atoms from altered surfaces could not be accepted in the liquid film in the case of a thin film because the degree of freedom in the film structure is small. However, they can be accepted in a liquid film with increasing film thickness. Consequently, the degree of clustering decreases with increasing film thickness (Figure 6.6 and Figures 6.10–12).

The layered structure is also reported by Gurmani et al. (2011). They investigated forsterite– $MgSiO_3$  liquid with a film thickness of up to 8 nm by the classical molecular dynamics method. However, the contrast of composition and decrease of self-diffusion coefficients by the interface was much smaller than in our study. The difference between Gurmani et al. (2011) and our studies is caused by the area of the surface cross section. Horbach et al. (1996) reported the finite-size effects in simulations of silicate glass. According to their study, the system should contain more than 8000 atoms (4–5 nm for

each side of the periodic cell) to avoid the size effects. Gurmani et al. (2011) simulated the same system with approximately 2 nm length sides for the cross section of the interface. The length of the cross section of our simulation is approximately 5 nm to avoid the size effects reported by Horbach et al. (1996).

The structure of the altered crystal surface seems to be different because of the thickness of the liquid films. The concentration of magnesium in the altered crystal surface with the 4 nm liquid film is much higher than that with the 16 nm liquid film (Figures 6.4a and 6.8a). In addition, the orientation of Si–O–Si bridging in the altered crystal surface with the 16 nm liquid film is strongly perpendicular to the crystal surface compared with the surface with the 4 nm liquid film (Figures 6.5 and 6.9). These differences might be explained by the degree of freedom of the configuration of the liquid films. There might be no structural flexibility in the liquid domain to accept the excess magnesium atoms in altered crystal surfaces because there are only 5 layers in the 4 nm liquid film. In contrast, the concentration of magnesium in the altered crystal surface with the 16 nm liquid film is lower than that with the 4 nm liquid film because of the structural flexibility of the liquid film. The surface becomes well-ordered by acceptance of magnesium in liquid and disordered by existence of excess magnesium atoms.

The two-dimensional self-diffusion coefficients parallel to the crystal surface are dependent on their distance from the altered crystal surface. Those coefficients show larger values in Mg-rich layers and smaller values in Si-rich layers. The regional dependences are simply explained by the composition of the sliced layer. Self-diffusion coefficients of network-forming elements in binary silicate liquids depend on their SiO<sub>2</sub> contents (Keller et al. 1982; Keller and Schwerdtfeger 1979). Self-diffusion coefficients of Si and O atoms decrease with increasing SiO<sub>2</sub> contents in bulk silicate liquids because of the difference in bond strength between Si–O covalent bonds and ionic bonds. Consequently, the self-diffusion coefficients of oxygen atoms decrease in Si-rich layers and increase in Mg-rich layers. The two-dimensional self-diffusion coefficients of oxygen in the 4 nm liquid film are lower than those in the 16 nm liquid film by an order of magnitude (Figures 6.4b and 6.8b). The difference in the self-diffusion coefficients might be explained by the structural flexibility of liquid films. The variety of Mg/Si ratios in the 4 nm liquid film is larger than that in the 16 nm liquid film. The degree of freedom of the configuration in the 4 nm liquid film is lower than that in the 16 nm liquid film. The liquid film is strongly structured by the crystal surface in the case of thin liquid films. Consequently, the flexibility of motion of each atom in the 4 nm liquid film is lower than in the 16 nm liquid film, and mobility is decreased by the lower

flexibility.

The oxygen diffusivity is related to shear viscosity by the Einstein–Stokes relation.

The Einstein–Stokes relation is stated as

$$D = kT/6\pi r\eta, \quad (4)$$

where  $D$  is the self-diffusion coefficient,  $k$  is the Boltzmann constant,  $T$  is temperature,  $r$  is the radius of diffusing particles, and  $\eta$  is shear viscosity. This equation has been used with remarkable success in a variety of silicate liquids to relate diffusivity of network forming atoms and shear viscosity (e.g., Oishi et al. 1975; Dunn 1982; Shimizu and Kushiro 1984; Rubie et al. 1993; Lacks et al. 2007). Applying the Einstein–Stokes relation to the results of this study, the viscosity of thin film silicate liquid might be considered to have higher viscosity than bulk liquid by one order of magnitude (Figure 6.6c). In the 16 nm film liquid, the viscosity of the liquid is slightly lower than that of bulk liquid in the near surface region, the same as with bulk liquid in the Mg-rich layer, and oscillates with distance from the crystal surface (Figure 6.10c).

## **Implications**

The melt segregation velocity in partially molten rock is inversely proportional to the melt viscosity (McKenzie 1989). In texturally equilibrated partially molten rocks, melts reside at the grain corners and edges (see Figure 1 of Zhu and Hirth 2003). A melt channel exists on the grain edge, and its cross-sectional area is determined by the dihedral angle, the melt fraction, and grain size. Von Bargen and Waff (1986) showed that the minimum channel cross-sectional area of partially molten rock consists of tetrakaidekahedron grains of varying melt fraction and dihedral angle  $\theta$ . We calculated the viscosity at melt channels using the results of our simulations (Figure 6.13) and geometrical calculation by von Bargen and Waff (1986). Figure 6.14 shows the logarithm of normalized viscosity of melts in melt channels versus melt fraction with two grain sizes and two dihedral angles. Waff and Bulau (1979) showed that the distribution of dihedral angles in partially molten ultramafic rocks is between  $30^\circ$  and  $47^\circ$ . The viscosity becomes higher than bulk liquids by one order of magnitude at lower melt fractions and  $1 \mu\text{m}$  grain. However, viscosity seems to be constant with varying melt fractions in the case of  $10 \mu\text{m}$  grain size. The effect of the silicate crystal–liquid interface is negligible in melt flow in the mantle conditions, postulating the textural equilibrium, because the range in grain size of the mantle is 1 mm to 50 mm (Faul and Jackson 2005). However, a melt film of 0.6 to 3.0 nm thickness was found in deformed

partially molten olivine–orthopyroxene rocks (de Kloe et al. 2000). Consequently, the crystal–liquid interface can affect the melt flow in deformed samples.

### **6.3 Conclusions**

We showed the results of molecular dynamics simulations of forsterite–MgSiO<sub>3</sub> liquid, which contribute to our understanding of the nano-scale structure of the interface and diffusivity of atoms in the interface. From these simulations, the characteristic structure of liquid films in forsterite–MgSiO<sub>3</sub> liquid interface is observed. We also observe the layered structure of an altered crystal surface, an Si-rich layer, and an Mg-rich layer in the crystal–liquid interface. The layered structure is formed by the strength difference between Si–O covalent bonds and Mg–O ionic bonds. Si–O–Si bridging and free oxygen atoms are excessively formed in the near surface because Si–O bonding is much stronger than Mg–O bonding. The difference in the layered structure indicated by the thickness of MgSiO<sub>3</sub> liquid films might be caused by the difference in degree of freedom of the configuration in liquid films. The two-dimensional diffusivity of oxygen is controlled by two factors. One factor is the thickness of the liquid films that decreases oxygen diffusivity with decreasing film thickness because of the decrease of degree of freedom of the configuration in the liquid films. The other factor is the composition of

the sliced layer, where oxygen diffusivity increases with increasing Mg/Si ratio because Si–O bonding is much stronger than Mg–O bonding. The degree of Mg/Si layering strongly depends on film thickness and decreases with increasing film thickness. The effect of the crystal–liquid interface is negligible in texturally equilibrated rocks. However, the interface can affect the melt flow in deformed samples because the grain boundary melt film of several nanometer thickness exists stably in deformed partially molten rocks.

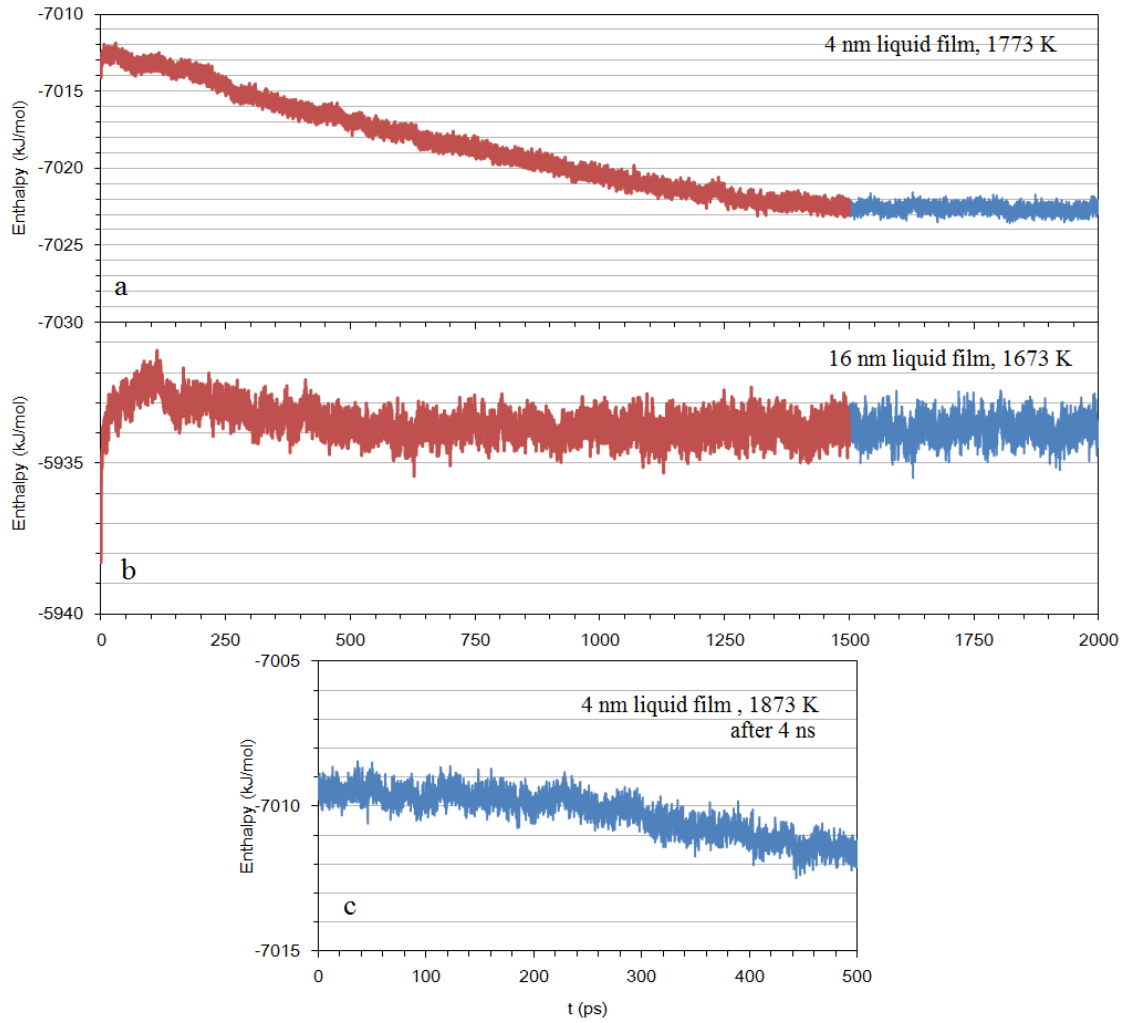


Figure 6.1. Plots of enthalpy of the simulated systems as a function of time. The

enthalpy is plotted as molar enthalpy of (a)  $\text{Mg}_{1.5459}\text{Si}_{1.0000}\text{O}_{3.5480}$ , (b)

$\text{Mg}_{1.2425}\text{Si}_{1.0000}\text{O}_{3.24345}$ , and (c)  $\text{Mg}_{1.5459}\text{Si}_{1.0000}\text{O}_{3.5480}$ .

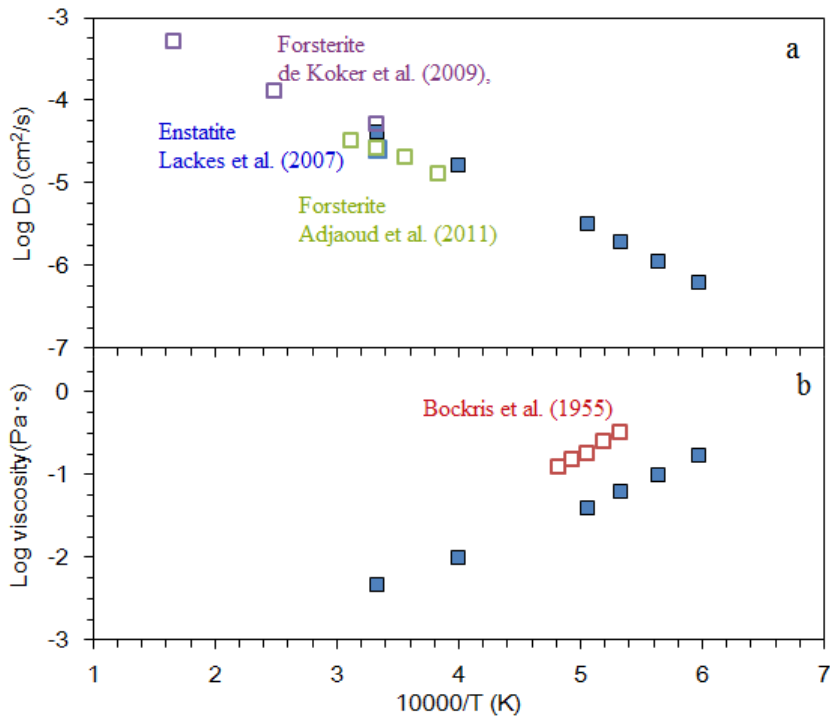


Figure 6.2. Comparisons of self-diffusion coefficients of oxygen and viscosities. (a)

Comparison of diffusion coefficients of oxygen  $\text{MgSiO}_3$  bulk liquid with other molecular dynamics studies. Closed squares indicate our study, and purple, green, and blue open squares indicate data of forsterite liquid from de Koker et al.

(2009), Adjaoud et al. (2011), and enstatite liquid by Lacks et al. (2007),

respectively. (b) Comparison of calculated viscosities with experiment results.

The experimental data are taken from Bockris et al. (1955). Viscosities are

calculated using the Einstein–Stokes relation and the effective radius reported by

Lacks et al. (2007).

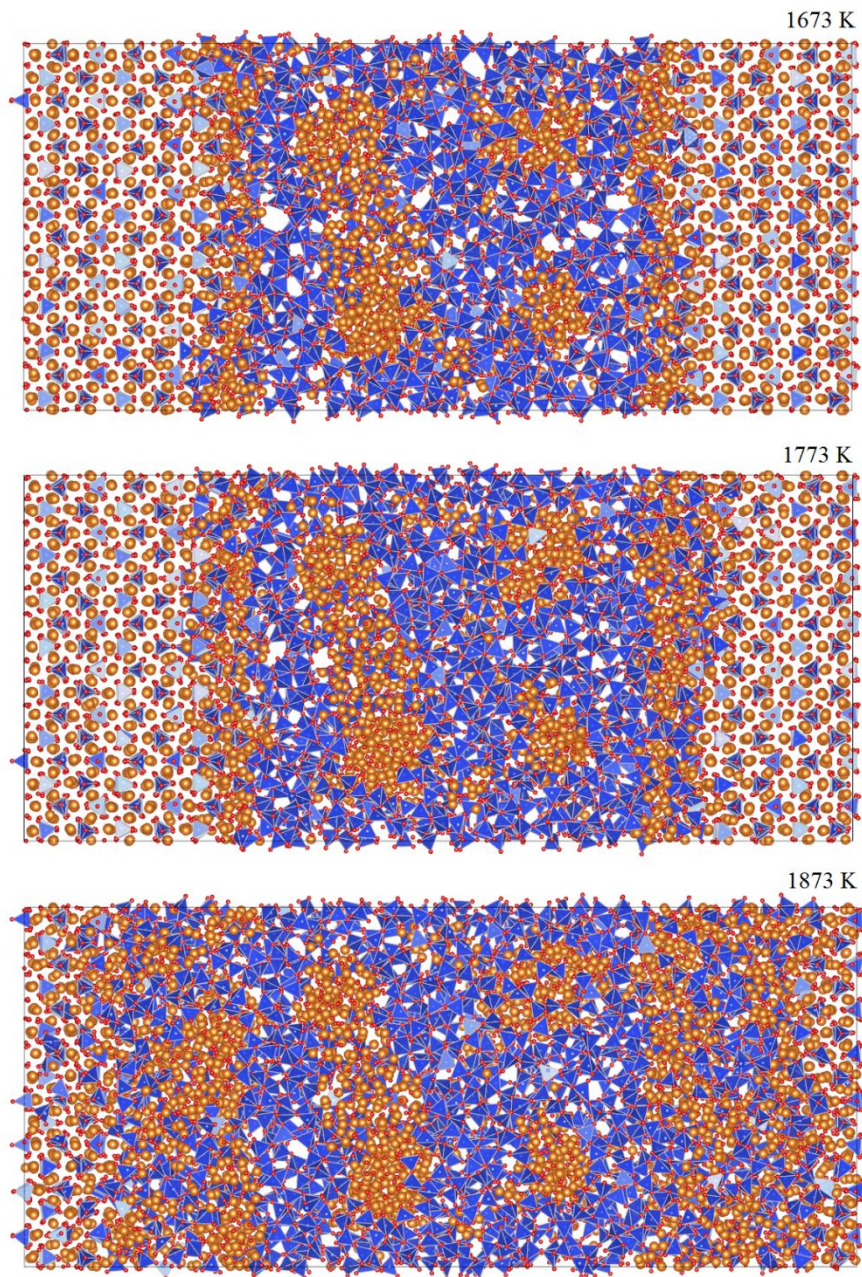


Figure 6.3. Snapshots of molecular dynamics simulations. The simulations are for the system forsterite-8000 atom  $\text{MgSiO}_3$  liquid perpendicular to the forsterite a-axis at various temperatures. The red, blue, and orange spheres represents O, Si, and Mg atoms, respectively.

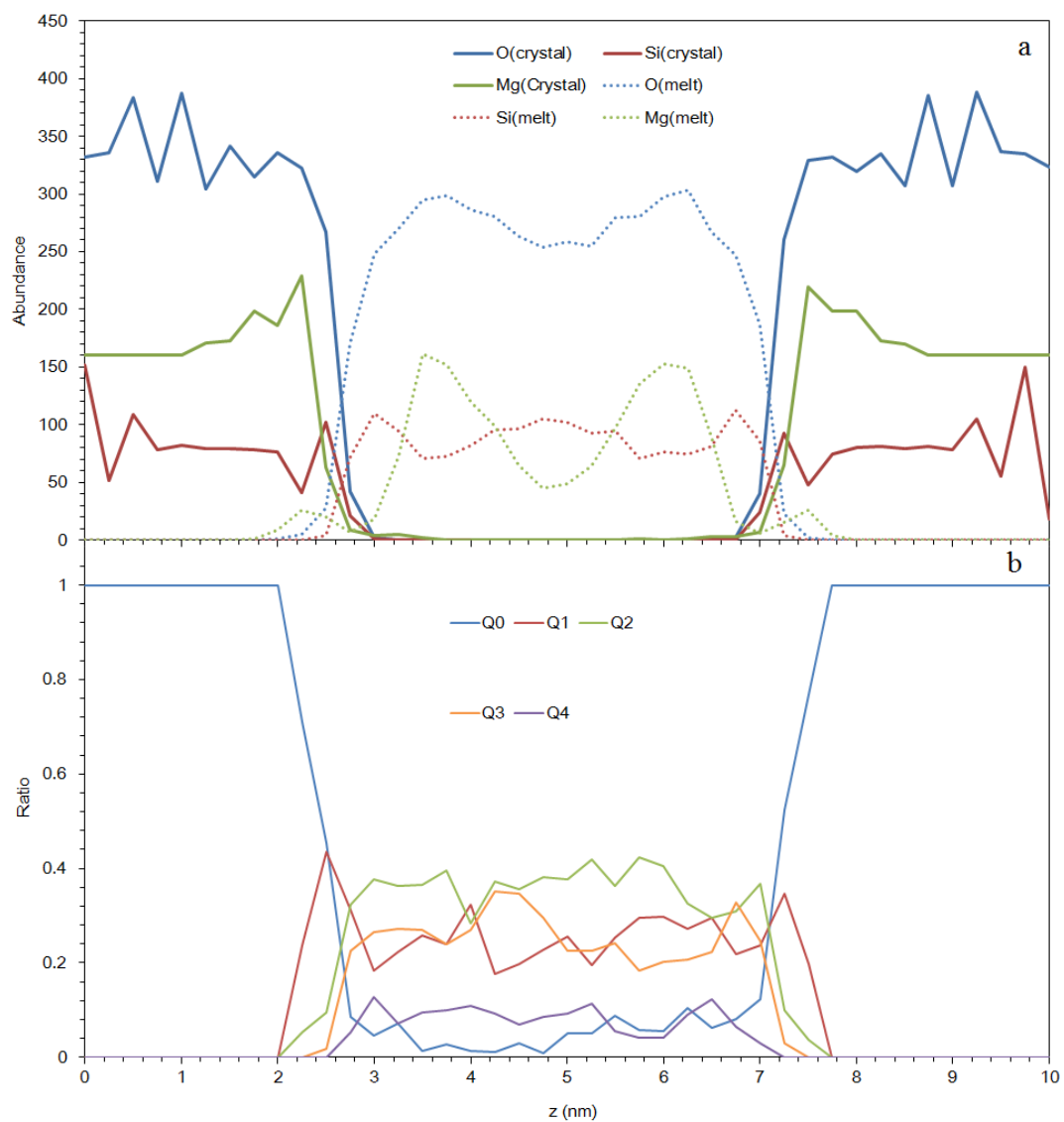


Figure 6.4. Distribution of elements and Q-species at 1773 K. (a) Distribution of elements perpendicular to the (010) surface of forsterite. (b) Distribution of Q-species perpendicular to the forsterite surface.

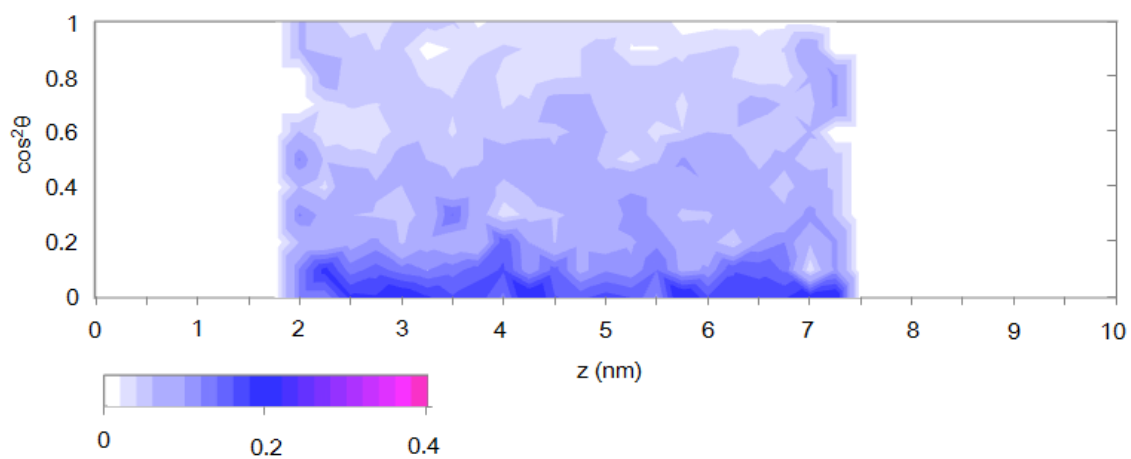


Figure 6.5. Distribution of the direction of Si–O–Si bridging perpendicular to the forsterite surface. The directions are shown as the  $\cos^2\theta$  of the Si–Si vector and z-axis.

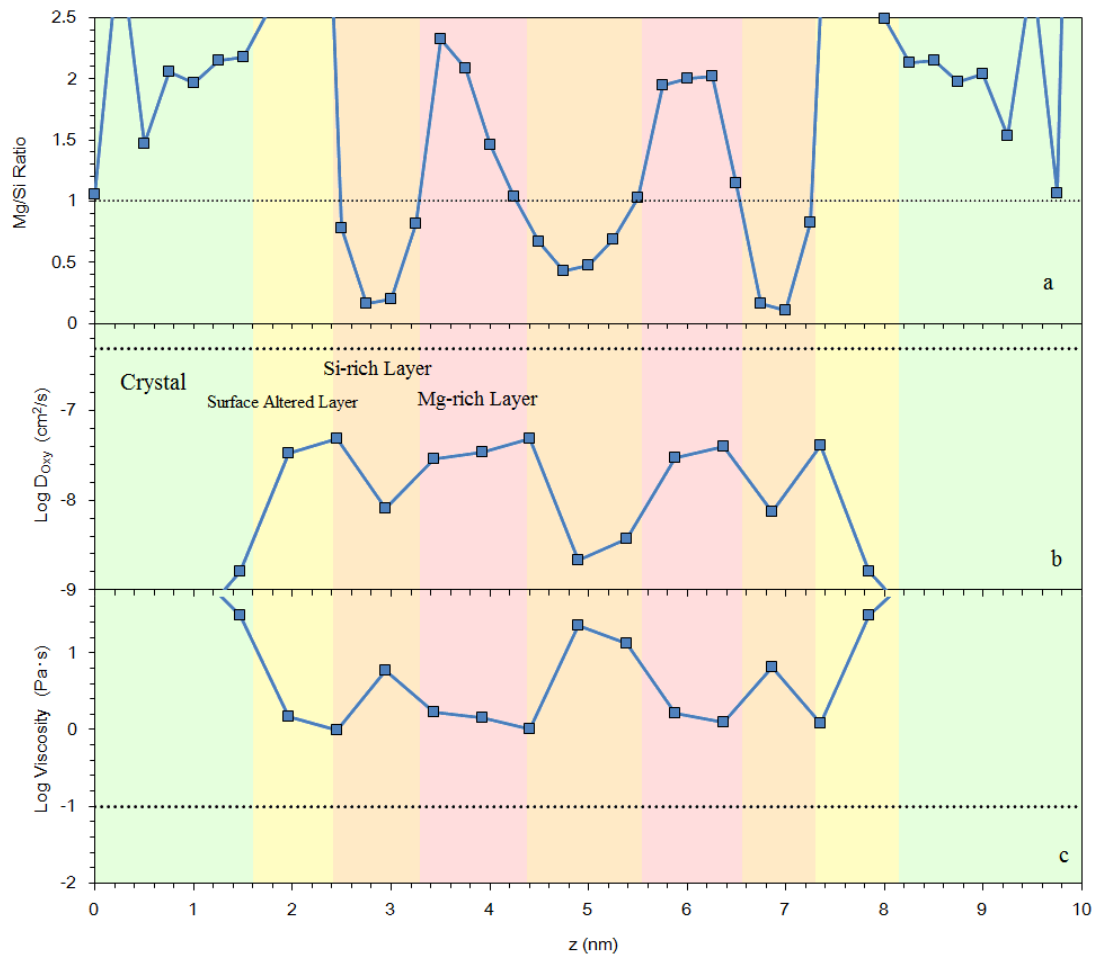


Figure 6.6. Distribution of Mg/Si ratios, self-diffusion coefficients of oxygen, and viscosities at 1773 K. (a) Distribution of Mg/Si ratios perpendicular to the (010) surface of forsterite. (b) Distribution of two-dimensional self-diffusion coefficients of oxygen parallel to the forsterite surface. (c) Distribution of viscosities. The dotted line represents the value of bulk  $MgSiO_3$  liquid.

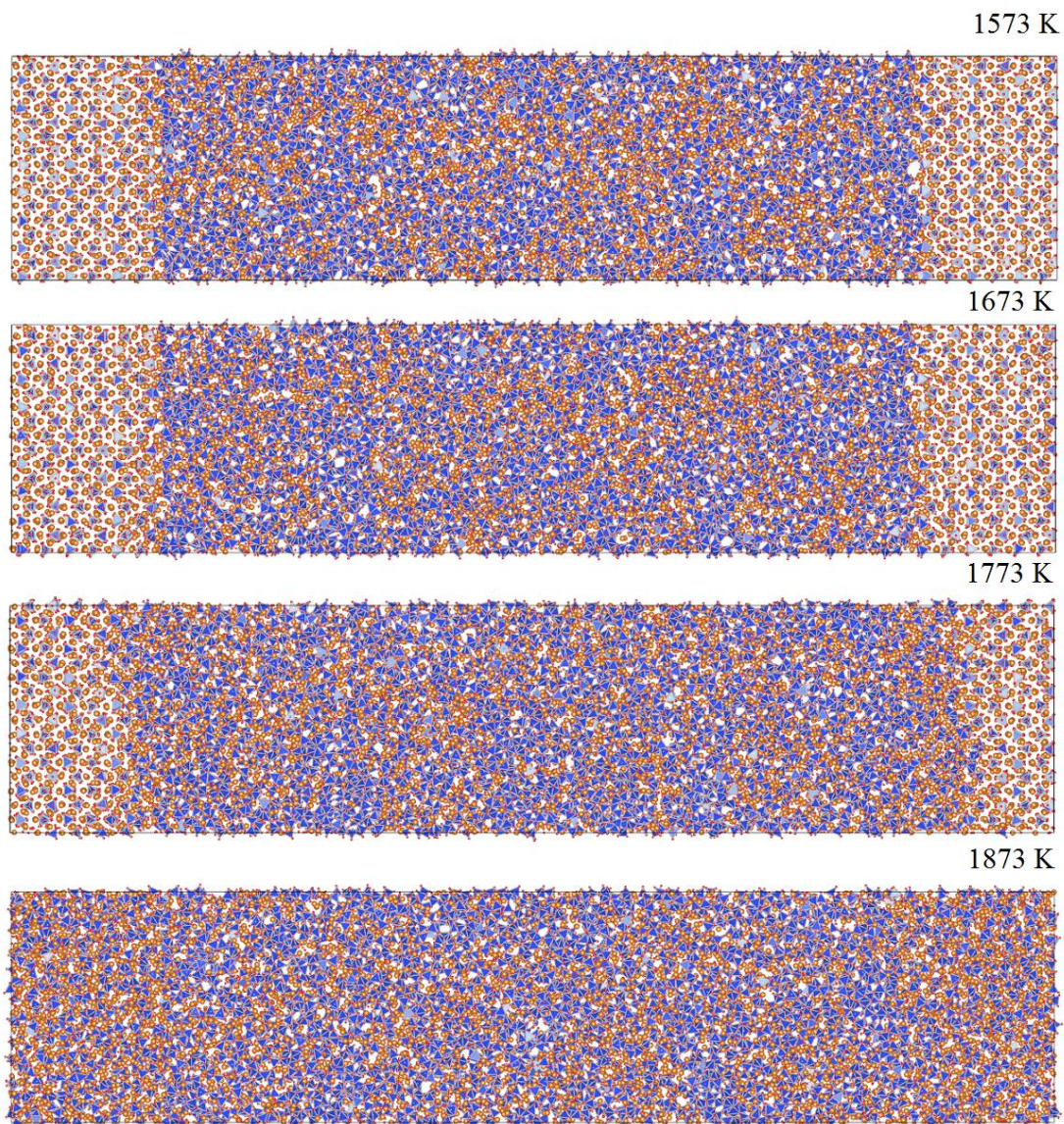


Figure 6.7. Snapshots of molecular dynamics simulations. Simulations are for the system forsterite-30,000 atom  $\text{MgSiO}_3$  liquid perpendicular to the a-axis of forsterite at various temperatures. The red, blue, and orange spheres represents O, Si, and Mg atoms, respectively.

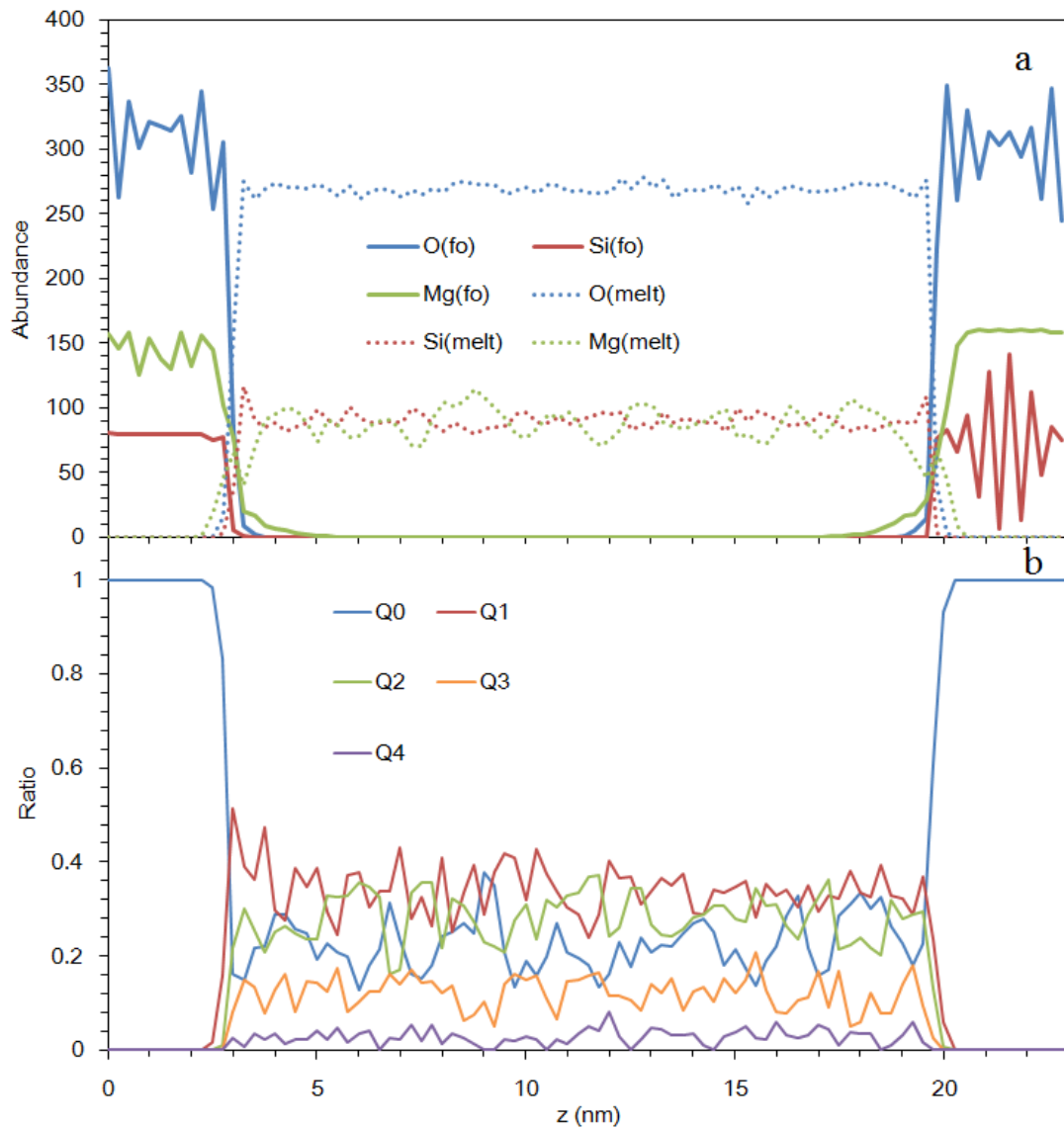


Figure 6.8. Distribution of elements and Q-species at 1673 K. (a) Distribution of elements perpendicular to the (010) surface of forsterite. (b) Distribution of Q-species perpendicular to the forsterite surface.

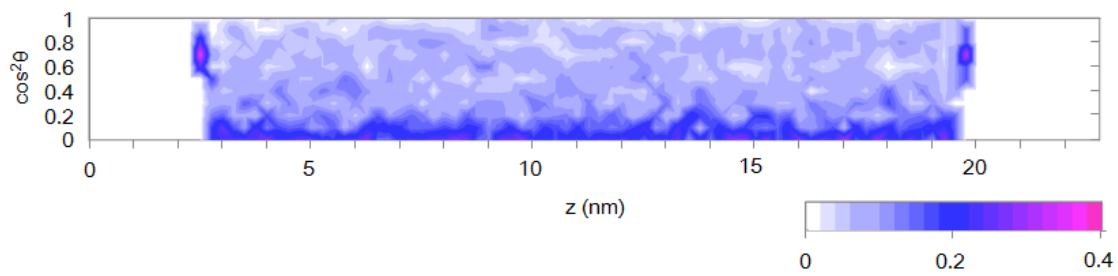


Figure 6.9. Distribution of the direction of the Si–O–Si bridging perpendicular to the forsterite (010) surface. The directions are shown as the  $\cos^2\theta$  of the Si–Si vector and z-axis.

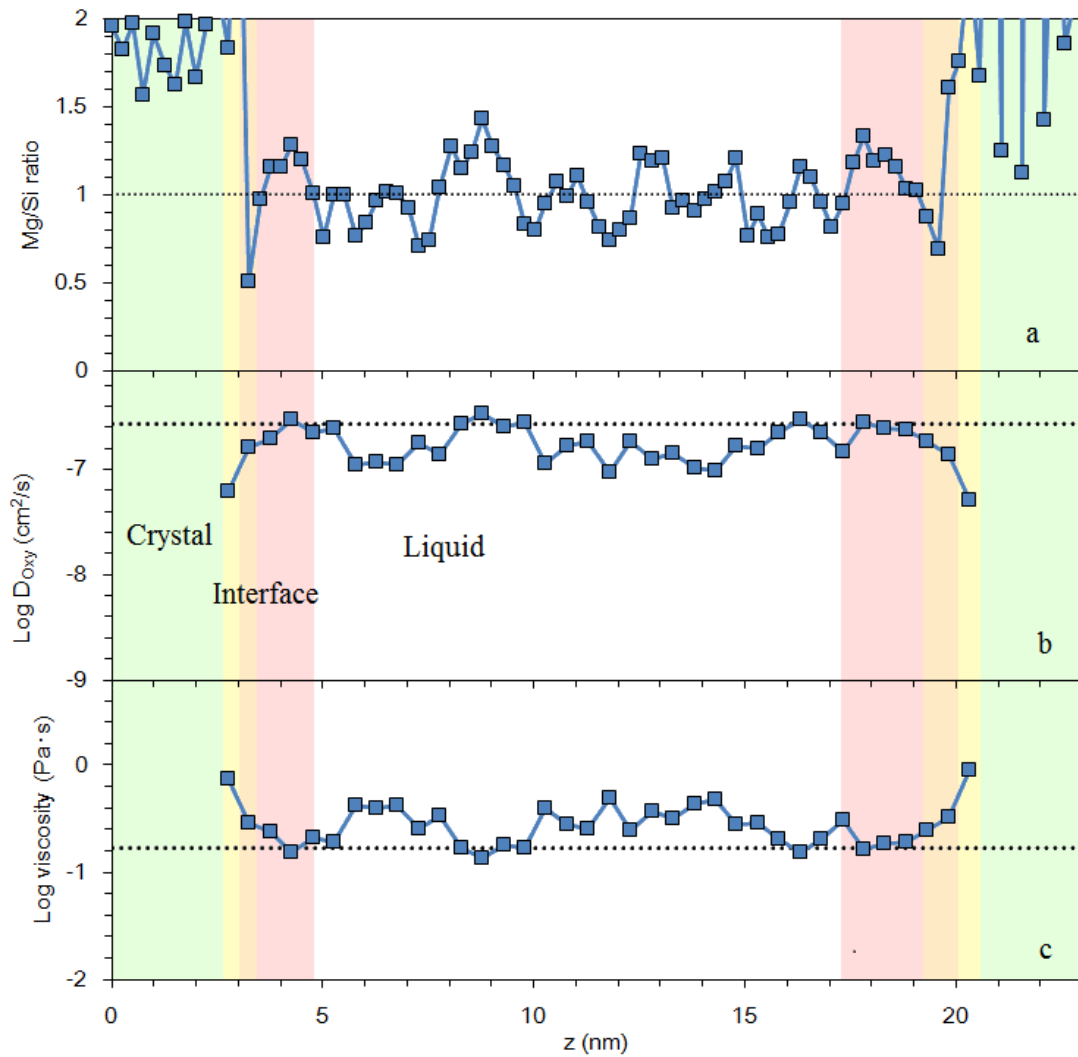


Figure 6.10. Distribution of Mg/Si ratios, self-diffusion coefficients of oxygen, and viscosities at 1673 K. (a) Distribution of Mg/Si ratio perpendicular to the (010) surface of forsterite. (b) Distribution of two-dimensional self-diffusion coefficients of oxygen parallel to the forsterite surface. (c) Distribution of viscosities. The dotted line represents the value of bulk  $\text{MgSiO}_3$  liquid.

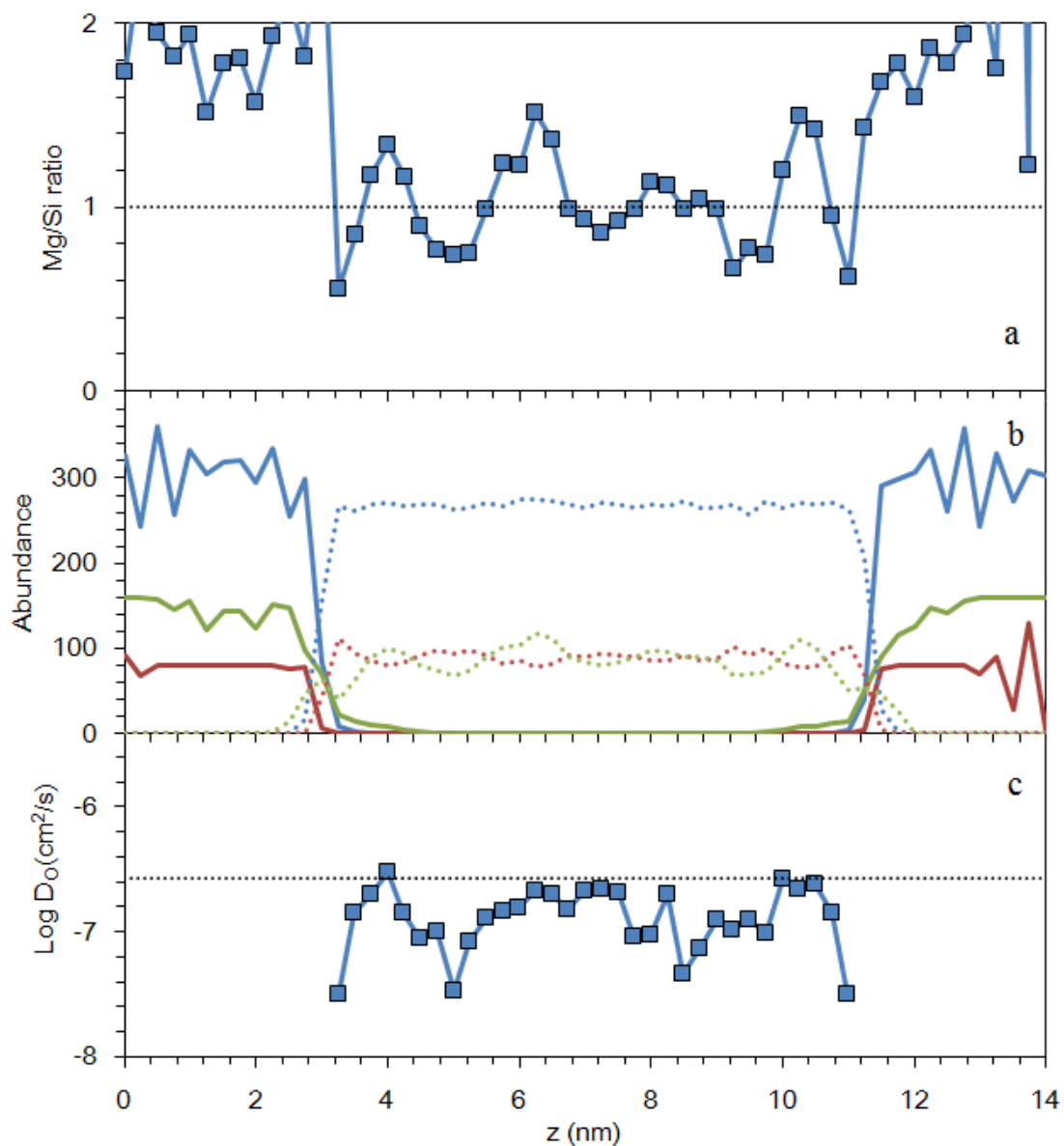


Figure 6.11. Mg/Si ratios, elements, and self-diffusion coefficients of oxygen for forsterite– $\text{MgSiO}_3$  with 7 nm liquid film. (a) Distribution of Mg/Si ratio perpendicular to the (010) surface of forsterite at 1673 K. (b) Distribution of elements perpendicular to the (010) surface of forsterite at 1673 K. (c) Distribution of two-dimensional self-diffusion coefficients of oxygen parallel to the forsterite surface at 1673 K.

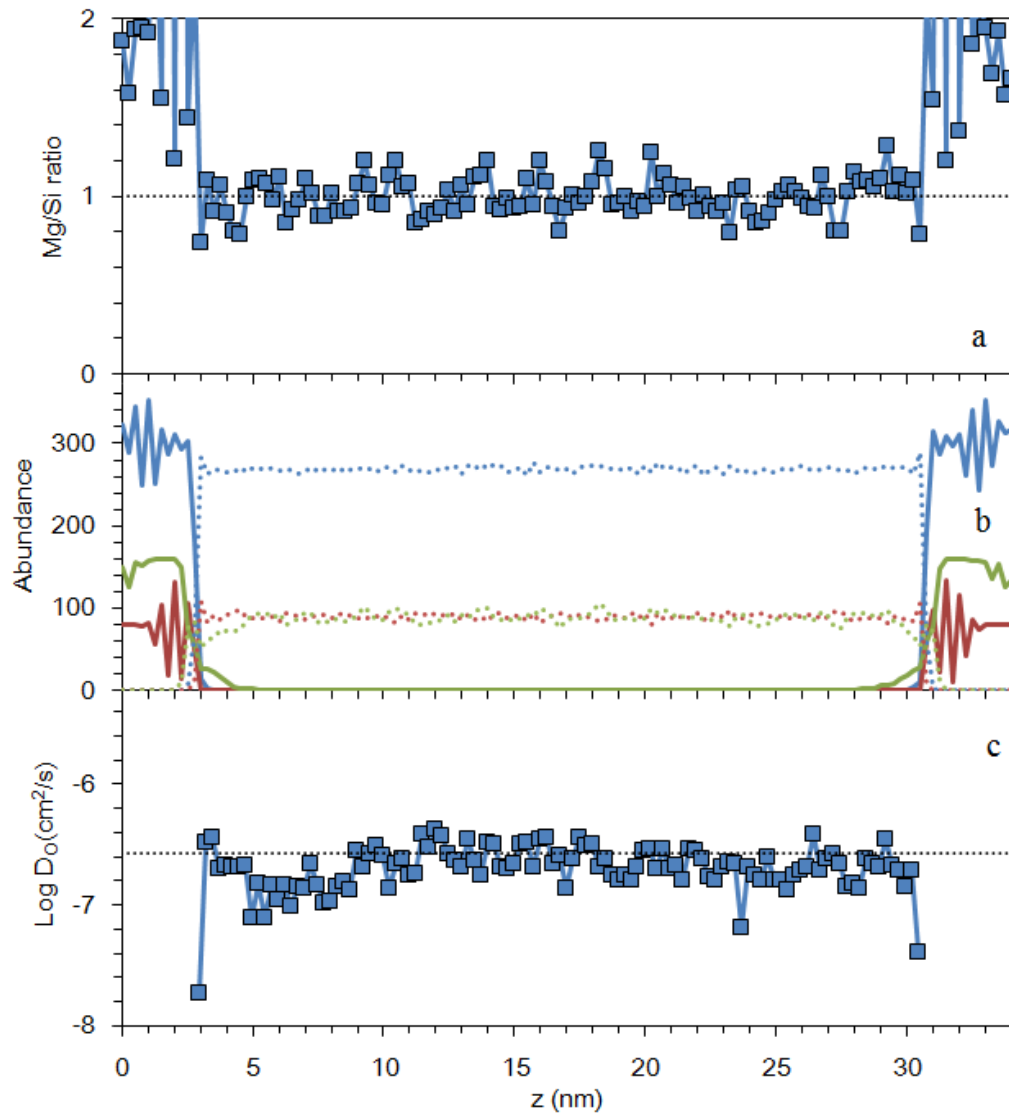


Figure 6.12. Mg/Si ratios, elements, and self-diffusion coefficients of oxygen for forsterite– $\text{MgSiO}_3$  with 28 nm liquid film. (a) Distribution of Mg/Si ratio perpendicular to the (010) surface of forsterite at 1673 K. (b) Distribution of elements perpendicular to the (010) surface of forsterite at 1673 K. (c) Distribution of two-dimensional self-diffusion coefficients of oxygen parallel to the forsterite surface at 1673 K.

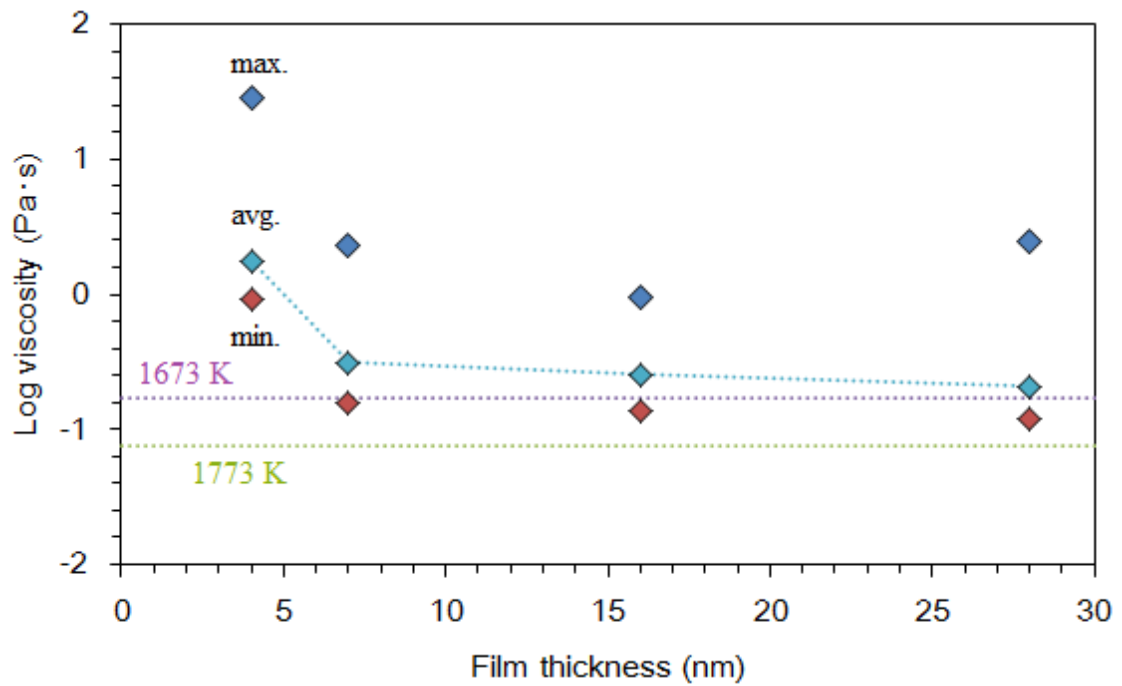


Figure 6.13. Plots of viscosity as a function of film thickness. Max. and min. denote the maximum and minimum viscosity in the liquid region, respectively. Avg. means the average of the entire liquid film (4 and 7 nm) and the average of the region 5 nm apart from the crystal surface (16 and 28 nm).

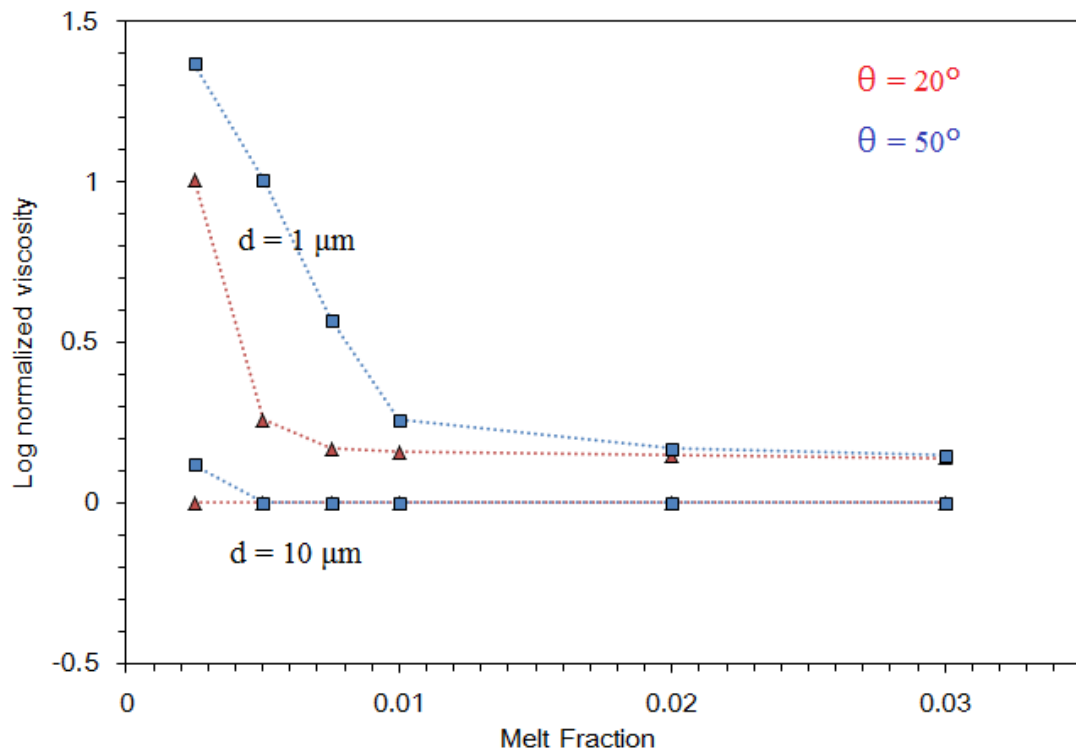


Figure 6.14. Logarithm plots of normalized viscosity as a function of melt fraction at melt channels in texturally equilibrated partially molten rock.

**Table 6.1**

Inter-atomic potential parameters

Atomic parameters	q	a (Å)	b (Å)	c (kJ/mol · Å <sup>3</sup> )
Si	2.23607	0.99759	0.0830	0.000
O	-1.11803	1.81819	0.1539	27.400
Mg	1.11803	1.09881	0.0470	40.000
Pair parameters	D <sub>1</sub> (kJ/mol)	β <sub>1</sub> (1/Å)	D <sub>2</sub> (kJ/mol)	β <sub>2</sub> (1/Å)
Si-O	668428	59.636	-105335	45.514
Mg-O	28960.0	5.0	-1556.8	2.24
3-body parameters	f (kJ/mol)	θ <sub>0</sub> (degree)	r <sub>m</sub> (Å)	g <sub>r</sub> (1/Å)
Si-O-Si	0.0006	147.0	0.170	168.0

**Table 6.2**

Comparison of lattice constants between MD simulations and experiments

	Forsterite		Enstatite	
	MD	Exp <sup>1</sup>	MD	Exp <sup>3</sup>
a (Å)	4.8709	4.7534	18.921	18.230
b (Å)	10.2820	10.1902	8.840	8.817
c (Å)	6.1249	5.9783	5.388	5.181
Density (g/cm <sup>3</sup> )	3.0467	3.2275	2.960	3.203
K <sub>0</sub> (GPa)	128	129 <sup>2</sup>	95.0	95.8 <sup>4</sup>
K'	5.69	4.2 <sup>2</sup>	11.0	14.9 <sup>4</sup>

<sup>1</sup>Fujino et al. (1981), <sup>2</sup>Duffy et al. (1995), <sup>3</sup>Morimoto and Koto (1969), <sup>4</sup>Angel and

Hugh-Jones (1994)

## 7. References

Adjaoud, O., Steinle-Neumann, G., Jahn S., (2011) Transport properties of  $\text{Mg}_2\text{SiO}_4$  liquid at high pressure: Physical state of magma ocean, *E. P. S. L.*, **312**, 463-470.

Almenningen, A., Bastiansen, O., Ewing, V., Hedberg, K., Trøttestad, M., (1963), The molecular structure of disiloxane,  $(\text{SiH}_3)_2\text{O}$ , *Acta Chemica Scandinavica*, **17**, 2455-2460.

Angel RJ, Hugh-Jones DA, (1994) Equations of state and thermodynamic properties of enstatite pyroxenes. *J. Geophys. Res.* **99**, 19777-19783.

Becke, A., D., (1988), Density-functional exchange-energy approximation with correct asymptotic behavior, *Phys. Rev. A*, **38**, 3098.

Bish, D. L., (1993), Rietveld refinement of the kaolinite structure at 1.5 K., *Clays and Clay Min.*, **43**, 738-744.

Bockris J. O'M., Mackenzie J. D., Kitchener J. A., (1955) Viscous flow in silica and binary liquid silicates, *Trans Faraday Soc.*, **51**, 1734-1748.

Cruickshank, D. W. J., (1961), Role of 3d-orbitals in  $\pi$ -bonds between (a) silicon, phosphorus, sulfur or chlorine and (b) oxygen or nitrogen, *J. Chem. Society*, **1077**, 5486-5504.

De Kloe R., Drury M. R., van Roermund H. L. M., (2000), Evidence for stable grain boundary melt films in experimentally deformed olivine-orthopyroxene rocks, *Phys. Chem. Min.*, **27**, 480-494.

De Koker, N. P., Stixrude L., Karki B., (2009), Thermodynamics, structure, dynamics, and freezing of  $\text{Mg}_2\text{SiO}_4$  liquid at high pressure, *G.C.A.*, **72**, 1427-1441.

Devine, R. A. B., Dupree, R., Farnan, I., Capponi, J. J., (1987), Pressure-induced bond-angle variation in amorphous  $\text{SiO}_2$ , *Phys. Rev. B.*, **35**, 2560-2562.

Diefenbacher, J., McMillan, P. F., Wolf, G. H., (1998), Molecular dynamics simulations of  $\text{Na}_2\text{Si}_4\text{O}_9$  at high pressure, *J. Phys. Chem. B*, **102**, 3003-3008.

Duffy, T. S., Zha, C., Downs, R. T., Mao, H., Hemley, R. J., (1995) Elasticity of forsterite to 16GPa and the composition of the upper mantle. *Nature*. **378**, 170-173.

Dunn T, (1982) Oxygen diffusion in three silicate melts along the join diopside-anorthite. *G.C.A.* **46**, 2293-2299.

Faul U. H., Jackson I., (2005), The seismological signature of temperature and grain size variations in the upper mantle, *E. P. S. L.*, **234**, 119-134.

doi:10.1016/j.epsl.2005.02.008

Foster, J. P., Weinhold, F., (1980), Natural hybrid Orbitals, *J. Am. Chem. Soc.*, **102**, 7211-7218.

Fujino K, Sasaki S, Takeuchi Y, Sadanaga R, (1981) X-ray determination of electron distributions in forsterite, fayalite and tephroite. *Acta. Cryst.* **B37**, 513-518.

Funamori, N., Yamamoto, S., Yagi, T., Kikegawa, T., (2004), Exploratory studies of silicate melt at high pressures and temperature by in situ X-ray diffraction, *J. Geophys. Res.*, **109**, B03203.

Gaussian 09, Revision **A.1**, M. J. Frisch, G. W. Trucks, H. B. Schlegel, G. E. Scuseria, M. A. Robb, J. R. Cheeseman, G. Scalmani, V. Barone, B. Mennucci, G. A. Petersson, H. Nakatsuji, M. Caricato, X. Li, H. P. Hratchian, A. F. Izmaylov, J. Bloino, G. Zheng, J. L. Sonnenberg, M. Hada, M. Ehara, K. Toyota, R. Fukuda, J. Hasegawa, M. Ishida, T. Nakajima, Y. Honda, O. Kitao, H. Nakai, T. Vreven, J. A. Montgomery, Jr., J. E. Peralta, F. Ogliaro, M. Bearpark, J. J. Heyd, E. Brothers, K. N. Kudin, V. N. Staroverov, R. Kobayashi, J. Normand, K. Raghavachari, A. Rendell, J. C. Burant, S. S. Iyengar, J. Tomasi, M. Cossi, N. Rega, J. M. Millam, M. Klene, J. E. Knox, J. B. Cross, V. Bakken, C. Adamo, J. Jaramillo, R. Gomperts, R. E. Stratmann, O. Yazyev, A. J. Austin, R. Cammi, C. Pomelli, J. W. Ochterski, R. L. Martin, K. Morokuma, V. G. Zakrzewski, G. A. Voth, P. Salvador, J. J. Dannenberg, S. Dapprich, A. D. Daniels, Ö. Farkas, J. B. Foresman, J. V. Ortiz, J. Cioslowski, and D. J. Fox, Gaussian, Inc., Wallingford CT, 2009.

Geisinger, K. L., Gibbs, G. V., Navrotsky, A., (1985), A molecular orbital study of bond length and angle variations in framework structures, *Phys. Chem. Minerals*, **11**, 266-283.

Gibbs, G. V., Prewitt, C. T., Baldwin, K. J., (1977), A study of the structural chemistry of coesite, *Z. Kristallogr*, **145**, 108-123.

Gurmani S. F., Jahn S., Brasse H., Schilling F. R., (2011), Atomic scale view on partially molten rocks: Molecular dynamics simulations of melt-wetted olivine grain boundaries, *J. Geophys. Res.*, **116**, V12209.

Hariya, Y. and G. C. Kennedy, (1968), Equilibrium study of anorthite under high pressure and high temperature, *American Journal of Science*, **266**, 193-203

Head-Gordon, M., Pople, J. A., Frisch, M. J., (1988), MP2 energy evaluation by direct methods, *Chem. Phys. Letters*, **153**, 503-506.

Hehre, W. J., Stewart R. F., Pople, J. A., (1969), Self-consistent molecular-orbital methods. 1. Use of Gaussian expansion of Slater-type atomic orbitals, *J. Chem. Physics*, **51**, 2657.

Hiraga T, Anderson LM, Zimmerman ME, Mei S, Kohlstedt DL, (2002) Structure and chemistry of grain boundaries in deformed, olivine + basalt and partially molten lherzolite aggregates : evidence of melt-free grain boundaries. *Cont. Min. Pet.* **144**,163-175.

Horbach J., Kob W., Binder K., Angell C. A., (1996), Finite size effects in simulations of glass dynamics, *Phys. Rev. E.*, **54**, R5897-R5900.

Ichikawa Y, Kawamura K, Nakano M, Kitayama K, Seiki T, Theramast N, (2001) Seepage and consolidation of bentonite saturated with pure- or salt-water by the method of unified molecular dynamics and homogenization analysis. *Engineering Geology*. **60**, 127-138.

Jung I, Deckerov SA, Pelton AD, (2004) Critical thermodynamic evaluation and optimization of the FeO-Fe<sub>2</sub>O<sub>3</sub>-MgO-SiO<sub>2</sub> system. *Metall. Mater. Trans.* **35**,877-889.

Keller H, Schwerdtfeger K, (1979) Tracer diffusivity of Si<sup>31</sup> in Ca-SiO<sub>2</sub> melts at 1600°C. *Metall. Trans. B.* **10**, 551-554

Keller H, Schwerdtfeger K, Petri H, Hölzle, Hennesen K, (1982) Tracer diffusivity of O<sup>18</sup> in Ca-SiO<sub>2</sub> melts at 1600°C. *Metall. Trans. B.* **13**, 237-240

Kubicki, J. D., Sykes, D., (1993), Molecular orbital calculations on H<sub>6</sub>Si<sub>2</sub>O<sub>7</sub> with a variable Si-O-Si angle: Implications for the high pressure vibrational spectra of silicate glasses, *American Mineralogist*, **78**, 253-259.

Kushiro, I., (1976), Changes in viscosity and structure of melt of NaAlSi<sub>2</sub>O<sub>6</sub> composition at high pressures, *J. Geophys. Research*, **81**, 1955-1958.

Kushiro, I., (1977), Phase transformation in silicate melts under upper-mantle conditions. *High-Pressure Research: Application in Geophysics*, (Academic Press), Manghnani, M. H. and Akimoto, S. (eds), 25-37.

Kushiro, I., (1978), Viscosity and structural changes of albite ( $\text{NaAlSi}_3\text{O}_8$ ) melt at high pressures, *E. P. S. L.*, **41**, 87-90.

Kushiro, I., (1980), Viscosity, density, and structures of silicate melts at high pressures, and their petrological applications, *Physics of Magmatic Process*, (Princeton University), Hargraves, R. B. (eds), 92-120.

Lacks D. J., Rear D. B., van Orman J. A., (2007), Molecular dynamics investigation of viscosity, chemical diffusivities and partial molar volumes of liquids along the MgO-SiO<sub>2</sub> join as functions of pressure, *G.C.A.*, **71**, 1312-1323.

Lee, C., Yang, W., Parr, R. G., (1988), Development of the Colle-Salvetti correlation-energy formula into a functional of the electron density, *Phys. Rev. B*, **37**, 785.

Levien, L., Prewitt, C. T., Weidner, D. J. (1980). Structure and elastic properties of quartz at pressure. *American Mineralogist*, **65**, 920-930.

Maekawa, H., Maekawa, T., Kawamura, K., Yokokawa, T. (1991). The structural groups of alkali silicate glasses determined from  $^{29}\text{Si}$  MAS-NMR. *Journal of Non-Crystalline Solids*, **127**, 53-64.

McKenzie D., (1989), Some remarks on the movement of small melt fractions in the mantle, *E. P. S. L.*, **95**, 53-72.

McLean, A. D., Chandler, G. S., (1980), Contracted Gaussian-basis sets for molecular calculations. 1. 2nd row atoms,  $Z = 11-18$ , *J. Chem. Physics*, **72**, 5639-5648.

McMillan, P. F., Piriou, B., Couty, R., (1984). A Raman study of pressure-densified vitreous silica. *J. Chem. Phys.* **81**, 4234.

Meade, C., Hemley, R., Mao, H. K., (1992), High-pressure X-ray diffraction of  $\text{SiO}_2$  glass, *Phys. Rev. Letters*, **69**, 1387-1390.

Momma K, Izumi F, (2011) VESTA 3 for three-dimensional visualization of crystal, volumetric and morphology data. *J. Appl. Cryst.* **44**, 1272-1276.

Morimoto N, Koto K, (1969) The crystal structure of orthoenstatite. *Zeits Krist.* **129**, 65-83.

Mulliken, R. S., (1955) Electronic population analysis on LCAO-MO molecular wave functions. 1. *J. Chem. Physics*, **23**, 1833-1840.

Mysen, B. O., (1990). Effect of Pressure, Temperature, and Bulk Composition on the Structure and Species Distribution in Depolymerized Alkali Aluminosilicate Melts and Quenched Melts. *J. Geophys. Res.*, **95**, pp. 15733-15744.

Navrotsky, A., Geisinger, A. L., McMillan, P., Gibbs, G. V., (1985), The tetrahedral framework in glasses and melts – Inferences from molecular orbital calculations and implications for structure, thermodynamics and physical properties, *Phys. Chem. Minerals*, **11**, 284-298.

Newton, M. D., Gibbs, G. V., (1980), *Ab Initio* calculated geometries and charge distributions for  $\text{H}_4\text{SiO}_4$  and  $\text{H}_6\text{Si}_2\text{O}_7$  compared with experimental values for silicates and siloxanes, *Phys. Chem. Minerals*, **6**, 221-246.

Noritake, F., Kawamura, K., Yoshino, T., Takahashi, E., (2012) Molecular dynamics simulation and electrical conductivity measurement of  $\text{Na}_2\text{O} \cdot 3\text{SiO}_2$  melt under high pressure; relationship between its structure and properties, *J. Non-Cryst. Solids*, **358**, 3109-3118.

Ohtani, E., Taulelle, F., Angell, C. A., (1985),  $\text{Al}^{3+}$  coordination changes in liquid aluminosilicates under pressure, *Nature*, **314**, 78-81.

Oishi Y, Terai R, Ueda H, (1975) Oxygen diffusion in liquid silicates and relation to their viscosity. *Mass Trans. Phenom. Cer.* **9**, 297-310

Perdew, J. P., Burke, K., Ernzerhof, M., (1996), Generalized gradient approximation made simple, *Phys. Rev. Letters*, **77**, 3865.

Poe, B. T., McMillan, P. F., Rubie, D. C., Chakraborty, S., Yarger, J., Diefenbacher, J., (1997), Silicon and oxygen self-diffusivities in silicate liquids measured to 15 gigapascals and 2800 kelvin, *Nature*, **276**, 1245-1247.

Raghavachari, K., Binkley, J. S., Seeger, R., Pople, J. A., (1980), Self-consistent molecular orbital methods. 20. Basis set for correlated wave-functions, *J. Chem. Physics*, **72**, 650-654.

Reed, A. E., Curtiss, L. A., Weinhold, F., (1988), Intermolecular interactions from a natural bond orbital, donor-acceptor viewpoint, *Chem. Review*, **88**, 899-926.

Reed, A. E., Weinhold, F., Weinstock, R. B., (1985), Natural population analysis, *J. Chem. Physics*, **83**, 735.

Rubie DC, Ross CR, Carroll MR, Elphick SC, (1993) Oxygen self-diffusion in  $\text{Na}_2\text{Si}_4\text{O}_9$  liquid up to 10GPa and estimation of high-pressure melt viscosities. *Am. min.* **78**, 574-582.

Sakamaki, T., Ohtani, E., Urakawa, S., Suzuki, A., Katayama, Y., (2009), Measurement of hydrous peridotite magma density at high pressure using the X-ray absorption method, *E. P. S. L.*, **287**, 293-297.

Sakamaki, T., Wang, Y., Park, C., Yu, T., Shen, G., (2012), Structure of jadeite melt at high pressure up to 4.9 GPa, *J. App. Physics*, **111**, 112623.

Sakuma H, Kawamura K, (2009) Structure and dynamics of water on muscovite mica surfaces. *G.C.A.* **73**, 4100-4110.

Sakuma H, Tsuchiya T, Kawamura K, Otsuki K, (2003) Large self-diffusion of water on brucite surface by ab initio potential energy surface and molecular dynamics simulations. *Surface Sci.* **536**, L396-L402.

Scarfe, C. M., Myasen B. O., Virgo, D., (1979), Changes in viscosity and density of melts of sodium disilicate, sodium metasilicate and siopside composition with presrue, *Carnegie Inst. Wash. Yearbook*, **78**, 574-582.

Shimizu N, Kushiro I, (1984) Diffusivity of oxygen in jadeite and diopside melts at high pressures. *G.C.A.* **48**, 1295-1303.

Suzuki, A., Ohtani, E., Funakoshi, K., Terasaki, H., Kubo, T., (2002), Viscosity of albite melt at high pressure and high temperature, *Phys. Chem. Minerals*, **29**, 159-165.

Tsuneyuki, S., (1996), Molecular dynamics simulation of silica with a first-principles interatomic potential, *Molecular Engineering*, **6**, 157-182.

Stolper, E. M., Ahrens, T. J., (1987), On the nature of pressure-induced coordination changes in silicate melts and glasses, *Geophys. Res. Letters*, **14**, 1231-1233.

Von Bargen N., Waff H. S., (1986), Permeabilities, interfacial areas and curvatures of partially molten systems: Results of numerical computations of equilibrium microstructures, *J. Geophys. Res.*, **91**, 9261-9276.

Waff H. S., Bulau J. R., (1979), Equilibrium fluid distribution in an ultramafic partial melt under hydrostatic stress conditions, *J. Geophys. Res.*, **84**, 6109-6114.

Wakabayashi, D., Funamori, N., (2013), Equation of state of silicate melts with densified intermediate-range order at the pressure condition of the Earth's deep mantle, *Phys. Chem. Minerals*, **40**, 299-307.

Xue, X., Kanzaki, M., Tronnes, R. G., Stebbins, J. F., (1989). Silicon Coordination and Speciation Changes in Silicate Liquid at High Pressures. *Science*, **245**, pp. 962-964.

Xue, X., Stebbins, J. F., Kanzaki, M., Poe, B. T., McMillan, P. F., (1991). Pressure-induced silicon coordination and tetrahedral structural changes in alkali oxide-silica melts up to 12 GPa; NMR, Raman, and infrared spectroscopy. *Am. Mineral*, **76**, pp. 8-26.

Zhu W., Hirth G., (2003), A network model for permeability in partially molten rocks, (2003), *E. P. S. L.*, **212**, 407-416.